

**University of Alberta**

**Modelling of Light Propagation and Interaction with  
Biological Cells**

by

**YunFeng Shao**



A thesis submitted to the Faculty of Graduate Studies and Research in partial  
fulfillment of the requirements for the degree of Doctor of Philosophy

**Department of Physics**

Edmonton, Alberta

Fall 2002



National Library  
of Canada

Acquisitions and  
Bibliographic Services

395 Wellington Street  
Ottawa ON K1A 0N4  
Canada

Bibliothèque nationale  
du Canada

Acquisitions et  
services bibliographiques

395, rue Wellington  
Ottawa ON K1A 0N4  
Canada

*Your file Votre référence*

*Our file Notre référence*

The author has granted a non-exclusive licence allowing the National Library of Canada to reproduce, loan, distribute or sell copies of this thesis in microform, paper or electronic formats.

The author retains ownership of the copyright in this thesis. Neither the thesis nor substantial extracts from it may be printed or otherwise reproduced without the author's permission.

L'auteur a accordé une licence non exclusive permettant à la Bibliothèque nationale du Canada de reproduire, prêter, distribuer ou vendre des copies de cette thèse sous la forme de microfiche/film, de reproduction sur papier ou sur format électronique.

L'auteur conserve la propriété du droit d'auteur qui protège cette thèse. Ni la thèse ni des extraits substantiels de celle-ci ne doivent être imprimés ou autrement reproduits sans son autorisation.

0-612-81263-4

Canada

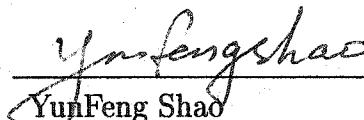
University of Alberta

Library Release Form

NAME OF AUTHOR: YunFeng Shao  
TITLE OF THESIS: Modelling of Light Propagation and  
Interaction with Biological Cells  
DEGREE: Doctor of Philosophy  
YEAR THIS DEGREE GRANTED: 2002

Permission is hereby granted to the University of Alberta Library to reproduce single copies of this thesis and to lend or sell such copies for private, scholarly or scientific research purposes only.

The author reserves all other publication and other rights in association with the copyright in the thesis, and except as herein before provided neither the thesis nor any substantial portion thereof may be printed or otherwise reproduced in any material form whatever without the author's prior written permission.

  
\_\_\_\_\_  
YunFeng Shao  
12 Beaverbrook Lane  
Ottawa, Ontario  
CANADA  
K2K 1L3

*September 18, 2002*

**Imagination is more important than Knowledge**

**Albert Einstein**

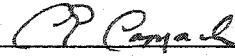
University of Alberta

Faculty of Graduate Studies and Research

The undersigned certify that they have read, and recommend to the Faculty of Graduate Studies and Research for acceptance, a thesis entitled **Modelling of Light Propagation and Interaction with Biological Cells** submitted by **YunFeng Shao** in partial fulfillment of the requirements for the degree of Doctor of Philosophy.



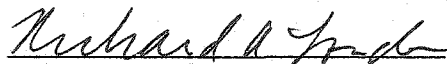
Dr. W. Rozmus (Supervisor)



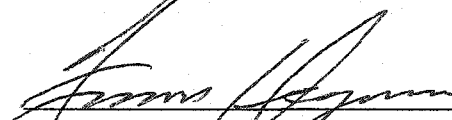
Dr. C. Capjack (Co-supervisor)



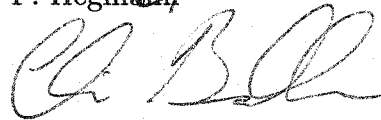
Dr. R. Sydora (Chair)



Dr. R. London (External)



Dr. F. Hegmann



Dr. C. Backhouse

DATE: September 12, 2002

*To*

*Shuping Zhao and Yizhen Shao*

## Abstract

The application of a new technique, based on the spectral method, for describing light scattering by biological cells is reported. The accuracy of the spectral numerical method has been verified by comparison with linear perturbation theory and Mie theory. Comparison with Mie theory has validated that the three-dimensional scalar wave equation is a good approximation to the full Maxwell's set of equations for light scattering at moderate angles. The computational requirements for the spectral method in modelling laser interaction with biological samples are much lower than the requirements for other existing numerical methods such as: finite-difference time-domain and Monte Carlo. Yet the new algorithm is capable of resolving the variations in the scattered signal with a contrast in intensity of up to six orders of magnitude. The spectral technique can be successfully applied to address scattering from individual cells and from biological samples containing many cells. The new method is well suited to recognizing the size and composition of biological cells, making it a valuable tool in cell cytometry, for example, in the detection of rare event cells, cancerous cells and bacterial cells.

A three dimensional coupled vector wave equation comprised of two

orthogonal field components is derived from Maxwell's equation for capturing the polarization information for small angle scattering. The spectral technique has been applied to solve this 3D coupled vector wave equation. Both a 3D-2 component vector field solver and a 3D-3 component vector field solver have been developed. These solvers are capable of providing a more accurate prediction of the angular spectrum of the scattered intensity than that which is provided by our 3D scalar equation solver, especially in the backscattering range. In addition, polarization information is also provided.

An outline of our proposed measurement of laser light scattering from latex beads is presented. A detailed derivation of the normalization constant for both Gaussian beam and plane wave incident sources is provided. Hence, the angular spectra of the scattered light intensity can be reported in an appropriate unit, i.e. *photons/(s.sr)*, allowing for the calculation of the scattering cross section .



## Acknowledgments

The author would like to thank his supervisors, Dr. W. Rozmus and Dr. C. E. Capjack, for their constant guidance and support. The author would also like to thank Dr. A. V. Maximov and I. G. Ourdev for many useful discussions and advice throughout the course of his research. Further thanks go to his colleague D. Shaw for proof reading this manuscript and polishing the English.

## Preface

The results in this thesis were obtained over the course of the author's Ph.D. program at the University of Alberta between 1996 and 2002. The work was done under the supervision of W. Rozmus and C. Capjack. The presentation of this work given here is in accordance with the "Paper Format" regulations of the Faculty of Graduate Studies and Research of the University of Alberta, and is based on the following published papers:

- Y. Shao, A. V. Maximov, I. G. Ourdev, W. Rozmuz, and C. E. Capjack, "*Spectral Method Simulations of Light Scattering by Biological Cells*", published in the *IEEE Journal of Quantum Electronics*. VOL. 37, NO. 5, pp. 617-625, 2001.
- A. V. Maximov, C. E. Capjack, W. Ruzmus, and Y. Shao "*Three-dimensional Modeling of Light Scattering in Biological Tissue by the Spectral Method*", to be presented in the conference *Functional Imaging and Optical Manipulation of Living Cells and Tissues*, 2001. *Proceedings of SPIE Optical Diagnostics of Living Cellular*. VOL. 4260 , pp. 59-67, 2001.
- C.-G. Stefanita, Y. Shao, W. Rozmus, C. E. Capjack, and C. J. Backhouse, "*Microchip-Based Optical Device for Medical Diagnostics Performed on a Single Cell*", *IEEE Proceedings of the 2002 2<sup>nd</sup> Conference on Nanotechnology, Washington D.C., August 26-28*, pp. 133-136.

# Table of Contents

**Abstract**

**Preface**

**Acknowledgements**

**Table of Contents**

**List of Tables**

**List of Figures**

<b>1</b>	<b>Introduction</b>	<b>1</b>
1.1	Analytical Approach . . . . .	6
1.2	Numerical Approach . . . . .	8
<b>2</b>	<b>Review of Mie Theory</b>	<b>19</b>
2.1	Introduction . . . . .	19
2.2	Solutions to the vector wave equations . . . . .	23
2.3	Expansion of a Plane Wave in Vector Spherical Harmonics . . . . .	28
2.4	The Internal and Scattered Fields . . . . .	30
2.5	Scattering Matrix—Mueller Matrix . . . . .	33
2.6	Computations of Mie Theory . . . . .	39

## TABLE OF CONTENTS

<b>3</b>	<b>The Computational Model</b>	<b>45</b>
3.1	Basic Equations . . . . .	45
3.2	The Spectral Method . . . . .	49
3.3	Iteration in Time . . . . .	51
3.4	Boundary Conditions . . . . .	52
3.5	The Shape of Incident Beam . . . . .	53
3.6	Far-field Calculation . . . . .	54
3.7	Conclusions . . . . .	56
<b>4</b>	<b>Code Development and Validation</b>	<b>58</b>
4.1	Introduction . . . . .	58
4.2	Code Development . . . . .	59
4.3	Code Validation . . . . .	60
4.3.1	Linear Perturbation Theory . . . . .	60
4.3.2	Scattering from a Homogeneous Sphere . . . . .	63
4.3.3	Backward Scattering . . . . .	66
4.4	Conclusions . . . . .	71
<b>5</b>	<b>Two Dimensional Simulation Results</b>	<b>86</b>
5.1	Introduction . . . . .	86
5.2	Scattering by Single Cells . . . . .	87
5.3	Scattering by many objects . . . . .	89
5.4	Conclusions . . . . .	93
<b>6</b>	<b>Three Dimensional Simulation Results</b>	<b>97</b>
6.1	Introduction . . . . .	97
6.2	Scattering by a Single Cell . . . . .	98
6.3	Backward Scattering . . . . .	102
6.4	Multiple Scattering . . . . .	102

## TABLE OF CONTENTS

6.5	Conclusions . . . . .	106
<b>7</b>	<b>Polarization Effects</b>	<b>111</b>
7.1	Introduction . . . . .	111
7.2	Polarization Properties of Light . . . . .	112
7.2.1	Linearly Polarized Light . . . . .	112
7.2.2	Circularly Polarized Light . . . . .	113
7.3	The Two Component Vector Wave Equations and Algorithm . . .	114
7.4	Simulation Results . . . . .	116
7.5	The Three Components Vector Wave Equation . . . . .	117
7.6	Conclusion . . . . .	124
<b>8</b>	<b>Experimental Considerations</b>	<b>128</b>
8.1	Introduction . . . . .	128
8.2	A Gaussian Beam Incident Light Source . . . . .	130
8.3	Plane Wave . . . . .	136
8.4	Simulation Results . . . . .	139
8.5	Conclusions . . . . .	145
<b>9</b>	<b>Summary</b>	<b>149</b>

# List of Tables

5.1	The values for index of refraction of various cell components which are used in the simulations. . . . .	87
8.1	Our calculation results of scattering cross section against the published results. . . . .	140
8.2	The cross section of the beads obtained from our calculation using parameters appropriate for the proposed experiments. . . . .	142

# List of Figures

2.1	Geometry of Mie Theory . . . . .	23
2.2	Incident beam scattered by a cell. . . . .	34
2.3	The computational results of Mie theory with parameters of $a/\lambda =$ 1 and $N_1/N = 1.59/1.33$ . . . . .	42
2.4	The computational results of Mie theory with the parameters of $a/\lambda = 5.5$ and $N_1/N = 1.37/1.35$ . . . . .	43
3.1	The profile of time function $f(t)$ . . . . .	48
3.2	The geometry of the simulation . . . . .	50
4.1	The scattering intensity from simulations and analytical formula for three types of square cells . . . . .	62
4.2	Scattering intensity by a homogeneous sphere-I . . . . .	64
4.3	Scattering intensity by a homogeneous sphere-II . . . . .	65
4.4	Backward scattering signals on the left boundary from a two di- mensional cell with diameter of $11\mu m$ and dielectric constant of 1.8769 . . . . .	73
4.5	The profiles of smooth cutoff . . . . .	74
4.6	Scattering intensities in far-field . . . . .	75
4.7	The backscattered phase function of Mie theory over a small range of size parameters. . . . .	76

## LIST OF FIGURES

4.8	Smooth profile of the interface between cytoplasm and surrounding medium and its scattering intensity distribution . . . . .	77
4.9	Sharp profile of the interface between cytoplasm and surrounding medium and its scattering intensity distribution . . . . .	78
4.10	“Smooth” profile of the interface between cytoplasm and surrounding medium and its scattered intensity distribution . . . . .	79
4.11	The much sharper profile of the interface between cytoplasm and surrounding medium and its scattering intensity distribution. . . . .	80
4.12	Two different profiles of the interface between cytoplasm and surrounding medium in the high resolution case of 12 points per wavelength. . . . .	81
4.13	Simulation results of the scattered intensity distributions for four different interface profiles. . . . .	82
4.14	Simulation results of the scattered intensity distributions for different cell sizes with the very sharp interface profile. . . . .	83
5.1	Scattering intensity from a two dimensional single cell . . . . .	88
5.2	An example of the random distribution of scatterers in the simulation region. . . . .	91
5.3	Scattering intensity as a function of scattering angle for ten scatterers and for a single scatterer. . . . .	92
5.4	The dependence of scattered power (a) and the average scattering angle (b) on the number of scattering objects. . . . .	94
6.1	Scattered light intensity from plane wave for three types of cells . . . . .	98
6.2	Scattered light intensity from plane wave for three sizes of cells . . . . .	99
6.3	Scattered intensity from a Gaussian beam with $f/3$ optics on a logarithmic scale (a) and linear scale (b) for three types of cells . . . . .	101



*LIST OF FIGURES*

6.4 Scattered intensity from a Gaussian beam with  $f/10$  on a logarithmic scale (a) and linear scale (b) for three types of cells . . . . . 103

6.5 Forward scattering intensity (a) and backscattering intensity (b) from a three dimensional single cell with different size . . . . . 104

6.6 The scattering angular distribution from single cell. . . . . 106

6.7 The difference of scattering angular distribution from 10 cells and from single cell. . . . . 107

6.8 Multiple scattering distribution of laser light from 18 cells and 34 cells. . . . . 108

6.9 Dependence of the scattered intensity on the number of scatterers (cells). . . . . 109

7.1 The angular spectra of forward and backward scattered lights for two orthogonal vector components . . . . . 118

7.2 Scattering by a cell—two components vector wave equation solver. 119

7.3 Comparison of our simulation results  $i_{\parallel}/i_{\perp}$  with Mie theory results.120

7.4 The angular spectra of forward and backward scattered light for the  $E_y$  and  $E_z$  components of the electric field as predicted by our three component vector wave equation solver. . . . . 125

7.5 The backward scattered intensity by a cell with diameter  $D_0 = 11\mu m$  as simulated by our 3D-3 component vector solver (solid line), 3D-2 component vector solver (dotted line), and 3D scalar solver (dash-dotted line). The dashed line is the result of Mie theory.126

8.1 Microchip for manipulation of cells . . . . . 130

8.2 Schematic of the experimental setup for measuring forward scattered light by cells . . . . . 131

8.3 A Gaussian Beam with  $f/12$  at best focus, represented as a contour plot. . . . . 132

## LIST OF FIGURES

8.4	The far-field distributions of a Gaussian beam with (a) $f/15$ and (b) $f/12$ . . . . .	135
8.5	The far-field distribution for an incident plane wave in the absence of scattering. . . . .	138
8.6	The far-field distributions (a) for a Gaussian Beam with $f/12$ and (b) for a plane wave. . . . .	141
8.7	The far-field distributions (a) for a Gaussian Beam with $f/12$ and (b) for a plane wave. . . . .	143
8.8	The far-field distributions (a) for a Gaussian Beam with $f/12$ and (b) for a plane wave. . . . .	144
8.9	Photons/s incident on $1\mu m^2$ of CCD vs scattering angle. . . . .	146

# Chapter 1

## Introduction

Lasers have several unique properties, such as monochromaticity, high power, short pulse duration, and coherence, which are particularly useful for biological and medical applications. Laser medicine is now a quickly growing research field. The increasing use of laser light for both diagnostic and therapeutic medicine has created a need to understand how laser light propagates through biological tissues, in order to enable the quantitative analysis of diagnostic measurements and the optimum development of therapeutic techniques.

There are five main categories [1–3] of photophysical processes in laser light tissue interactions. There are non-destructive photo interactions, photochemical, photothermal, photoablative and photomechanical interactions. Non-destructive photo interactions mainly concern laser light propagation and scattering in tissue, which can be used both for imaging and diagnostics. Photochemical interactions involve the absorption of light by specific molecules that are either present in, or added to, a tissue sample. Such interactions are the basis for photodynamic therapy. Photothermal interactions are those where the observed biological effect is due to the deposition of heat in the tissue. Most current laser surgery, such as welding and coagulation, for example, falls into this category. Photoablative in-

teractions can occur when photons have sufficient energy to cause the dissociation of biopolymers and subsequent desorption of fragments. The threshold for this effect to occur with  $10\text{ns}$  pulses is approximately  $10^8\text{Wcm}^{-2}$ . Photomechanical interactions occur at fluence rates of approximately  $10^{10}\text{Wcm}^{-2}$  for nanosecond pulses and  $10^{12}\text{Wcm}^{-2}$  for picosecond pulses. When these ps pulses illuminate tissue, the dielectric of the tissue experiences breakdown, and a small volume plasma is produced. The expansion of this plasma creates a shock wave which can mechanically rupture the tissue. These last two types of interaction are complex in terms of their thresholds and nonlinear effects. Both can be used for tissue ablation, emulsification and drug delivery.

At the Lawrence Livermore National Laboratory (LLNL), a computer code named LATIS [6] has been developed to realistically model these physical processes (excluding the first category of non-destructive photo interactions) for medical applications. LATIS is a two-dimensional, time-dependent simulation program which takes into account laser light transport, mechanical response, thermal response, and material response, and the non-linear interactions between these phenomena. It has been demonstrated that LATIS can be used in describing such applications such as the ablation of hard biological tissue [7], vapor bubble generation by short-pulse lasers [8], and tissue welding.

I will not discuss the last four types of photophysical processes further in this thesis; instead, I will focus on non-destructive photo interactions, where the optical properties of the tissue do not change in time and are independent of the light intensity. Optical properties of tissue and individual cells are very important for a wide range of studies from imaging and diagnostic applications, such as cytometry [9], confocal [10] and optical coherence tomography [11] imaging, and fundamental investigations of a cells' sensitivities to light sources [12]. When laser light enters a biological sample, it can be scattered and absorbed. The

relative probability of these processes in a given tissue depends on the laser wavelength [4]. In these applications, laser light from the blue to near-infrared parts of the spectrum is predominantly scattered from local variations of the index of refraction between different parts of cells and other small structures in the sample.

Cytometry is the measurement of physical and/or chemical characteristics of cells, or, by extension, of other biological particles. Flow cytometry [13] is a process in which such measurements are made while the cells or particles pass, preferably in single file, through the measuring apparatus in a fluid stream. During the past 30 years, sophisticated improvements have made flow cytometry a powerful and invaluable tool for the quantitative analysis of individual cells or other biological particles. A flow cytometer is an instrument, which can be used to obtain quantitative information based on light scattering or fluorescence emission caused by individual cells (or particles) as they flow rapidly in a fluid stream in front of a light source [14]. The components of a flow cytometer usually include a light source (normally a laser); a sample chamber with flow cell and sheath fluid stream; a photodetector or photomultiplier tubes (PMTs) that collect light and convert it to a electronic signals; a signal processing system that converts the signal from analog to digital; and a computer to direct operations, store the collected signals, and display data [15]. With the combination of state-of-the-art advances in computer and laser technology, more sophisticated flow cytometers have been developed to obtain objective and precise measurements of multiple characteristic parameters of an individual cell at one time. Such parameters include cell size, cell shape, and cytoplasmic granularity (refractive index).

In conventional flow cytometry, the physical properties of cells are deduced from an analysis of the angular distribution of scattered light. When a cell (or

particle) passes in front of the disc-like focused narrow laser beam, the light is scattered in all directions. The larger the cells, the more light is scattered. Through comparison of relatively simple forward and backward scattering information, broad categorizations of cells can be performed. The identification of different types of cells is based on the empirical observation [16] that the small-angle scatter in the forward direction is more sensitive to the size of the cell, while the large-angle scattering primarily depends on small-scale structures inside the cell or other granularity. The processing of this relatively simple information is dictated by several factors. For example, the system is able to position the cells only by moving them at high speed, thereby limiting the time available for data acquisition. In addition, the detectors are limited to detecting the light scattered far from the original beam direction, since any scattering signal near the collimated beam is negligible compared with the beam itself. Moreover, insufficient information is obtained to account for cell rotation effects. As a result, only simple predictions can be made.

Recently, microfluidic devices or microchips, which consist of micromachined channels (typically  $100\mu m$  wide), have been used in improving flow cytometry techniques. In Ref. [17], Schrum et al. demonstrated a microchip-based cytometer with which they sorted latex beads, correlating the scattered peak intensity with the bead size. They used two different sizes of particles: fluorescent smaller particles with a diameter of  $0.972\mu m$  and non-fluorescent large particles with a diameter of  $1.94\mu m$ . The results show that peak intensity, which corresponds to the total scattered intensity by a particle, was 0.235 times smaller for the  $0.972\mu m$  fluorescent particles than for the  $1.94\mu m$  non-fluorescent particles. These observations are consistent with Mie theory, which predicts that the scattered intensity should be proportional to the particle surface area and, therefore, to the square of the particle diameter [24]. This was a powerful demonstration of

the manipulation of latex beads, especially with regards to the use of hydrodynamic focusing—balancing fluid flows to position the beads in the laser beam so as to ensure a reproducible scattering signal. However, because of the very fast movement of the beads (34 beads per second), their apparatus was incapable of detecting more than the peak value of the scattered signal, which greatly limited the information that could be extracted from the experimental data. A U.S. company called Micronics has developed a microcytometer in which biological cells from a sample, such as blood, pass in single file through a micro-channel upon which a laser beam is focused. Light scatter measurements are taken at multiple angles over two ranges: forward angle scattering (from 0 to 3 degrees) and small angle scattering (from 3 to 11 degrees), and these multi-parameter scatter measurements provide information not simply about the size but also about the internal cellular structure for the various type of cells. A study of this device's ability to separate several types of white blood cells has been presented in Ref. [18]. This would be very useful in blood counting and differentiation.

Understanding relationships between measured scattered light properties and physiological differences at the cellular level is fundamental to the usefulness of optical diagnostics and constitutes the main challenge for the modelling of light scattering from cells. Both analytical approximations and numerical solutions have been used to model tissue scattering. Due to the complexity of scattering media, and the fact that dielectric constant inhomogeneities occur on scales comparable to the laser wavelength, analytical solutions to the scattering problem are limited. Several numerical procedures originally employed in other physical and engineering applications have been adopted to the cell scattering problem.

## 1.1 Analytical Approach

Mie theory, which was published in 1908 by G. Mie [19, 20], refers to the electromagnetic theory for the diffraction of a plane monochromatic wave by a homogeneous sphere of arbitrary diameter and refractive index immersed in a homogeneous medium. In fact, Mie theory is a rigorous solution to the Maxwell equations describing the field generated by a plane monochromatic wave incident upon a spherical surface, at which the refractive index of the medium changes abruptly. Based on Mie theory, the electromagnetic fields inside and outside the sphere can be expressed by infinite series expansions. To obtain quantitative results from the Mie theory it might seem that we are faced a straightforward task. However, the number of terms in the series required for convergence can be very large. For example, we need to sum about 12,000 terms in investigating the rainbow — a visible scattering phenomenon, if we assume a water droplet radius of  $1\text{mm}$ . Such a calculation clearly requires much more than just patience and pocket calculator. Even for smaller particles the number of calculations can be painfully large. Indeed, although the Mie theory has been available for many years, only the recent development of fast computers has made it a practical means for detailed computations.

Mie theory has many applications in the study of light scattering by biological objects. For example, it can be used to calculate light scattering from tissue on the cellular level by assuming that cells are homogeneous spheres [21]. It has also been used to describe light scattering from coated spheres, which represent many types of biological cells with a nucleus of a refractive index  $\approx 1.1$  and a cytoplasm with a slight lower refractive index [22], as well as to study the dependence of the backward scatter pattern on membrane thickness and refractive index when light is scattered from biological cells [23].

In summary, Mie theory has been very successful in describing light scattering



from biological cells which can be approximated by homogeneous spheres of any diameter with arbitrary values for the refractive index and for simple 2-layered structures. Indeed, the scattering matrix (Mueller Matrix) for a homogeneous sphere can be constructed from Mie theory. However, Mie theory is unable to describe the interaction of light and biological cells with arbitrary shapes or with complex structures such as multiple organelles contained within individual cells.

Mie theory provides a benchmark for testing other analytical solutions [25] and numerical approaches [38] which are developed to account for light scattering that arises from inhomogeneous biological objects of arbitrary shape. In this thesis, Mie theory will be used as the benchmark for validating numerical results. A detailed description of Mie theory will be presented in Chapter 2 and the numerical results of a modified version of Bohren and Huffman's computer code [24] are also presented in Chapter 2.

When the shape of the cell is not spherical, but is still homogeneous inside, several approximate analytical methods, such as Wentzel-Kramer-Brillouin (WKB) [25, 26], Rayleigh-Gans-Debye (RGD) [27], Fraunhofer diffraction, and anomalous diffraction [28], have been used to model the resulting scattering of light. All these approximate analytical methods have been compared numerically with the exact Mie theory solution for the specific case of spherical cell scattering. With regard to erythrocytes (red blood cells), which are biconcave and disk-shaped, the WKB method used in Ref. [25] gives qualitative agreement with experimental results of scattered light over an angular range of  $15^\circ - 35^\circ$ . However, these analytical methods involve increasing computational complexity and become impractical for complicated shapes of particles and cells with more complex internal structure.

## 1.2 Numerical Approach

One of the common numerical techniques that has been used to date to describe laser light scattering from tissues and cells is the Monte Carlo technique. This method was first proposed by Metropolis and Ulam to simulate physical processes using a stochastic model [29], has been used to solve a variety of physical problems. In all applications of the Monte Carlo method, a stochastic model is constructed in which the expected value of a certain random variable (or of a combination of several variables) is equivalent to the value of a physical quantity to be determined. This expected value is then estimated by the average of multiple independent samples representing the random variable introduced above.

Monte Carlo simulations of photon propagation provide a flexible yet rigorous approach toward photon transport in turbid tissues [30,31]. This method describes local rules of photon propagation that are expressed as probability distributions for the step size of photon movement between sites of photon-tissue interaction, for the angles of deflection in a photon's trajectory when a scattering events occurs, and for the probability of transmittance or reflectance at boundaries. This method simulates the "random walk" of photons in a medium that contains absorption and scattering centers. The simulation can model multiple physical quantities simultaneously and produces a rigorous description of light propagation in biological tissue. However, this method is wholly statistical in nature and relies on numerical calculations for the propagation of a large number of photons. As a result, this method requires a large amount of computational time.

The number of photons required depends largely on the question being considered, the precision needed, and the spatial resolution desired. For example in Ref. [30], in order to simply have the total diffuse reflectance from tissue of spec-

ified optical properties, typically about 3,000 photons can yield a useful result. To have the spatial distribution of photons in a cylindrically symmetric problem, at least 10,000 photons are required. To map spatial distributions in a more complex three-dimensional problem, such as a finite diameter beam irradiating a tissue sample, the required number of photons may exceed 100,000.

Two important aspects of the Monte Carlo simulations deserve emphasis. First, MC simulations are based on macroscopic optical properties of tissue and do not treat details of the radiant energy distribution within cells. As a result, one cannot extract information concerning the refractive index on the cellular level from the MC simulations. Secondly, MC simulations usually treat the photon as a neutral particle and not as a wave phenomenon. Hence, features such as phase and polarization are ignored. Recently, Mainland et al.[32] conducted Monte Carlo simulations of polarized light propagation in microsphere suspensions. In this application, a normalized Stoke matrix was used for the photon polarization information and the Mueller Matrix, which is calculated from Mie theory, was used in the MC model for the scatterers, so that photons would still have the polarization information intact after a scattering event occurs.

The finite-difference time-domain (FDTD) method, or Yee's algorithm, which is an algorithm first described by Yee [33] to solve initial-boundary value problems for Maxwell's equation in isotropic media, has been used in a wide range of electromagnetic modelling applications including electromagnetic absorption of tissue in hyperthermia [34], scattering cross-section calculations of arbitrary objects [35], and scattering from frequency-dependent materials [36].

The FDTD algorithm solves for both the electric  $\vec{E}$  and magnetic  $\vec{H}$  fields in time and space by using the coupled Maxwell's equations. The FDTD algorithm centers its  $\vec{E}$  and  $\vec{H}$  components in three-dimensional space so that every  $\vec{E}$  component is surrounded by four circulating  $\vec{H}$  components. The FDTD al-

gorithm also centers its  $\vec{E}$  and  $\vec{H}$  components in time. All  $\vec{E}$  components have the full-point value and all  $\vec{H}$  components have the half-point value in the three-dimensional space and in time. All computations of  $\vec{E}$  over the spatial region of interest are completed and stored in the memory for a particular time point by using the  $\vec{H}$  data from the previous iteration. Then all of the  $\vec{H}$  computations in the modeled space are computed and stored in memory using the  $\vec{E}$  data just computed. The cycle is repeated until time-stepping is ended. The increment of iteration both in three-dimensional space and time is  $1/2$  of space/time step. A detailed explanation of the FDTD method can be found in Ref. [37].

Recently, the FDTD algorithm has been implemented to model the cellular scattering problem [38–40]. In this application, the size of the computational domain is slightly larger than the cell size, and the dielectric constant  $\epsilon(i, j, k)$  for the simulation medium is specified at each grid point  $(i, j, k)$  in three-dimensional space. The cell is constructed as a dielectric object by assigning different dielectric constant values to each of the different components, such as the nucleus, the cytoplasm, and the mitochondria [38–40]. Due to computational stability considerations, the grid spacing  $\Delta$  must be less than  $\lambda/10$  and the maximum time step is limited to  $\Delta/(c\sqrt{2})$ , where  $c$  is the speed of light in the medium and  $\lambda$  is the laser light wavelength. Thus, the FDTD method requires extensive computational resources, especially for three-dimensional problems. As reported in Ref. [38], the grid spacing in the simulation was  $\lambda/20$  ( $\lambda = 900nm$ ), a sinusoidal source was stepped in time until sinusoidal steady state of the scattered fields was reached. This typically requires 3 or 4 passes through the grid. The scattering pattern,  $F(\theta, \phi)$ , was computed in one-degree resolution for both  $\theta$  and  $\phi$ . A simulation for an object  $12\mu m$  in diameter typically required 100 Mwords of storage and 30 minutes of system CPU time on a Cray J90 computer.

The coupled dipole method was introduced to describe scattering from dielec-

tric particles of an arbitrary shape in astrophysical applications [41]. It has since been adapted to the cell scattering problem [42]. In the coupled dipole algorithm, scattering particles are placed on a cubic grid and subdivided into smaller sub-regions, each modeled as a dipole. The external field and the field due to the dipoles themselves both contribute to the far field values of the scattered intensity.

Overall, the use of MC simulations and FDTD algorithms are the two established mainstream approaches for modelling laser light propagation in biological tissue for multiple scattering studies. The MC method efficiently describes multiple scattering from tissues; however, it is not well suited to resolving the scattering from single cells, especially from cells of different sizes and compositions, and may lose the polarization and phase information. On the other hand, the FDTD method accurately describes scattering from a single cell, but requires large amounts of computer memory and time as the FDTD algorithm solves the full vector electric and magnetic fields and resolves their time evolution on the scale of a laser light period. Such a complete solution is unnecessary when scattering occurs on stationary cells and modelling is restricted to the angular distribution of the scattered light intensity. Moreover, its application to multiple cell scattering further increases computational resource requirements.

The goals of this thesis are: (1) to develop a new technique, based on the existing spectral method [44], which can be applied in studies of single cell scattering and multiple scattering in large samples; (2) to develop a computer simulation code which is capable to modelling and predicting the laser light propagation in biological tissues; (3) to provide numerical support for planed micro-cytometry experiments in the Electrical & Computer Engineering Department at the University of Alberta; and (4) for other possible optical diagnostic applications in laser medicine.

The proposed new numerical method for modelling laser light scattering from cells is based on a simplified mathematical model of light propagation and the spectral algorithm. The spectral method has been successfully used to study the physics of laser-plasma interactions [43]. In these applications, the plasma, which is a neutral gas of charged particles, was modelled as a time-dependent, spatially inhomogeneous dielectric. Similarly, biological cells or tissues are modelled as spatially varying dielectrics, although stationary in time. The results of numerical and analytical studies in both two and three spatial dimensions (cf. [38], [39]) are presented in this thesis. In the two dimensional studies, the relative changes in the scattering intensity distribution due to the internal cell structure, shape, size, and refractive index can be addressed more easily than in three dimensions. Multiple scattering processes, i.e., the dependence of the scattered light characteristics on the number of scatterers and the packing parameter, i.e, density of cells, have been illustrated in 2-D simulations.

In our approach, the full set of Maxwell equations is reduced to the wave equation for the electric field. Further approximations include the elimination of high frequency ( $\omega_0$ ) oscillations by enveloping field amplitude variations that occur on time scale of  $1/\omega_0$  and reducing the order of a time derivative in the wave equation. As compared, for example, to the FDTD method we have reduced the number of equations, eliminated the need for high time resolution, and achieved convergence with just six points per laser wavelength. By reducing numerical requirements, we have produced an effective algorithm, which can be applied to studies of a single cell as well as in tissue scattering problems where our code can be used to model large samples. The application of the FDTD method to the latter case is impractical because of the large computational requirements. The Monte Carlo (MC) techniques allows calculations of light propagation in large geometries, but the loss of information regarding the coherence of scattered

radiation makes this approach unsuitable for modelling of confocal or optical coherence tomography imaging [10, 11].

The remainder of this thesis is organized as follows. This introductory chapter is followed by a chapter describing Mie theory. Chapter three contains a description of the numerical model in which the scalar wave equations, the spectral method, and the calculation of the scattered light amplitude in the far-field are addressed. Chapter four details code development and testing. Chapters five and six present the 2-D and 3-D simulation results, respectively. Chapter seven addresses polarization effects in laser-tissue scattering. The spectra method has also been applied to solve a coupled three dimensional vector wave equation with two orthogonal field components and a wave equation with 3 electric field components in a 3-D geometry. In chapter eight, we present an outline of our proposed experimental measurement of laser light scattered by a latex bead. We also present a detailed derivation of the normalization constant for both Gaussian beam and plane wave incident sources. The scattered light intensity distribution can therefore be presented in an appropriate unit, i.e *photons/(s.sr)*, and the simulation results of our 3D scalar solver can predict the outcome of the proposed measurement. The last chapter contains concluding remarks and proposes further development of this research topic.

## Bibliography

- [1] R. A. London, *Laser Tissue Interaction Modeling*, Seminar in University of Alberta (1998)
- [2] M. S. Patterson, B. C. Wilson, and D. R. Wyman, *The propagation of optical radiation in tissue I*, *Lasers in Medical Science* **6** 155-168 (1991)
- [3] J. L. Boulnois, *Photophysical processes in recent medical laser developments: a review*, *Lasers in Medical Science* **1** 47-66 (1986)
- [4] M. S. Patterson, B. C. Wilson, and D. R. Wyman, *The propagation of optical radiation in tissue II*, *Lasers in Medical Science* **6** 379-390 (1991)
- [5] G. B. Zimmerman and W. L. Kruer, *Numerical Simulation of Laser-initiated fusion*, *Commun. Plasma Phys. Controlled Fusion*, **11**, 51-61 (1975).
- [6] R. A. London, M. E. Glinsky, G. B. Zimmerman, D. S. Bailey, D. C. Eder, and S. L. Jacques, *Laser-tissue interaction modeling with LATIS*, *J. Appl. Optics*, **36**, 9068-9074 (1997)
- [7] D. S. Bailey, R. A. London, and W. E. Alley *Hard tissue ablation simulations using the LATIS computer code*, *SPIE* **3254** 232-240 (1998)
- [8] P. Amendt, R. A. London, M. Glinsky, D. J. Maitland, P. M. Celliers, S. R. Visuri, D. S. Bailey, D. A. Young, D. Ho, C. P. Lin, and M. W. Kelly



- Simulations studies of vapor bubble generation by short-pulse lasers*, SPIE **3195** 259-272 (1998)
- [9] A. Gilman-Sachs, *Anal. Chem.* **66**, 700 (1994).
- [10] M. Grossman, D. Esterwitz, R. Webb, and R. Anderson, *J. Invest. Dermatol.* **104**, 946 (1995).
- [11] J. Izatt, M. Hee, D. Huang, A. Swanson, C. Lin, J. Schuman, C. Puliafito, and J. Fujimoto, *Opt. Photonics News* **4**, 14 (1993).
- [12] G. Albrecht-Buehler, *Surface extensions of 3T3 cells towards distant infrared sources*, *J. Cell. Biol.* **114** 493-502(1991)
- [13] H. M. Shapiro, *Practical Flow Cytometry*, (Alan R. Liss, New York 1988)
- [14] A. Gilman-Sachs, *Flow cytometry*, *Anal. Chem.*, **66** 700A-707A, (1994)
- [15] E. J. Lovett, B. Schnitzer, D. F. Keren, A. Flint, J. L. Hudson, K. D. McClatchey, *Lab. Invest.* **50** 115-140 (1984)
- [16] D. H. Tycko, M. H. Metz, E. A. Epstein, A. Grinbaum, *Flow-cytometric light scattering measurement of red blood cell volume and hemoglobin concentration*, *Applied Optics*, **24**, 1355(1985)
- [17] D. P. Schrum, C. T. Culbertson, S. C. Jacobson, and J. M. Ramsey *Microchip flow cytometry using electrokinetic focusing*, *Anal. Chem.* **71**, 4173-4177(1999)
- [18] E. Altendorf, D. Zebert, M. Holl, A. Vannelli, C. Wu and T. Schulte, *Results obtained using a prototype microfluidics-based hematology analyzer*, Micro TAS98, Banff, Canada(1998)
- [19] G. Mie, *Ann. d. Physik* (4), **30** 377(1908)

- [20] M. Born and E. Wolf, *Principles of Optics* (Pergamon, Oxford, 1970).
- [21] E. Saidi, S. Jacques, and F. Kittel, *Mie and Rayleigh modeling of visible-light scattering in neonatal skin*, *Appl. Opt.* **34** 7410-7418 (1995)
- [22] A. Brusting and P. F. Mullaney, *Light scattering from coated spheres: model for biological cells*, *Appl. Opt.* **11** 675-680 (1972)
- [23] R. A. Meyer, *Light scattering from biological cells: dependence of backscatter radiation on membrane thickness and refractive index*, *Appl. Opt.* **18** 585-588 (1979)
- [24] C. F. Bohren and D. R. Huffman, *Absorption and Scattering of Light by Small particles*, (Wiley, New York, 1983)
- [25] A. N. Shvalov, J. T. Soini, A. V. Chernyshev, P. A. Tarasov, E. Soini and V. P. Maltsev, *Light-scattering properties of individual erythrocytes*, *Applied Optics* **38** 230-235 (1999)
- [26] J. D. Klett and R. A. Sutherland, *Approximate methods for modeling the scattering properties of nonspherical particles: evaluation of the Wentzel-Kramers-Brillouin method*, *Applied Optics* **31** 373-386 (1992)
- [27] H. C. van de Hulst, *Light Scattering by Small particles*, (Wiley, New York, 1957)
- [28] G. J. Steekstra, A. G. Hoeksta, E. Nijhof, and R. M. Heethaar, *Light-scattering by red blood cells in ektacytometry: Fraunhofer versus anomalous diffraction*, *Applied Optics* **32** 2266-2272 (1993)
- [29] N. Metropolis, S. Ulam, *Monte Carlo Method*, *Journal of the American Statistical Association* **44**, 335-341(1949)

- [30] A. J. Welch and M. J. C. Van Gemert, *Optical-Thermal Response of Laser-Irradiated Tissue*, Plenum, New York, (1995)
- [31] S. A. Prahl, M. Keijzer, S. L. Jacques, A. J. Welch, *A Monte Carlo model of light propagation in tissue* SPIE 155, 102-111 (1989)
- [32] D. Maitland, V. Sankaran, P. Amendt, R. London and G. Zimmerman, *Monte Carlo simulations of polarization light propagation in microsphere suspensions*, A Seminar on Medical Technology Program at LLNL
- [33] K. Yee, IEEE Trans. Antennas Propagation AP-14, 302 (1966).
- [34] D. M. Sullivan, D. T. Borup, and O. P. Gandhi, *Use of the finite-difference time-domain method in calculating EM absorption in human tissues*, IEEE Trans. Biomed. Eng., 34 148-157 (1987)
- [35] A. Taflove and K. Umashankar, *Radar cross section of general three-dimensional structures*, IEEE Trans. Electromagn. Compat. 25 433-440 (1983)
- [36] R. Luebbers and H. Hunsberger, *FDTD for Nth-order dispersive media*, IEEE Trans. Antennas Propagat. Mag., 37 39-56 (1992)
- [37] A. Taflove, *Computational Electrodynamics: The Finite-Difference Time-Domain Method*, Artech House, Norwood, MA (1995)
- [38] A. Dunn, R. Richards-Kortum, *Three Dimensional Computation of Light Scattering from Cells*, IEEE Journal of Selected Topics in Quantum Electronics 2, 898 (1996).
- [39] A. Dunn, C. Smithpeter, A. J. Welch, and R. Richards-Kortum, *Finite-Difference Time-Domain Simulation of Light Scattering from Single Cells*, Journal of Biomedical Optics 2, 262 (1997).

- [40] A. Dunn *Light Scattering Properties of Cells*, Dunn's Ph.D Thesis(1997).
- [41] E. M. Purcell, and C. R. Pennypacker, *Scattering and Absorption of Light by Nonspherical Dielectric Grains*, *Astrophys. J.* **186**, 705 (1973).
- [42] A. Hoekstra, and P. Slood, *New Computational Technique to Simulate Light Scattering from Arbitrary Particles*, *Particle System Characterization*, **11**, 189 (1994).
- [43] M.R. Amin, C.E. Capjack, P. Frycz, W. Rozmus, and V.T. Tikhonchuk, *Two dimensional simulations of stimulated Brillouin scattering in laser produced plasma*, *Phys. Rev. Lett.* **71**, 81-84 (1993); *Phys. Fluids B* **5**, 3748 (1993)
- [44] C. Canuto, M. Y. Hussaini, A. Quarteroni, T. A. Zang, *Spectral Methods in Fluid Dynamics* (Springer-Verlag, Berlin Heidelberg 1988).

## Chapter 2

# Review of Mie Theory

### 2.1 Introduction

We consider the problem of a particle with given size, shape, and optical properties illuminated by a monochromatic wave. Our goal is to determine the electromagnetic field at all points in the homogeneous medium in which the particle is embedded. Clearly, the amount and angular distribution of the light scattered by a particle depends in a detailed way on the nature of the particle. In general, the light scattered by an arbitrary particle can be expressed by [1]:

$$\vec{S}_s = \mathbf{M}\vec{S}_i \quad (2.1)$$

where  $\mathbf{M}$  stands for a  $4 \times 4$  Mueller matrix and  $\vec{S}_s$  and  $\vec{S}_i$  are the Stokes vectors which have the following form:

$$\vec{S} = \begin{pmatrix} I = \text{Total Intensity} \\ Q = \text{Linear Polarization } (I_{0^\circ} - I_{90^\circ}) \\ U = \text{Linear Polarization } (I_{+45^\circ} - I_{-45^\circ}) \\ V = \text{Circular Polarization } (I_{\text{right}} - I_{\text{left}}) \end{pmatrix}, \quad (2.2)$$

where  $I$ ,  $Q$ ,  $U$ , and  $V$  are the Stokes parameters which are an equivalent description of polarized light, particularly in scattering problems.

An arbitrary monochromatic wave may be expressed as a superposition of two orthogonal components: horizontal  $E_x$  and vertical  $E_y$ ; right-circular and left-circular; and so on. Therefore, the electric field  $\vec{E}$  referred to the orthogonal axes  $\hat{e}_x$  and  $\hat{e}_y$  is

$$\vec{E} = \vec{E}_0 \exp(ikz - i\omega t) \quad (2.3)$$

$$\vec{E}_0 = E_x \hat{e}_x + E_y \hat{e}_y, \quad (2.4)$$

and the Stokes parameters of  $I$  and  $Q$  take the following form:

$$I = I_{0^\circ} + I_{90^\circ} = E_x E_x^* + E_y E_y^* \quad (2.5)$$

$$Q = I_{0^\circ} - I_{90^\circ} = E_x E_x^* - E_y E_y^*. \quad (2.6)$$

By introducing another orthonormal set of basis vector  $\hat{e}_+$  and  $\hat{e}_-$ , which are obtained by rotating  $\hat{e}_x$  by  $+45^\circ$  and  $-45^\circ$ :

$$\begin{aligned} \hat{e}_+ &= \frac{1}{\sqrt{2}}(\hat{e}_x + \hat{e}_y) \\ \hat{e}_- &= \frac{1}{\sqrt{2}}(\hat{e}_x - \hat{e}_y), \end{aligned} \quad (2.7)$$

the electric field  $\vec{E}_0$  may be written as

$$\vec{E}_0 = E_+ \hat{e}_+ + E_- \hat{e}_-, \quad (2.8)$$

where

$$\begin{aligned} \hat{E}_+ &= \frac{1}{\sqrt{2}}(E_x + E_y) \\ \hat{E}_- &= \frac{1}{\sqrt{2}}(E_x - E_y). \end{aligned} \quad (2.9)$$

Therefore, the third Stokes parameter  $U$  takes the following form:

$$U = I_{+45^\circ} - I_{-45^\circ} = E_+ E_+^* - E_- E_-^* = E_x E_y^* - E_y E_x^* \quad (2.10)$$

For consideration of circularly polarized light, one more set of basis vectors  $\hat{e}_R$  and  $\hat{e}_L$  are introduced:

$$\begin{aligned}\hat{e}_R &= \frac{1}{\sqrt{2}}(\hat{e}_x + i\hat{e}_y) \\ \hat{e}_L &= \frac{1}{\sqrt{2}}(\hat{e}_x - i\hat{e}_y).\end{aligned}\quad (2.11)$$

These basis vectors represent right-circularly and left-circularly polarized waves and are orthonormal since

$$\begin{aligned}\hat{e}_R \cdot \hat{e}_R^* &= 1, \\ \hat{e}_L \cdot \hat{e}_L^* &= 1, \\ \hat{e}_R \cdot \hat{e}_L^* &= 0.\end{aligned}$$

The incident field  $\vec{E}_0$  may be written as

$$\vec{E}_0 = E_+ \hat{e}_R + E_- \hat{e}_L, \quad (2.12)$$

where

$$\begin{aligned}\hat{E}_R &= \frac{1}{\sqrt{2}}(E_x - iE_y) \\ \hat{E}_L &= \frac{1}{\sqrt{2}}(E_x + iE_y).\end{aligned}\quad (2.13)$$

Therefore, the last Stokes parameter  $V$  takes the following form:

$$V = I_{right} - I_{left} = E_R E_R^* - E_L E_L^* = i(E_x E_y^* - E_y E_x^*) \quad (2.14)$$

Assuming  $E_x$  and  $E_y$  take the following forms:

$$\begin{aligned}E_x &= A_x e^{-i\phi_x} \\ E_y &= A_y e^{-i\phi_y},\end{aligned}$$

the Stokes parameters  $I$ ,  $Q$ ,  $U$ ,  $V$  are written as:

$$I = E_x E_x^* + E_y E_y^* = E_x E_x^* + E_y E_y^* = A_x^2 + A_y^2, \quad (2.15)$$

$$Q = E_x E_x^* - E_y E_y^* = E_x E_x^* - E_y E_y^* = A_x^2 - A_y^2, \quad (2.16)$$

$$U = E_+ E_+^* - E_- E_-^* = E_x E_y^* + E_y E_x^* = 2A_x A_y \cos \delta, \quad (2.17)$$

$$V = E_R E_R^* - E_L E_L^* = i(E_x E_y^* - E_y E_x^*) = 2A_x A_y \sin \delta, \quad (2.18)$$

where the phase difference  $\delta$  is  $\phi_x - \phi_y$ .

The various degrees of polarization are defined as follows:

$$\text{Degree of linear polarization} = \sqrt{Q^2 + U^2}/I$$

$$\text{Degree of circular polarization} = \sqrt{V^2}/I$$

$$\text{Degree of total polarization} = \sqrt{Q^2 + U^2 + V^2}/I. \quad (2.19)$$

In particular, if  $E_x$  and  $E_y$  have the same amplitude  $A_x = A_y$  and same phase  $\phi_x = \phi_y$ , the degree of circular polarization is zero and the degree of linear polarization is described by

$$\text{Degree of linear polarization} = \frac{2A_x A_y}{A_x^2 + A_y^2} = 1. \quad (2.20)$$

Mie theory is a theoretical framework which can be used to exactly solve Maxwell's equations in order to determine the field arising from a plane monochromatic wave incident upon a spherical surface, at which the properties of the medium change abruptly (see fig. 2.1). Although Mie theory has been available for many years, it is only with the advent of fast computers that it has become a practical means for detailed computations.

The following is the derivation of Mie theory as presented by Bohren and Huffman [1].



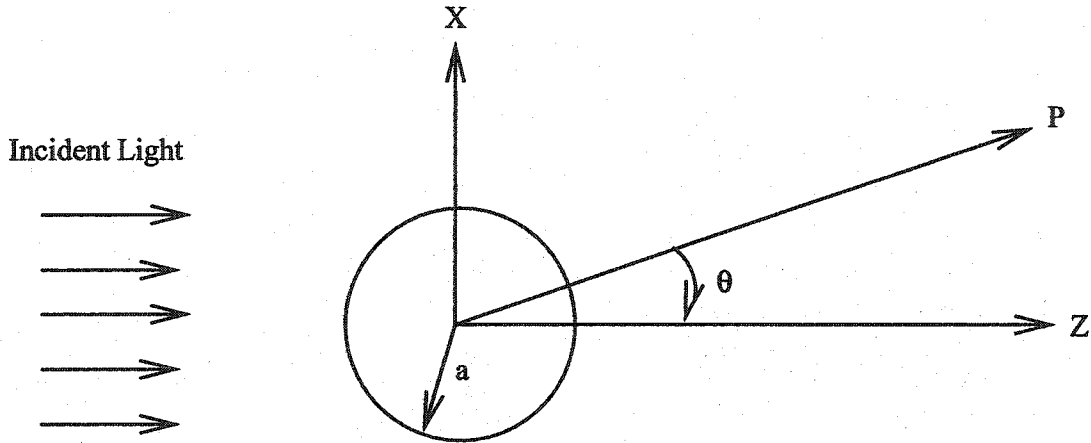


Figure 2.1: Geometry of Mie Theory. The incident field  $(\vec{E}_i, \vec{H}_i)$  gives rise to a field  $(\vec{E}_1, \vec{H}_1)$  inside the dielectric sphere and a scattered field  $(\vec{E}_s, \vec{H}_s)$  in the medium surrounding the sphere.

## 2.2 Solutions to the vector wave equations

We consider a sphere with an infinitely thin interface. The dielectric constant within the sphere is assumed to be  $\epsilon_1$ . That outside is assumed to be equal to  $\epsilon$ . Let us denote the field inside the sphere as  $(\vec{E}_1, \vec{H}_1)$ , while the field outside the sphere  $(\vec{E}_2, \vec{H}_2)$  is a superposition of the incident  $(\vec{E}_i, \vec{H}_i)$  and scattered  $(\vec{E}_s, \vec{H}_s)$  fields

$$\begin{aligned}\vec{E}_2 &= \vec{E}_i + \vec{E}_s \\ \vec{H}_2 &= \vec{H}_i + \vec{H}_s,\end{aligned}\tag{2.21}$$

where

$$\vec{E}_i = \vec{E}_0 \exp(i\vec{k} \cdot \vec{x} - i\omega t)$$

$$\vec{H}_i = \vec{H}_0 \exp(i\vec{k} \cdot \vec{x} - i\omega t),$$

and  $\vec{k}$  is the wave vector in the surrounding medium. In a region with zero free space charge and no free conduction currents, these fields must satisfy the

following Maxwell equations

$$\nabla \cdot \vec{E} = 0 \quad (2.22)$$

$$\nabla \cdot \vec{H} = 0 \quad (2.23)$$

$$\nabla \times \vec{E} = i\omega\mu\vec{H} \quad (2.24)$$

$$\nabla \times \vec{H} = -i\omega\varepsilon\vec{E} \quad (2.25)$$

at all points where  $\varepsilon$  and  $\mu$  are continuous. Taking the curl of (2.24) and (2.25) yields

$$\begin{aligned} \nabla \times (\nabla \times \vec{E}) &= i\omega\mu\nabla \times \vec{H} = \omega^2\varepsilon\mu\vec{E} \\ \nabla \times (\nabla \times \vec{H}) &= -i\omega\mu\nabla \times \vec{E} = \omega^2\varepsilon\mu\vec{H}. \end{aligned} \quad (2.26)$$

We may now use the vector identity

$$\nabla \times (\nabla \times \vec{A}) = \nabla(\nabla \cdot \vec{A}) - \nabla \cdot (\nabla \vec{A})$$

to find

$$\begin{aligned} \nabla^2 \vec{E} + k^2 \vec{E} &= 0 \\ \nabla^2 \vec{H} + k^2 \vec{H} &= 0, \end{aligned} \quad (2.27)$$

where  $k^2 = \omega^2\varepsilon\mu$  and  $\nabla^2 \vec{A} = \nabla \cdot (\nabla \vec{A})$ . Hence, we see that  $\vec{E}$  and  $\vec{H}$  satisfy the vector wave equation.

Let us construct a vector function  $\vec{M}$ ,

$$\vec{M} = \nabla \times (\vec{c}\psi),$$

where  $\psi$  is a scalar function and  $\vec{c}$  is an arbitrary constant vector. Since the divergence of the curl of any vector function vanishes, we have

$$\nabla \cdot \vec{M} = 0,$$

and we may once again use the vector identity

$$\nabla \times (\nabla \times \vec{A}) = \nabla(\nabla \cdot \vec{A}) - \nabla \cdot (\nabla \vec{A})$$

to obtain

$$\nabla^2 \vec{M} + k^2 \vec{M} = \nabla \times [\vec{c}(\nabla^2 \psi + k^2 \psi)]. \quad (2.28)$$

If  $\psi$  is a solution to the scalar wave equation

$$\nabla^2 \psi + k^2 \psi = 0, \quad (2.29)$$

then  $\vec{M}$  satisfies the vector wave equation. We now construct a new vector function  $\vec{N}$ ,

$$\vec{N} = \frac{\nabla \times \vec{M}}{k}.$$

Clearly  $\nabla \cdot \vec{N}$  vanishes, so  $\vec{N}$  satisfies the vector wave equation

$$\nabla^2 \vec{N} + k^2 \vec{N} = 0.$$

It also follows that

$$\nabla \times \vec{N} = k \vec{M}.$$

Let us take stock of what we have accomplished. Starting from a scalar function  $\psi$  (often referred to as a generating function) and an arbitrary vector  $\vec{c}$  (called the guiding or pilot vector), we have constructed two vector functions  $\vec{M}$  and  $\vec{N}$  which possess all the properties of the electromagnetic fields  $\vec{E}$  and  $\vec{H}$ . Therefore, we have reduced the problem of solving Maxwell's equations for the vector fields to having to solve the much simpler scalar wave equation for the generating function  $\psi$ .

In general, whatever generating function we choose depends on the symmetries which may exist in the problem. In much of the work in this thesis we choose a generating function  $\psi$  that satisfies the wave equation in spherical polar

coordinates  $r, \theta, \phi$ . While the pilot vector is completely arbitrary, if we choose  $\vec{c} = \vec{r}$ , the radius vector, then

$$\vec{M} = \nabla \times (\vec{r}\psi), \quad (2.30)$$

and  $\vec{M}$  is a solution to the vector wave equation in spherical polar coordinates. In problems possessing spherical symmetry,  $\vec{M}$  given by (2.30) and the associated  $\vec{N}$  are the fundamental solutions to the field equations.

In spherical polar coordinates, the scalar wave equation is given by

$$\begin{aligned} \frac{1}{r^2} \frac{\partial}{\partial r} (r^2 \frac{\partial \psi}{\partial r}) + \frac{1}{r^2 \sin \theta} \frac{\partial}{\partial \theta} (\sin \theta \frac{\partial \psi}{\partial \theta}) \\ + \frac{1}{r^2 \sin^2 \theta} \frac{\partial^2 \psi}{\partial \phi^2} + k^2 \psi = 0. \end{aligned} \quad (2.31)$$

Using separation of variables,

$$\psi(r, \theta, \phi) = R(r)\Theta(\theta)\Phi(\phi),$$

we obtain three separated equations:

$$\frac{d^2 \Phi}{d\phi^2} + m^2 \Phi = 0, \quad (2.32)$$

$$\frac{1}{\sin \theta} \frac{d}{d\theta} (\sin \theta \frac{d\Theta}{d\theta}) + [n(n+1) - \frac{m^2}{\sin^2 \theta}] \Theta = 0, \quad (2.33)$$

$$\frac{d}{dr} (r^2 \frac{dR}{dr}) + [k^2 r^2 - n(n+1)] R = 0, \quad (2.34)$$

where  $m$  and  $n$  are separation constants which are determined by various constraints on  $\psi$ . For a given  $m$ , the linearly independent solutions to (2.32) are

$$\Phi_e = \cos m\phi, \quad \Phi_o = \sin m\phi,$$

where subscripts  $e$  and  $o$  denote even and odd, respectively. Since we require  $\psi$  to be a single-valued function of the azimuthal angle  $\phi$

$$\psi(\phi + \pi) = \psi(\phi), \quad (2.35)$$

(2.35) requires  $m$  to take on integer values—by convention, we will take  $m = 0, 1, 2, 3, \dots$ , which is sufficient to generate all linearly independent solutions of (2.71).

The solutions to (2.70) are the associated Legendre functions of the first kind  $P_n^m(\cos \theta)$  of degree  $n$  and order  $m$ , where  $n = m, m + 1, \dots$ . These functions are orthogonal, finite at  $\theta = 0$  and  $\theta = \pi$ , and reduce to the Legendre polynomials, denoted by  $P_n$ , when  $m = 0$ .

Introducing the dimensionless variable  $\rho = kr$  and defining the function  $Z = R\sqrt{\rho}$ , we may rewrite (2.34) as

$$\rho \frac{d}{d\rho} \left( \rho \frac{dZ}{d\rho} \right) + [\rho^2 - (n + \frac{1}{2})^2] Z = 0. \quad (2.36)$$

Equation (2.36) is solved by the Bessel functions of the first and second kind,  $J_\nu$  and  $Y_\nu$ , of half-integral the order  $\nu = n + \frac{1}{2}$ . For notational convenience, we introduce the spherical Bessel functions

$$\begin{aligned} j_n &= \sqrt{\frac{\pi}{2\rho}} J_{n+1/2}(\rho) \\ y_n &= \sqrt{\frac{\pi}{2\rho}} Y_{n+1/2}(\rho). \end{aligned} \quad (2.37)$$

Any linear combination of  $j_n$  and  $y_n$  is also a solution to (2.34). For example, the spherical Bessel functions of the third kind (often called the spherical Hankel functions),

$$\begin{aligned} h_n^{(1)} &= j_n(\rho) + iy_n(\rho) \\ h_n^{(2)} &= j_n(\rho) - iy_n(\rho) \end{aligned} \quad (2.38)$$

are often useful. Therefore, our generating functions take the form

$$\begin{aligned} \psi_{emn} &= \cos m\phi P_n^m(\cos \theta) z_n(kr) \\ \psi_{omn} &= \sin m\phi P_n^m(\cos \theta) z_n(kr), \end{aligned} \quad (2.39)$$

where  $z_n$  is any one of the four spherical Bessel functions  $j_n$ ,  $y_n$ ,  $h_n^{(1)}$ , or  $h_n^{(2)}$ . Any function that satisfies the scalar wave equation in spherical polar coordinates may be expanded as an infinite series in the functions (2.39). Moreover, we may now generate our vector spherical harmonics from  $\psi_{emn}$  and  $\psi_{omn}$ , obtaining:

$$\begin{aligned} \vec{M}_{emn} &= \frac{-m}{\sin \theta} \sin m\phi P_n^m(\cos \theta) z_n(\rho) \vec{e}_\theta \\ &\quad - \cos m\phi \frac{dP_n^m(\cos \theta)}{d\theta} z_n(\rho) \vec{e}_\phi, \end{aligned} \quad (2.40)$$

$$\begin{aligned} \vec{M}_{omn} &= \frac{m}{\sin \theta} \cos m\phi P_n^m(\cos \theta) z_n(\rho) \vec{e}_\theta \\ &\quad - \sin m\phi \frac{dP_n^m(\cos \theta)}{d\theta} z_n(\rho) \vec{e}_\phi, \end{aligned} \quad (2.41)$$

$$\begin{aligned} \vec{N}_{emn} &= \frac{z_n(\rho)}{\rho} \cos m\phi n(n+1) P_n^m(\cos \theta) \vec{e}_r \\ &\quad + \cos m\phi \frac{dP_n^m(\cos \theta)}{d\theta} \frac{1}{\rho} \frac{d}{d\rho} [\rho z_n(\rho)] \vec{e}_\theta \\ &\quad - m \sin m\phi \frac{P_n^m(\cos \theta)}{\sin \theta} \frac{1}{\rho} \frac{d}{d\rho} [\rho z_n(\rho)] \vec{e}_\phi, \end{aligned} \quad (2.42)$$

$$\begin{aligned} \vec{N}_{omn} &= \frac{z_n(\rho)}{\rho} \sin m\phi n(n+1) P_n^m(\cos \theta) \vec{e}_r \\ &\quad + \sin m\phi \frac{dP_n^m(\cos \theta)}{d\theta} \frac{1}{\rho} \frac{d}{d\rho} [\rho z_n(\rho)] \vec{e}_\theta \\ &\quad + m \cos m\phi \frac{P_n^m(\cos \theta)}{\sin \theta} \frac{1}{\rho} \frac{d}{d\rho} [\rho z_n(\rho)] \vec{e}_\phi. \end{aligned} \quad (2.43)$$

Any solution to the field equations can now be expanded in an infinite series of these functions (2.40–2.43).

## 2.3 Expansion of a Plane Wave in Vector Spherical Harmonics

In this section, we outline how to determine the coefficients of the expansion of a plane wave in vector spherical harmonics.

In spherical polar coordinates, a plane  $x$ -polarized wave may take the form

$$\vec{E}_i = E_0 e^{ikr \cos \theta} (\sin \theta \cos \phi \vec{e}_r + \cos \theta \cos \phi \vec{e}_\theta - \sin \phi \vec{e}_\phi), \quad (2.44)$$

and we may expand (2.44) in vector spherical harmonics as

$$\vec{E}_i = \sum_{m=0}^{\infty} \sum_{n=m}^{\infty} (B_{emn} \vec{M}_{emn} + B_{omn} \vec{M}_{omn} + A_{emn} \vec{N}_{emn} + A_{omn} \vec{N}_{omn}). \quad (2.45)$$

From the orthogonality of the vector spherical harmonics, we have that the coefficients in the expansion (2.45) take the form

$$B_{emn} = \frac{\int_0^{2\pi} \int_0^\pi \vec{E}_i \cdot \vec{M}_{emn} \sin \theta d\theta d\phi}{\int_0^{2\pi} \int_0^\pi |\vec{M}_{emn}|^2 \sin \theta d\theta d\phi}, \quad (2.46)$$

with analogous expressions for  $B_{omn}$ ,  $A_{emn}$ , and  $A_{omn}$ . Combining (2.40), (2.43), and (2.44) with the orthogonality of sine and cosine, we have  $B_{emn} = A_{omn} = 0$  for all  $m$  and  $n$ . Moreover, for the same reason, the remaining coefficients vanish unless  $m = 1$ . At the origin, the incident field should be finite, but since  $y_n$  blows up at the origin, we must choose  $j_n(kr)$  as the spherical Bessel function in the generating functions  $\psi_{o1n}$  and  $\psi_{e1n}$ . Notationally, we will denote vector harmonics whose radial dependence of the generating function is specified by  $j_n$  with superscript (1). Hence, the expansion for  $\vec{E}_i$  has the form

$$\vec{E}_i = \sum_{n=1}^{\infty} (B_{o1n} \vec{M}_{o1n}^{(1)} + A_{e1n} \vec{N}_{e1n}^{(1)}). \quad (2.47)$$

By evaluating integrals of the expressions for  $B_{o1n}$  and  $A_{e1n}$ , the expansion coefficients take the form

$$\begin{aligned} B_{o1n} &= i^n E_0 \frac{2n+1}{n(n+1)} \\ A_{e1n} &= -i E_0 i^n \frac{2n+1}{n(n+1)}. \end{aligned} \quad (2.48)$$

Therefore, the expansion of a plane wave in spherical harmonics has the form

$$\vec{E}_i = E_0 \sum_{n=1}^{\infty} i^n \frac{2n+1}{n(n+1)} (\vec{M}_{o1n}^{(1)} - i \vec{N}_{e1n}^{(1)}), \quad (2.49)$$

and from the curl of (2.49), we obtain the expansion of the corresponding incident magnetic field in spherical harmonics

$$\vec{H}_i = \frac{-k}{\omega\mu} E_0 \sum_{n=1}^{\infty} i^n \frac{2n+1}{n(n+1)} (\vec{M}_{o1n}^{(1)} + i\vec{N}_{e1n}^{(1)}). \quad (2.50)$$

## 2.4 The Internal and Scattered Fields

Consider a plane wave polarized in the  $x$ -direction being scattered by a homogeneous, isotropic sphere of radius  $a$  Figure 2.1. By using the boundary conditions

$$(\vec{E}_i + \vec{E}_s - \vec{E}_1) \times \vec{e}_r = (\vec{H}_i + \vec{H}_s - \vec{H}_1) \times \vec{e}_r = 0 \quad (2.51)$$

between the sphere and the surrounding medium, we may expand the scattered electromagnetic field  $(\vec{E}_s, \vec{H}_s)$  and the field  $(\vec{E}_1, \vec{H}_1)$  inside the sphere in vector spherical harmonics. As we saw above, the boundary conditions (2.51), orthogonality of the vector harmonics, and form of the expansion of the incident field force the coefficients in these expansions to vanish for all  $m \neq 1$ .

In the region inside the sphere, finiteness once again requires that we choose  $j_n(k_1 r)$ , where  $k_1$  is the wave number in the sphere, as the spherical Bessel functions in the generating functions. Therefore, the expansion of the field  $(\vec{E}_1, \vec{H}_1)$  is

$$\begin{aligned} \vec{E}_1 &= \sum_{n=1}^{\infty} E_n (c_n \vec{M}_{o1n}^{(1)} - i d_n \vec{N}_{e1n}^{(1)}) \\ \vec{H}_1 &= \frac{-k_1}{\omega\mu_1} \sum_{n=1}^{\infty} E_n (d_n \vec{M}_{e1n}^{(1)} + i c_n \vec{N}_{o1n}^{(1)}), \end{aligned} \quad (2.52)$$

where  $E_n = i^n E_0 (2n+1)/(n(n+1))$  and  $\mu_1$  is the permeability of the sphere.

On the other hand, both  $j_n$  and  $y_n$  are well behaved in the region outside the sphere. Therefore, we will consider the spherical Hankel functions  $h_n^{(1)}$  and  $h_n^{(2)}$  which have the asymptotic form

$$h_n^{(1)}(kr) \sim \frac{(-i)^n e^{ikr}}{ikr} \quad (2.53)$$



$$h_n^{(2)}(kr) \sim -\frac{i^n e^{-ikr}}{ikr} \quad kr \gg n^2 \quad (2.54)$$

It is clear that  $h_n^{(1)}(kr)$  corresponds to an outgoing spherical wave while  $h_n^{(2)}(kr)$  corresponds to an incoming spherical wave. Since the scattered field is to be an outgoing wave at large distance from the sphere, only  $h_n^{(1)}$  should be used in the generating functions. Therefore, the expansion of the scattered field ( $\vec{E}_s, \vec{H}_s$ ) should be given by

$$\begin{aligned} \vec{E}_s &= \sum_{n=1}^{\infty} E_n (ia_n \vec{N}_{e1n}^{(3)} - b_n \vec{M}_{o1n}^{(3)}) \\ \vec{H}_s &= \frac{k}{\omega\mu} \sum_{n=1}^{\infty} E_n (ib_n \vec{N}_{o1n}^{(3)} + a_n \vec{M}_{e1n}^{(3)}), \end{aligned} \quad (2.55)$$

where the superscript (3) denote vector spherical harmonics whose generating functions radial dependence is specified by  $h_n^{(1)}$ .

We notice that, for a given  $n$ , there are four unknown coefficients  $a_n$ ,  $b_n$ ,  $c_n$ , and  $d_n$  in the expansions of the scattered and internal fields. We therefore require four independent equations to solve for these four unknown coefficients. From the boundary conditions (2.51) in component form:

$$\begin{aligned} E_{i\theta} + E_{s\theta} &= E_{1\theta}, & E_{i\phi} + E_{s\phi} &= E_{1\phi}, \\ H_{i\theta} + H_{s\theta} &= H_{1\theta}, & H_{i\phi} + H_{s\phi} &= H_{1\phi}, \quad r = a, \end{aligned} \quad (2.56)$$

we eventually obtain four linear equations from which we may determine expressions for the four coefficients. We are primarily interested in  $a_n$  and  $b_n$ , which are called scattering coefficients and are given by

$$\begin{aligned} a_n &= \frac{m\psi_n(mx)\psi_n'(x) - \psi_n(x)\psi_n'(mx)}{m\psi_n(mx)\xi_n'(x) - \xi_n(x)\psi_n'(mx)} \\ b_n &= \frac{\psi_n(mx)\psi_n'(x) - m\psi_n(x)\psi_n'(mx)}{\psi_n(mx)\xi_n'(x) - m\xi_n(x)\psi_n'(mx)}, \end{aligned} \quad (2.57)$$

where  $\psi_n(\rho)$  and  $\xi_n(\rho)$  are the Riccati-Bessel functions:

$$\psi_n(\rho) = \rho j_n(\rho), \quad \xi_n(\rho) = \rho h_n^{(1)}(\rho),$$

while

$$x = ka = \frac{2\pi Na}{\lambda_0}, \quad m = \frac{k_1}{k} = \frac{N_1}{N},$$

are the size parameter and the relative refractive index, respectively.  $N_1$  is the refractive index of the sphere and  $N$  is the refractive indices of the medium.

Note that  $a_n$  and  $b_n$  vanish as  $m$  approaches unity, because when the sphere disappears, so does the scattered field.

For convenience, let us define angle-dependent functions  $\pi_n$  and  $\tau_n$

$$\begin{aligned} \pi_n &= \frac{P_n^l}{\sin \theta} \\ \tau_n &= \frac{dP_n^l}{d\theta}, \end{aligned} \quad (2.58)$$

which can be built up through use of the recurrence relations

$$\begin{aligned} \pi_n &= \frac{2n-1}{n-1} \cos \theta \pi_{n-1} - \frac{n}{n-1} \pi_{n-2} \\ \tau_n &= n \cos \theta \pi_n - (n+1) \pi_{n-1}, \end{aligned} \quad (2.59)$$

beginning with  $\pi_0 = 0$  and  $\pi_1 = 1$ .  $\pi_n$  and  $\tau_n$  are alternately even and odd functions of  $\cos \theta$

$$\begin{aligned} \pi_n(-\cos \theta) &= (-1)^{n-1} \pi_n(\cos \theta) \\ \tau_n(-\cos \theta) &= (-1)^n \tau_n(\cos \theta), \end{aligned} \quad (2.60)$$

while  $\pi_n + \tau_n$  and  $\pi_n - \tau_n$  are orthogonal sets of functions

$$\begin{aligned} \int_0^\pi (\pi_n + \tau_n)(\pi_m + \tau_m) \sin \theta d\theta &= \int_0^\pi (\pi_n - \tau_n)(\pi_m - \tau_m) \sin \theta d\theta = 0 \\ (m \neq n). \end{aligned} \quad (2.61)$$

Using the angle-dependent functions  $\pi_n$  and  $\tau_n$  (with  $m = 1$ ), we may express the vector harmonics (2.40–2.43) which are used in the expansions of the internal (2.52) and scattered (2.55) fields in a more concise manner as follows

$$\begin{aligned}
 M_{o1n} &= \cos \phi \pi_n(\cos \theta) z_n(\rho) \vec{e}_\theta - \sin \phi \tau_n(\cos \theta) z_n(\rho) \vec{e}_\phi \\
 M_{e1n} &= -\sin \phi \pi_n(\cos \theta) z_n(\rho) \vec{e}_\theta - \cos \phi \tau_n(\cos \theta) z_n(\rho) \vec{e}_\phi \\
 N_{o1n} &= \sin \phi n(n+1) \sin \theta \pi_n(\cos \theta) \frac{z_n(\rho)}{\rho} \vec{e}_r \\
 &\quad + \sin \phi \tau_n(\cos \theta) \frac{[\rho z_n(\rho)]'}{\rho} \vec{e}_\theta + \cos \phi \pi_n(\cos \theta) \frac{[\rho z_n(\rho)]'}{\rho} \vec{e}_\phi \\
 N_{e1n} &= \cos \phi n(n+1) \sin \theta \pi_n(\cos \theta) \frac{z_n(\rho)}{\rho} \vec{e}_r \\
 &\quad + \cos \phi \tau_n(\cos \theta) \frac{[\rho z_n(\rho)]'}{\rho} \vec{e}_\theta - \sin \phi \pi_n(\cos \theta) \frac{[\rho z_n(\rho)]'}{\rho} \vec{e}_\phi \quad (2.62)
 \end{aligned}$$

## 2.5 Scattering Matrix—Mueller Matrix

Figure 2.2 shows a cell illuminated by a plane wave. The propagation direction of the incident light is taken to lie along the  $Z$  axis, which we shall call the forward direction. The centre of the cell is chosen as the origin of a Cartesian coordinate system  $(x, y, z)$ , with the  $X$  and  $Y$  axes orthogonal to the  $Z$  axis and to each other. The scattering plane (see Fig. 2.2) is defined by the scattering direction  $\hat{e}_r$  and the forward direction  $\hat{e}_z$ . When  $\hat{e}_r$  is not parallel to the  $Z$  axis, the scattering plane is uniquely determined by the azimuthal angle  $\phi$ . On the other hand, when  $\hat{e}_r$  is equal to  $\pm \hat{e}_z$ , any plane containing the  $Z$  axis is a suitable scattering plane.

We introduce two new orthonormal basis vectors for the incident light;  $\hat{e}_{\parallel i}$ , which is parallel to the scattering plane, and  $\hat{e}_{\perp i}$ , which is perpendicular to the scattering plane. Therefore, an incident electric field  $\vec{E}_i$ , which lies in the  $xy$  plane,

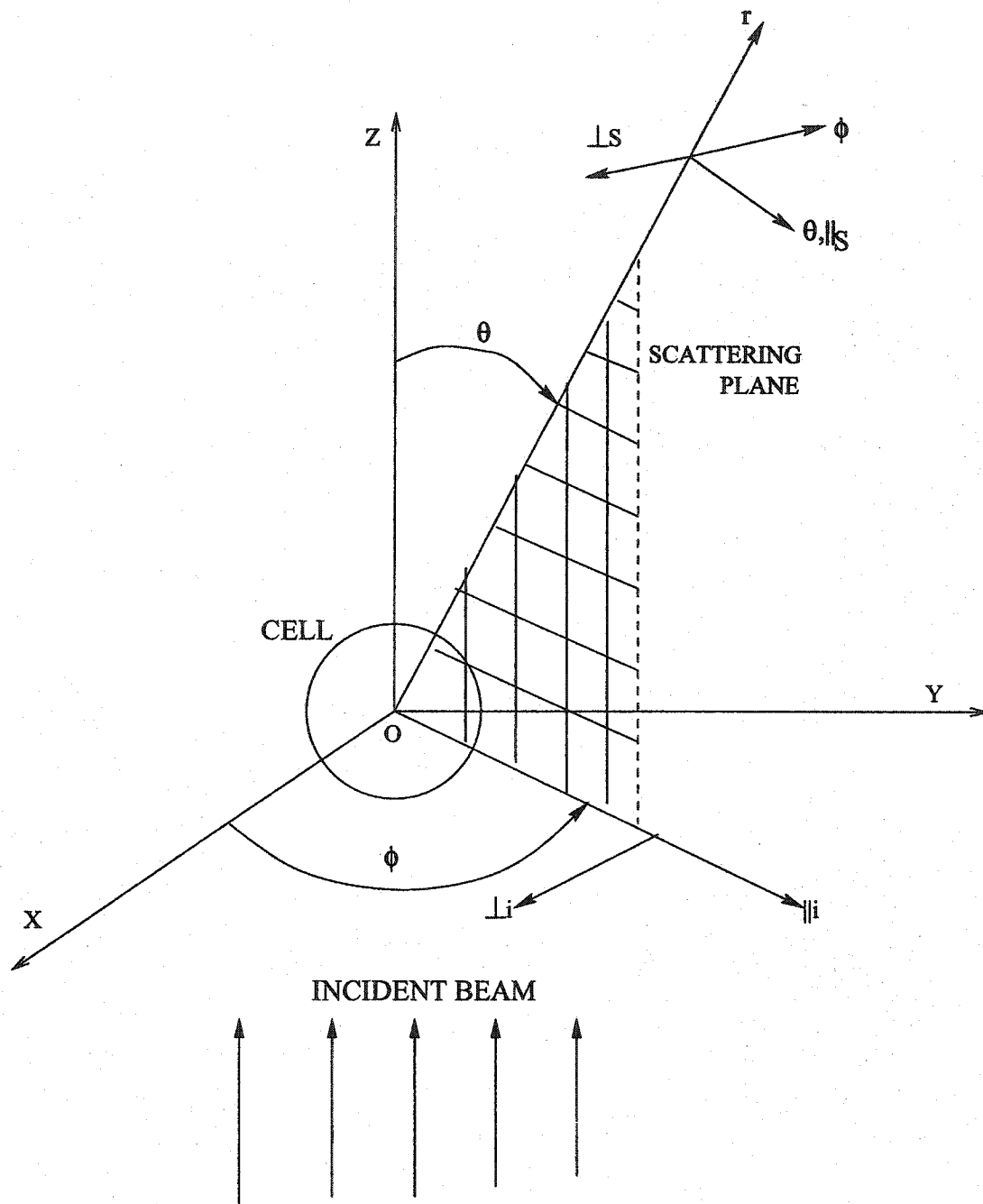


Figure 2.2: Incident beam scattered by a cell.

can be resolved into parallel component  $E_{\parallel i}$  and perpendicular component  $E_{\perp i}$ :

$$\vec{E}_i = E_{\parallel i} \hat{e}_{\parallel i} + E_{\perp i} \hat{e}_{\perp i}. \quad (2.63)$$

These new orthonormal basis vectors  $\hat{e}_{\perp i}$  and  $\hat{e}_{\parallel i}$  form a right-handed triad with  $\hat{e}_z$ :

$$\hat{e}_{\perp i} \times \hat{e}_{\parallel i} = \hat{e}_z, \quad (2.64)$$

and we have

$$\begin{aligned} \hat{e}_{\perp i} &= \sin \phi \hat{e}_x - \cos \phi \hat{e}_y, \\ \hat{e}_{\parallel i} &= \cos \phi \hat{e}_x + \sin \phi \hat{e}_y. \end{aligned} \quad (2.65)$$

Moreover,

$$\begin{aligned} \hat{e}_{\perp i} &= -\hat{e}_\phi, \\ \hat{e}_{\parallel i} &= \sin \theta \hat{e}_r + \cos \theta \hat{e}_\theta, \end{aligned}$$

where  $\hat{e}_r$ ,  $\hat{e}_\theta$ , and  $\hat{e}_\phi$  are the orthonormal basis vectors of the spherical polar coordinate system  $(r, \theta, \phi)$ . Using Eq. (2.65), the components  $E_{\perp i}$  and  $E_{\parallel i}$  of incident electric field take the following forms

$$E_{\perp i} = \sin \phi E_{xi} - \cos \phi E_{yi}, \quad (2.66)$$

$$E_{\parallel i} = \cos \phi E_{xi} + \sin \phi E_{yi}, \quad (2.67)$$

where  $E_{xi}$  and  $E_{yi}$  stand for the  $x$  and  $y$  components of the incident electric field.

In the far-field ( $kr \gg 1$ ), the scattered electric field  $\vec{E}_s$  is approximately transverse ( $\vec{E}_s \cdot \hat{e}_r \simeq 0$ ) [2]. So that in the far-field region, the scattered electric field takes form

$$\vec{E}_s = E_{\parallel s} \hat{e}_{\parallel s} + E_{\perp s} \hat{e}_{\perp s}, \quad (2.68)$$

where the basis vectors  $\hat{e}_{\parallel s}$  and  $\hat{e}_{\perp s}$  are respectively parallel and perpendicular to the scattering plane, and have the following properties

$$\hat{e}_{\parallel s} = \hat{e}_\theta \quad (2.69)$$

$$\hat{e}_{\perp s} = -\hat{e}_{\phi} \quad (2.70)$$

$$\hat{e}_{\perp s} \times \hat{e}_{\parallel s} = \hat{e}_r. \quad (2.71)$$

If we assume that the series expansion (2.55) of the scattering field is uniformly convergent, we can terminate the series after  $n_c$  terms. When  $n_c$  is sufficiently large, the resulting error is very small. In addition, for  $kr \gg n_c^2$ , we may replace  $h_n^{(1)}(kr)$  with its asymptotic expression (2.53) in the truncated series. The transverse components of the scattering electric field are then given by

$$E_{s\theta} \sim E_0 \frac{e^{ikr}}{-ikr} \cos \phi S_2(\cos \theta) \quad (2.72)$$

$$E_{s\phi} \sim -E_0 \frac{e^{ikr}}{-ikr} \sin \phi S_1(\cos \theta) \quad (2.73)$$

where

$$S_1 = \sum_{n=0}^{n_c} \frac{2n+1}{n(n+1)} (a_n \pi_n + b_n \tau_n)$$

$$S_2 = \sum_{n=0}^{n_c} \frac{2n+1}{n(n+1)} (a_n \tau_n + b_n \pi_n). \quad (2.74)$$

Using Eqs. (2.44), (2.67), (2.67), (2.70), and (2.71), we may express our results for the scattered field Eqs. (2.72) and (2.73) in terms of the incident field as follows:

$$E_{\parallel s} \sim E_{\parallel i} \frac{e^{ikr}}{-ikr} S_2(\cos \theta), \quad (2.75)$$

$$E_{\perp s} \sim E_{\perp i} \frac{e^{ikr}}{-ikr} S_1(\cos \theta), \quad (2.76)$$

Therefore, the incident and scattered field amplitudes are related as follows

$$\begin{pmatrix} E_{\parallel s} \\ E_{\perp s} \end{pmatrix} = \frac{e^{ik(r-z)}}{-ikr} \begin{pmatrix} S_2 & 0 \\ 0 & S_1 \end{pmatrix} \begin{pmatrix} E_{\parallel i} \\ E_{\perp i} \end{pmatrix}. \quad (2.77)$$

Since basis vectors  $\hat{e}_{\parallel s}$  and  $\hat{e}_{\perp s}$  form a part of an orthonormal set of basis vectors, following the discussion in section 2.1, we have

$$\begin{aligned}
I_s &= E_{\parallel s} E_{\parallel s}^* + E_{\perp s} E_{\perp s}^*, \\
Q_s &= E_{\parallel s} E_{\parallel s}^* - E_{\perp s} E_{\perp s}^*, \\
U_s &= E_{\parallel s} E_{\perp s}^* + E_{\perp s} E_{\parallel s}^*, \\
V_s &= i(E_{\parallel s} E_{\perp s}^* - E_{\perp s} E_{\parallel s}^*).
\end{aligned} \tag{2.78}$$

Substituting Eq. (2.77) into Eq. (2.79), the scattered Stokes parameters are related to the incident Stokes parameters by the relation

$$\begin{pmatrix} I_s \\ Q_s \\ U_s \\ V_s \end{pmatrix} = \frac{1}{k^2 r^2} \begin{pmatrix} M_{11} & M_{12} & 0 & 0 \\ M_{12} & M_{11} & 0 & 0 \\ 0 & 0 & M_{33} & M_{34} \\ 0 & 0 & -M_{34} & M_{33} \end{pmatrix} \begin{pmatrix} I_i \\ Q_i \\ U_i \\ V_i \end{pmatrix}, \tag{2.79}$$

where the Mueller matrix elements have the form

$$\begin{aligned}
M_{11} &= \frac{1}{2}(|S_2|^2 + |S_1|^2), & M_{12} &= \frac{1}{2}(|S_2|^2 - |S_1|^2), \\
M_{33} &= \frac{1}{2}(S_2^* S_1 + S_2 S_1^*), & M_{34} &= \frac{i}{2}(S_1 S_2^* - S_2 S_1^*),
\end{aligned}$$

and the incident Stokes parameters take the following forms:

$$\begin{aligned}
I_i &= E_{\parallel i} E_{\parallel i}^* + E_{\perp i} E_{\perp i}^*, \\
Q_i &= E_{\parallel i} E_{\parallel i}^* - E_{\perp i} E_{\perp i}^*, \\
U_i &= E_{\parallel i} E_{\perp i}^* + E_{\perp i} E_{\parallel i}^*, \\
V_i &= i(E_{\parallel i} E_{\perp i}^* - E_{\perp i} E_{\parallel i}^*).
\end{aligned} \tag{2.80}$$

Only three of these four matrix elements are independent:  $M_{11}^2 = M_{12}^2 + M_{33}^2 + M_{34}^2$ . The factor  $1/k^2 r^2$  is usually omitted in the calculations.

When the incident light is polarized parallel to a particular scattering plane:  $E_{\perp i} = 0$ , then the Stokes parameters of incident light Eq. (2.81) becomes

$$I_i = E_{\parallel i} E_{\parallel i}^*,$$

$$\begin{aligned} Q_i &= I_i, \\ V_i &= U_i = 0, \end{aligned} \quad (2.81)$$

and the corresponding scattered Stokes parameters are

$$\begin{aligned} I_s &= (M_{11} + M_{12})I_i, \\ Q_s &= I_s, \\ U_s &= V_s = 0. \end{aligned} \quad (2.82)$$

Therefore, the scattered light is polarized parallel to the scattering plane. In the case of the incident light being parallel to the scattering plane, let us denote the scattered irradiance per unit incident irradiance  $i_{\parallel}$ :

$$i_{\parallel} = M_{11} + M_{12} = |S_2|^2. \quad (2.83)$$

Similarly, when the incident light is polarized perpendicular to the scattering plane, the Stokes parameters of incident light Eq. (2.81) are now given by

$$\begin{aligned} I_i &= E_{\perp i} E_{\perp i}^*, \\ Q_i &= -I_i, \\ V_i &= U_i = 0, \end{aligned} \quad (2.84)$$

and the corresponding scattered Stokes parameters are

$$\begin{aligned} I_s &= (M_{11} - M_{12})I_i, \\ Q_s &= -I_s, \\ U_s &= V_s = 0. \end{aligned} \quad (2.85)$$

Therefore, the scattered light is perpendicularly polarized with respect to the scattering plane. In the case of incident light being perpendicular to the scattering plane, let us denote the scattered irradiance per unit incident irradiance



$i_{\perp}$ :

$$i_{\perp} = M_{11} - M_{12} = |S_1|^2. \quad (2.86)$$

When the incident light is unpolarized, then the only non-zero Stokes parameter is  $I_i$ . Therefore, the corresponding scattered Stokes parameters are

$$\begin{aligned} I_s &= M_{11}I_i, \\ Q_s &= M_{12}I_i, \\ U_s &= V_s = 0. \end{aligned} \quad (2.87)$$

Using Eq. (2.19), the total degree of polarization  $P$  is given by

$$P = \frac{M_{12}}{M_{11}} = \frac{i_{\parallel} - i_{\perp}}{i_{\parallel} + i_{\perp}}, \quad (2.88)$$

it follows that  $|P| \leq 1$ . If  $P$  is positive, the scattered light is partially polarized parallel to the scattering plane; if  $P$  is negative, the scattered light is partially polarized perpendicular to the scattering plane. From the definitions of the angle-dependent functions  $\pi_n$  and  $\tau_n$  (2.58) and their recurrence relations (2.59), we have

$$\pi_n(1) = \tau_n(1) = \frac{n(n+1)}{2} \quad (2.89)$$

Thus, in the forward direction ( $\theta = 0^\circ$ ) and backward direction ( $\theta = 180^\circ$ ), Eq. (2.74) is reduced to

$$S_1(1) = S_2(1) = S(1) = \frac{1}{2} \sum_{n=0}^{n_c} (2n+1)(a_n + b_n), \quad (2.90)$$

which gives  $M_{12} = 0$  for both directions of forward and backward scattering. Hence, regardless of the size and composition of the cell,  $P(0^\circ) = P(180^\circ) = 0$ .

## 2.6 Computations of Mie Theory

By introducing the logarithmic derivative

$$D_n(\rho) = \frac{d}{d\rho} \ln \psi_n(\rho), \quad (2.91)$$

the scattering coefficients  $a_n$  and  $b_n$  (2.57) may be rewritten as

$$\begin{aligned} a_n &= \frac{[D_n(mx)/m + n/x]\psi_n(x) - \psi_{n-1}(x)}{[D_n(mx)/m + n/x]\xi_n(x) - \xi_{n-1}(x)} \\ b_n &= \frac{[mD_n(mx)/m + n/x]\psi_n(x) - \psi_{n-1}(x)}{[mD_n(mx)/m + n/x]\xi_n(x) - \xi_{n-1}(x)}, \end{aligned} \quad (2.92)$$

where we have used the recurrence relations

$$\begin{aligned} \psi'_n(x) &= \psi_{n-1}(x) - \frac{n\psi_n(x)}{x} \\ \xi'_n(x) &= \xi_{n-1}(x) - \frac{n\xi_n(x)}{x}, \end{aligned}$$

to eliminate  $\psi'_n$  and  $\xi'_n$ . This represents just one of many possible ways of rewriting the scattering coefficients in a form more suitable for computation. As a consequence of the recurrence relations of the Bessel functions, the logarithmic derivative also satisfies a recurrence relation

$$D_{n-1} = \frac{n}{\rho} - \frac{1}{D_n + n/\rho} \quad (2.93)$$

We may therefore use this downward recurrence to compute  $D_n$  in order to ensure numerical stability.

A modified version of the Mie code was developed based on the above discussion. In order to verify this code, we chose the same parameters, which are  $a/\lambda = 1$  and  $N_1/N = 1.59/1.33$ , as in [3]. Figure 2.3 (a) shows the average scattered intensity  $M_{11} = (i_{\parallel} + i_{\perp})/2$  vs scattering angle, while (b) shows the degree of linear polarization ( $-P$ ) as defined in equation (2.88) (note that the negative signs results from a difference in sign convention between this work and ref [1].) vs scattering angle when the incident laser light is unpolarized. Our results are excellent agreement with those presented in [3]. Furthermore, the scattered intensity  $i_{\parallel}$  polarized parallel to a scattering plane (it can be an arbitrary scattering plane depending on a given azimuthal angle  $\phi$ , refer to Fig. 2.2) and the scattered intensity  $i_{\perp}$  polarized perpendicular to the scattering plane

are presented in Figure 2.3 (a). This modified version of Mie code can be used in the description of arbitrarily polarized light that is scattered by a homogeneous sphere. Figure 2.4 shows the computational results of Mie theory with the parameters  $a/\lambda = 5.5$  and  $N_1/N = 1.37/1.35$ .

There are three curves in Fig. 2.4 (a) which stand for the average scattered intensity (solid line), the scattered intensity  $i_{\parallel}$  polarized parallel (dashed line) to and the scattered intensity  $i_{\perp}$  polarized perpendicular (dotted line) to the scattering plane, respectively. Fig. 2.4 (b) shows the degree of polarization of the scattered light when the incident light is unpolarized. In both forward (at  $0^\circ$ ) and backward (at  $180^\circ$ ) directions, the scattered light remains unpolarized ( $P(0^\circ) = P(180^\circ) = 0$ ). However, in the range of  $80^\circ$  to  $100^\circ$ , the scattered light is almost completely polarized perpendicular to the scattering plane ( $P \simeq 1$ ). These computational results will be used as a benchmark for our numerical simulations.

In conclusion, we have seen that when the incident light is 100% polarized parallel to the scattering plane, the scattered light is also polarized parallel to the scattering plane. When the incident light is 100% polarized perpendicular to the scattering plane, then the scattered light is also polarized parallel to the scattering plane. We have also seen that polarization may result for certain scattering angles if the incident light is itself unpolarized.

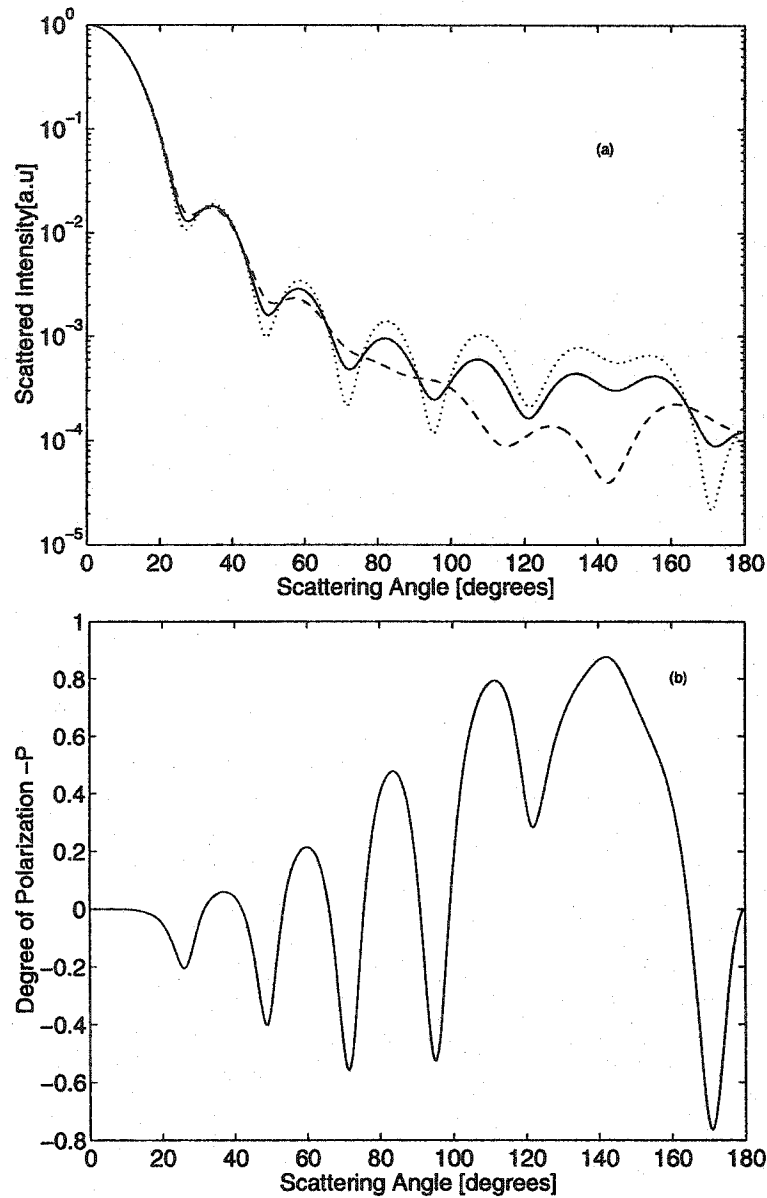


Figure 2.3: The computational results of Mie theory with parameters of  $a/\lambda = 1$  and  $N_1/N = 1.59/1.33$ . In Fig. (a), the solid line is for the average scattered intensity  $M_{11} = (i_{\parallel} + i_{\perp})/2$ ; the dashed line is for the scattered intensity  $i_{\parallel}$  polarized parallel to the scattering plane; and the dotted line is for the scattered intensity  $i_{\perp}$  polarized perpendicular to the scattering plane. Fig. (b) show the degree of polarization when the incident light is unpolarized.

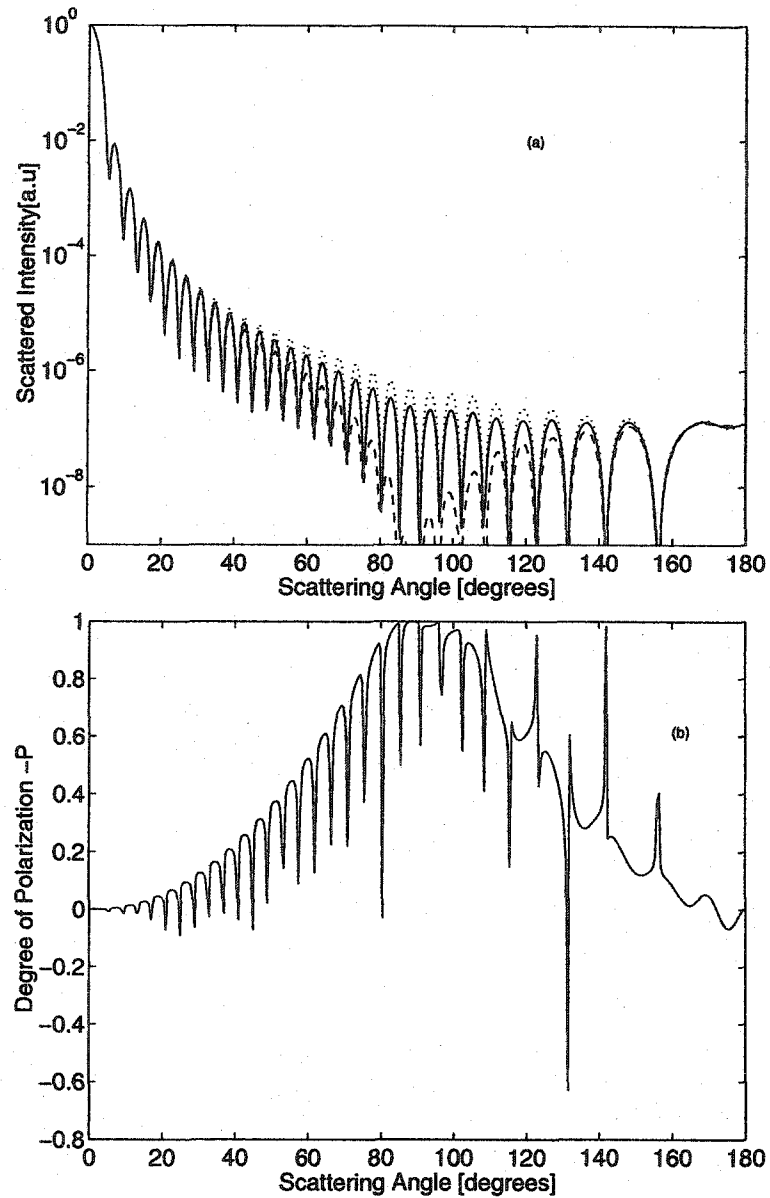


Figure 2.4: The computational results of Mie theory with the parameters of  $a/\lambda = 5.5$  and  $N_1/N = 1.37/1.35$ . In Fig. (a) three curves stand for the average scattered intensity (solid line), the scattered intensity  $i_{\parallel}$  polarized parallel (dash line) to and the scattered intensity  $i_{\perp}$  polarized perpendicular (dot line) to the scattering plane, respectively. Fig. (b) shows the degree of polarization of the scattered light when the incident light is unpolarized.

## Bibliography

- [1] C. F. Bohren and D. R. Huffman, *Absorption and Scattering of Light by Small particles*, (Wiley, New York, 1983)
- [2] J. D. Jackson, *Classical Electrodynamics*. New York: Wiley, 1974
- [3] D. Maitland, V. Sankaran, P. Amendt, R. London and G. Zimmerman, *Monte Carlo simulations of polarization light propagation in microsphere suspensions*, A Seminar on Medical Technology Program at LLNL

## Chapter 3

# The Computational Model

### 3.1 Basic Equations

The computational model used for the scattering problems considered in this thesis is based on solving the wave equation for the amplitude of the laser light by using the spectral method. This method allows us to model the interaction of laser light with biological specimens whose physical size can vary over a wide range of spatial scale lengths, from sub-wavelength dimensions up to a few orders of magnitude larger than the laser wavelength.

Maxwell's equations in a nonconducting medium take the following form[1]:

$$\nabla \cdot \epsilon \vec{E} = 0 \quad (3.1)$$

$$\nabla \cdot \vec{B} = 0 \quad (3.2)$$

$$\nabla \times \vec{E} + \frac{1}{c} \frac{\partial \vec{B}}{\partial t} = 0 \quad (3.3)$$

$$\nabla \times \vec{B} - \frac{\mu \epsilon}{c} \frac{\partial \vec{E}}{\partial t} = 0, \quad (3.4)$$

where  $\vec{E}$  and  $\vec{B}$  are the electric and magnetic fields, respectively;  $c$  is the speed of light in vacuum; and  $\mu$  and  $\epsilon$  stand for the magnetic permeability and the

dielectric constant of the medium, respectively. By taking the curl of Eq. (3.3) and substituting for  $\nabla \times \vec{B}$  by using Eq. (3.4), the full set of Maxwell equations (3.1—3.4) in three spatial dimensions is reduced to a wave equation for the electric field amplitude,

$$\frac{\mu\epsilon}{c^2} \frac{\partial^2 \vec{E}}{\partial t^2} - \nabla^2 \vec{E} + \nabla(\nabla \cdot \vec{E}) = 0, \quad (3.5)$$

where we have used the vector identity

$$\nabla \times (\nabla \times \vec{A}) = \nabla(\nabla \cdot \vec{A}) - \nabla^2 \vec{A},$$

and the fact that the operators  $\nabla \times \frac{\partial}{\partial t}$  and  $\frac{\partial}{\partial t} \nabla \times$  are equivalent as space and time coordinates are independent.

For an electromagnetic wave of high frequency  $\omega_0$ , the electric field vector takes the form

$$\vec{E} = \vec{E}(x, y, z, t) \exp(-i\omega_0 t) + c.c.,$$

where the amplitude  $\vec{E}(x, y, z, t)$  is assumed to vary on a time scale that is much larger than the light period  $2\pi/\omega_0$ . Enveloping Eq. (3.5) with respect to time reduces the order of the time derivative, and one obtains

$$2i \frac{\omega_0}{c^2} \epsilon \mu \frac{\partial \vec{E}}{\partial t} + \nabla^2 \vec{E} + \frac{\omega_0^2}{c^2} \epsilon \mu \vec{E} - \nabla(\nabla \cdot \vec{E}) = 0, \quad (3.6)$$

where  $\nabla^2 = \partial^2/\partial x^2 + \partial^2/\partial y^2 + \partial^2/\partial z^2$  is the Laplacian in a three-dimensional Cartesian geometry.

In this chapter, we develop a 1-field component wave equation (scalar case) model. This will later be generalized to the case of 2 and 3 electric field components. For the 1-field component case, we consider the scattering of laser light by biological mediums in two and three spatial dimensions. A 2-D wave equation can be obtained from Eq. (3.6) by assuming that the biological medium is inhomogeneous in the  $x - y$  plane and that the electromagnetic wave is  $s$  - polarized,



so that  $\vec{E} = E(x, y, t)\vec{e}_z$ , i.e., the electric field polarization vector is perpendicular to the plane of inhomogeneity of the biological medium. For this case, the last term on the left hand side of Eq. (3.6) is zero, and one obtains a scalar wave equation with a 2-D Laplacian for the electric field amplitude  $E(x, y, t)$ :

$$2i\frac{\omega_0}{c^2}\varepsilon\mu\frac{\partial E}{\partial t} + \nabla^2 E + \frac{\omega_0^2}{c^2}\varepsilon\mu E = 0. \quad (3.7)$$

The scalar field approximation can be also considered in three spatial dimensions. The form of the wave equation for the 3-D scalar field approximation is similar to that of Eq. (3.7), except that the Laplacian  $\nabla^2$  has three spatial components. For the case of three spatial dimensions, the last term on the left hand side of Eq. (3.6) may not be negligible. The validity of such an approximation will be tested by comparing simulation results with exact analytical solutions for scattering from homogeneous spherical dielectrics, especially for forward scattering (see figure 4.2).

For a biological medium, we assume  $\mu = 1$ , and that the dielectric constant can be represented as a sum of two terms:

$$\varepsilon = \varepsilon_0 + \Delta\varepsilon(x, y, z). \quad (3.8)$$

Here  $\varepsilon_0$  is the dielectric constant of inter-cellular fluid that is considered homogeneous, and  $(\varepsilon_0 + \Delta\varepsilon(x, y, z))$  is the dielectric constant of a cell that consists of cytoplasm, nucleus, and other internal structures. For the cells considered in this thesis, the perturbations  $\Delta\varepsilon$  are assumed small:  $|\Delta\varepsilon| < \varepsilon_0$ .

It is readily seen that the first term on the left hand side of Eq. (3.7) accounts for time variations of the electric field amplitude. In our studies, the biological medium is considered stationary. Non-stationarity can only play a role during the propagation of the electromagnetic wave front through the medium. Hence,  $\varepsilon$  can be replaced by  $\varepsilon_0$  in the time derivative term in Eq. (3.7), allowing us to

rewrite the scalar wave equation (3.7) as

$$2i\frac{\omega_0}{c^2}\varepsilon_0\frac{\partial E}{\partial t} + \nabla^2 E + \frac{\omega_0^2}{c^2}\varepsilon_0 E = -\frac{\omega_0^2}{c^2}f(t)\Delta\varepsilon E \quad (3.9)$$

The time function of  $f(t)$  in right-hand side of Eq. (3.9) models an adiabatic “turn on” of the perturbations (see fig.3.1). The normalizing time is in the unit of picoseconds (see details in the next section).

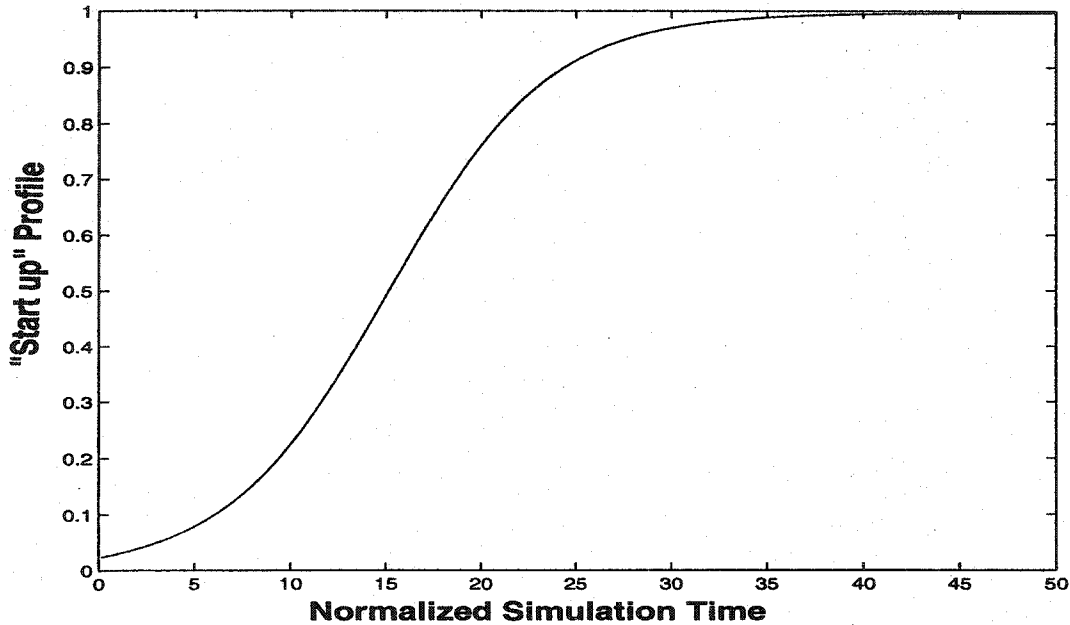


Figure 3.1: The profile of time function  $f(t)$  which is used to “turn on” the perturbations. Here the simulation time is normalized and a stable solution is generated in the time interval from 40 to 50ps.

The left hand side of Eq. (3.9) accounts for the field propagation in a homogeneous medium, and the interaction with inhomogeneous perturbations is described by the right-hand side. There are no restrictions in our model on the scale length of spatial variations in  $\Delta\varepsilon$ . However, inhomogeneities in the scattering medium on a scale length much smaller than laser wavelength cannot be properly resolved from the scattered light spectra. Therefore, we assume that

the characteristic scale length of the spatial inhomogeneity for the perturbation  $\Delta\epsilon$  is longer than the laser wavelength in the medium  $\lambda_m = c/(\omega_0\sqrt{\epsilon_0})$ . Inhomogeneities on a scale length smaller than the wavelength  $\lambda_m$  (for example, the interface between cell and inter-cellular fluid) are treated as sharp boundaries in our method. This approach is consistent with the fact that light scattering off an interface much narrower than the wavelength is similar to scattering off a sharp boundary.

## 3.2 The Spectral Method

The wave equation (3.9) is solved in a 3-D region:  $0 \leq x \leq L_x$ ,  $-L_y/2 \leq y \leq L_y/2$  and  $-L_z/2 \leq z \leq L_z/2$  (see Fig. 3.2) by using the spectral method [2]. The incident electromagnetic wave is assumed to propagate in the  $x$ -direction. In this spectral method, we expand the electric field amplitude  $E$  into a Fourier series in the transverse ( $y$  and  $z$ ) directions, obtaining

$$E = \sum_m \sum_{m'} E_{mm'}(x) \exp(imk_y y + im'k_z z), \quad (3.10)$$

where  $k_y = 2\pi/L_y$  and  $k_z = 2\pi/L_z$ . We now introduce the following dimensionless variables:

$$\begin{aligned} T &= \beta\omega_0 t / \epsilon_0 \\ X &= kx \\ Y &= ky \\ Z &= kz, \end{aligned} \quad (3.11)$$

where  $k = 2\pi N/\lambda_0$ , with  $\lambda_0 = c/\omega_0$  being the laser wavelength in vacuum and  $N = \sqrt{\epsilon_0}$  is the medium refractive index in the simulation region, and  $\beta$  being a dimensionless parameter which is used to renormalize the time  $T$  to some

convenient unit (picoseconds, for example). This allows us to recast Eq. (3.9) in the following form:

$$\left(2i\beta\frac{\partial}{\partial T} + \frac{\partial^2}{\partial X^2} + K_{Xmm'}^2\right) E_{mm'} = NL(E_{mm'}, T), \quad (3.12)$$

where,

$$\begin{aligned} NL(E_{mm'}, T) &= -\Delta\epsilon E_{mm'} \\ K_{Xmm'}^2 &= \epsilon_0 - (mk_y/k)^2 - (m'k_z/k)^2. \end{aligned} \quad (3.13)$$

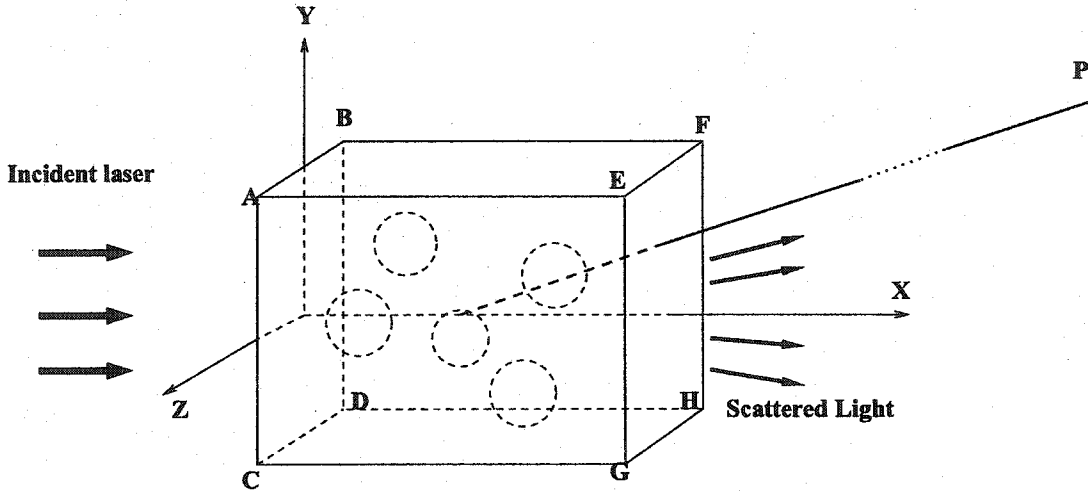


Figure 3.2: The geometry of the simulation

The electric field amplitude  $E$  is expanded into Chebyshev polynomials in the longitudinal ( $x$ ) direction. The length of the simulation region in the direction of light propagation  $[0, L_x]$  is mapped into the interval  $[-1, 1]$  and the gridpoints are defined as:  $X_j = -\cos((j-1)\pi/N_x)$ , where  $j = 1, 2, \dots, N_x + 1$  and  $N_x$  is the total number of points in the  $x$ -direction.

### 3.3 Iteration in Time

We use the implicit midpoint rule [5] for the time iteration of Eq. (3.12). The implicit midpoint method solves a differential equation of the following form

$$\dot{u} = p(u)u,$$

where  $p(u)$  is a given function of the quantity  $u$ . For a step in time  $u^n \rightarrow u^{n+1}$ ,  $t_n \rightarrow t_{n+1} = t_n + \tau$ , where  $\tau$  is the step size and  $u^n$  is the quantity  $u$  at  $t = t_n$ , the implicit midpoint rule reads

$$u^{n+1} = u^n + \tau p(\tilde{u})\tilde{u}, \quad (3.14)$$

where  $\tilde{u} = (u^{n+1} + u^n)/2$  is the midpoint value of  $u$ . Solutions to Eq. (3.14) have the conservation property  $|u^n| = |u^{n+1}|$ , and the solution  $u^n$  is bounded as  $n \rightarrow \infty$  [6].

Now, Eq. (3.12) can be rewritten as:

$$\frac{\partial E_{mm'}}{\partial T} = \frac{i}{2\beta} \left( \frac{\partial^2}{\partial X^2} + K_{Xmm'}^2 - \frac{NL(E_{mm'}, T)}{E_{mm'}} \right) E_{mm'}. \quad (3.15)$$

In order to advance Eq. (3.12) in time, the forward Euler scheme has been used to get the midpoint value  $\tilde{E}_{mm'}$ . The forward Euler scheme takes the form

$$E_{mm'}^{n+1} = E_{mm'}^n + \tau \left. \frac{dE_{mm'}}{dt} \right|_n. \quad (3.16)$$

Combining Eqs. (3.15) and (3.16), the middle point value takes the form

$$\tilde{E}_{mm'} = E_{mm'}^n + \frac{i\tau}{4\beta} \left[ \frac{\partial^2 E_{mm'}^n}{\partial X^2} + K_{Xmm'}^2 E_{mm'}^n - NL(E_{mm'}^n, T^n) \right]. \quad (3.17)$$

From the implicit midpoint rule (3.14), one obtains:

$$E_{mm'}^{n+1} = E_{mm'}^n + \frac{i\tau}{2\beta} \left[ \frac{\partial^2}{\partial X^2} + K_{Xmm'}^2 - \frac{NL(\tilde{E}_{mm'}, T^n)}{\tilde{E}_{mm'}} \right] \tilde{E}_{mm'}. \quad (3.18)$$

Substituting Eq. (3.17) into Eq. (3.18) and assuming  $NL(\tilde{E}_{mm'}, T^n) = NL(E_{mm'}^n, T^n)$ , we have

$$E_{mm'}^{n+1} = \tilde{E}_{mm'} + \frac{i\tau}{4\beta} \left[ \frac{\partial^2}{\partial X^2} + K_{Xmm'}^2 \right] E_{mm'}^{n+1} - \frac{i\tau}{4\beta} NL(\tilde{E}_{mm'}, T^n), \quad (3.19)$$

which can be rewritten as follows

$$\left( \frac{\partial^2}{\partial X^2} - \lambda \right) E_{mm'}^{n+1} = \frac{i4\beta}{\tau} \tilde{E}_{mm'} + NL(\tilde{E}_{mm'}, T^n), \quad (3.20)$$

where  $\lambda = -K_{Xmm'}^2 - i4\beta/\tau$ . The length of the simulation region in the direction of light propagation is mapped into interval  $[-1, 1]$  and, therefore, Eq. (3.20) is a Dirichlet problem for a second-order elliptic operator in the interval  $[-1, 1]$ , which we may solve using the Tau method [2].

### 3.4 Boundary Conditions

Due to the properties of the Fourier transform, the imposed boundary conditions are periodic in the transverse ( $y$  and  $z$ ) directions. The boundary conditions in  $x$ -direction correspond to transparent boundaries at  $X_l = 0$  and  $X_r = k_0 L_x$  for both the incident and the scattered waves (see [3] and [4]):

$$\begin{aligned} \left. \frac{\partial E_{mm'}}{\partial X} \right|_{X_l} &= iK_{Xmm'} \left( 2E_{mm'}^{(0)} - E_{mm'}(X_l, T) + \right. \\ &\quad \left. \frac{i\beta}{K_{Xmm'}^2} \frac{\partial}{\partial T} \left[ E_{mm'}^{(0)}(T) - E_{mm'}(X_l, T) \right] \right) \\ \left. \frac{\partial E_{mm'}}{\partial X} \right|_{X_r} &= iK_{Xmm'} \left( 1 + \frac{i\beta}{K_{Xmm'}^2} \frac{\partial}{\partial T} \right) E_{mm'}(X_r, T), \end{aligned} \quad (3.21)$$

where  $E_{mm'}^{(0)}(T)$  is the Fourier component of the incident electric field amplitude.

### 3.5 The Shape of Incident Beam

Three kinds of incident beam shapes are used in our simulations. The simplest case is that of an incident plane wave. However, we also use two more complicated beam shapes—the flat-top laser beam (in dimensional units)

$$E_0(x=0, y, z, t) = \frac{1}{4}E_0(t)\left(\tanh\frac{y+a}{\delta} - \tanh\frac{y-a}{\delta}\right) \times \left(\tanh\frac{z+a}{\delta} - \tanh\frac{z-a}{\delta}\right), \quad (3.22)$$

where  $a$  stands for the half-width of the beam at the plane of incidence and  $\delta$  characterizes the smoothness of the beam edges, as well as the Gaussian beam [7]

$$E_0(x=0, y, z, t) = E_0(t)\frac{\sigma}{W(x)}\exp\left[-\frac{y^2+z^2}{2W(x)^2}\right] \times \exp\left[-jkx - jk\frac{y^2+z^2}{2R(x)^2} + j\zeta(x)\right], \quad (3.23)$$

where  $W(x)$  and  $R(x)$  are the beam radius and the wavefront radius, respectively, taking the following forms:

$$W(x) = \sigma\left[1 + \left(\frac{x}{L_R}\right)^2\right]^{1/2} \quad (3.24)$$

$$R(x) = x\left[1 + \left(\frac{L_R}{x}\right)^2\right] \quad (3.25)$$

$$\zeta(x) = \arctan\frac{x}{L_R} \quad (3.26)$$

where  $\sigma$  is the minimum radius of the beam at the best focus position and  $L_R$  is the Rayleigh Range, which is the distance from the best focus position to where the beam radius increases by a factor of 2. The minimum radius of the beam is related to the Rayleigh Range by

$$\sigma = \left(\frac{\lambda L_R}{2\pi}\right)^{1/2}, \quad (3.27)$$

where  $\lambda$  is the wavelength. The number  $f$  is defined to characterize the minimum radius of the beam  $\sigma = f\lambda$  at the best focus position and the  $f$  number is also

related to the Rayleigh length  $L_R = 2\pi f^2 \lambda$ . The Gaussian profile given in (3.23) is a reasonable realization of an actual incident laser beam as it might be found in an experimental setup, while the plane wave is a ideal profile for testing the validity of the code, as it allows for comparison with analytical solutions, i.e., Mie theory.

### 3.6 Far-field Calculation

An appropriate presentation of numerical data is very important for the comparison with experimental results and theoretical models. Typical experimental measurements usually only show the characteristics of the laser light well outside the interaction region. Therefore, the laser field profile far from the scattering objects ( so-called far-field) should be calculated from the field distribution in the interaction region (so-called near-field) which we have obtained through our simulations.

The asymptotic expression for the electric field of the scattered light at a far-field point  $p$  (see Fig. 3.2) is given by [8]:

$$E(p, t) = \frac{1}{2i} \oint_s dS \cdot \left[ E_s(x, y, z, t) \nabla_n \left( \frac{1}{2\pi k \rho(x, y, z)} \exp(ik\rho(x, y, z) - i\pi/4) \right) - \frac{1}{2\pi k \rho(x, y, z)} \exp(ik\rho(x, y, z) - i\pi/4) \nabla_n E_s(x, y, z, t) \right], \quad (3.28)$$

where  $E_s$  is the electric field at the emitting surface,  $E(p, t)$  is the electric field at a far-field point  $p$ ,  $\nabla_n$  denotes the derivative along the outward drawn normal to the emitting surface, and  $\vec{\rho}$  is the vector from the point at the emitting surface with coordinates  $(x, y, z)$  to the far-field point with coordinates  $(x_0, y_0, z_0)$ . In order to evaluate the above integral, we use a Cartesian geometry and let

$$u = (1/2\pi k \rho(x, y, z)) \exp(ik\rho(x, y, z) - i\pi/4).$$



Then the integral (3.28) takes the following form:

$$E(p, t) = \frac{1}{2i} \oint_s dS \cdot (E \nabla_n u - u \nabla_n E). \quad (3.29)$$

From Fig. 3.2 one can see that the planes  $ABCD$  and  $EFGH$  coincide with the input ( $x = 0$ ) and output ( $x = L_x$ ) boundaries. For forward scattering calculations, we consider only the contributions due to plane  $EFGH$ , while for backward scattering calculations, we consider only the contributions due to plane  $ABCD$ . Hence, the integral Eq. (3.29) reduces to

$$E(p, t) = \frac{1}{2i} \int \int dydz \left( E \frac{\partial u}{\partial x} - u \frac{\partial E}{\partial x} \right). \quad (3.30)$$

The above result can be expressed in a somewhat more informative form if we rewrite  $|\vec{\rho}|$  in terms of spherical coordinates  $(\theta, \phi)$ . Using the facts

$$\begin{aligned} \partial \rho / \partial x &= -x/\rho = -\cos \theta \\ \partial u / \partial x &= (\partial u / \partial \rho)(\partial \rho / \partial x) = -\cos \theta (\partial u / \partial \rho) \\ \rho &\simeq \rho_0 - x \cos \theta - y \sin \theta \cos \phi - z \sin \theta \sin \phi \\ \lim_{\rho \rightarrow \infty} u &= \frac{1}{2\pi k \rho_0} \exp(ik\rho_0 - ikx \cos \theta -iky \sin \theta \cos \phi \\ &\quad -ikz \sin \theta \sin \phi - i\pi/4) \\ \lim_{\rho \rightarrow \infty} \frac{\partial u}{\partial \rho} &= \frac{ik}{2\pi k \rho_0} \exp(ik\rho_0 - ikx \cos \theta -iky \sin \theta \cos \phi \\ &\quad -ikz \sin \theta \sin \phi - i\pi/4), \end{aligned} \quad (3.31)$$

we have

$$\begin{aligned} E(p, t) &= \frac{1}{2i} \frac{1}{2\pi k \rho_0} \int \int dydz \left[ -ikE \cos \theta - \frac{\partial E}{\partial x} \right] \\ &\quad \times \exp(-ikx \cos \theta -iky \sin \theta \cos \phi -ikz \sin \theta \sin \phi). \end{aligned} \quad (3.32)$$

By introducing  $k_x = k \cos \theta$ ,  $k_y = k \sin \theta \cos \phi$ ,  $k_z = k \sin \theta \sin \phi$ , and taking into account that, in the case of forward scattering,  $E \sim \exp(ik_x x)$ , one obtains from Eq. (3.32) that

$$E(p, t) = \frac{\exp(ik\rho + i\pi/4)}{4\pi k \rho_0} [-2ik_x \exp(-ik_x x)] E(L_x, k_y, k_z). \quad (3.33)$$

Similarly, in the case of backward scattering, we have

$$E(p, t) = \frac{\exp(ik\rho + i\pi/4)}{4\pi k\rho_0} [2ik_x \exp(-ik_x x)] E(0, k_y, k_z). \quad (3.34)$$

Equations (3.33) and (3.34) for  $E(p, t)$  have been used in our numerical simulations to calculate the scattered light intensity at the far-field points. The emitted power at a far-field point is given by

$$Q = \frac{c}{8\pi} \rho_0^2 |E(p, t)|^2 = \frac{c}{128\pi^3 k^2} |ik_x E(L_x, k_y, k_z)|^2 \quad (3.35)$$

### 3.7 Conclusions

The model presented in this chapter allows us to describe the interaction of a laser with biological objects on spatial scales ranging from single cells to larger samples. In this model, only a scalar wave equation is solved, which can be accomplished more efficiently than the calculations required for other numerical solutions, such as FDTD and Monte Carlo techniques. The nonparaxial spectral method is employed to solve the scalar wave equation and both forward and backward scattering are considered in the model. The small-angle, large-angle (up to  $25^\circ$ ), and backward scattering signals can be obtained. From the scattered signals, it is possible to differentiate between cells on the basis of their size and composition. In the next chapter, the implementation and validation of the code will be presented.

## Bibliography

- [1] J. D. Jackson, *Classical Electrodynamics*. New York: Wiley, 1974
- [2] C. Canuto, M. Y. Hussaini, A. Quarteroni, T. A. Zang, *Spectral Methods in Fluid Dynamics* (Springer-Verlag, Berlin Heidelberg 1988).
- [3] M. R. Amin, C. E. Capjack, P. Frycz, W. Rozmus, and V. T. Tikhonchuk, *Phys. Fluids B* **5**, 3748 (1993).
- [4] M. R. Amin, C. E. Capjack, P. Frycz, W. Rozmus, and V. T. Tikhonchuk, *Phys. Rev. Lett.*, **71**, 81 (1993).
- [5] J. M. Sanz-Serna and J. G. Verwer, *IMA Journal of Numerical Analysis* **6**, 25-42 (1986).
- [6] J. M. Sanz-Serna and V. S. Manoranjan, *J. Comp. Phys.* **52**, 273-289 (1983).
- [7] B. E. A. Saleh and M. C. Teich, *Fundamentals of Photonics* (New York: Wiley, 1991).
- [8] M. Born and E. Wolf, *Principles of Optics* (Pergamon, Oxford, 1970).

# Chapter 4

## Code Development and Validation

### 4.1 Introduction

In the previous chapter, we presented the theoretical model upon which our simulations are based. We subsequently derived the approximate scalar 3-D wave equation from Maxwell's equations, explained in detail the numerical algorithm which we use to solve this equation, and also addressed the far-field electric field calculations.

A code previously developed for studying laser-plasma interaction physics [1–4] was evolved to address the scattering of light by cells. The development and validation of this new code is now addressed.

In the code development section, I briefly describe the process of code development and address some of the difficulties which arose during this process. In the code validation section, I describe the 3 main areas where the code was tested. These include 2-D simulation results which are compared with the predictions of linear perturbation theory; the 3-D simulation results, which are benchmarked

against the Mie theory predictions for scattering from a homogeneous sphere; and backward scattering calculations, which must be addressed as they require extensive computational accuracy and stability.

## 4.2 Code Development

As described in previous chapter, the wave equation (3.9) is solved numerically through use of the spectral method. In the past, the spectral method has been used to describe light scattering from inhomogeneous, time dependent dielectrics, and applied to a number of problems in laser-plasma interaction physics [1–4]. The 2-D laser-plasma interaction code solves a coupled system of equations for the non-paraxial electromagnetic and the ion-acoustic waves. In order to apply this code to laser-tissue interactions, several modifications were required, such as, physically separating the two coupled equations in the iterations, benchmarking the simulation results after separation, deleting everything related to the ion-acoustic wave equation, and implementing a subroutine to model cell as described by equation (3.8).

After successfully testing this new version of the 2-D code (see next section), a three dimensional version of the code was developed. One more dimension to the modified 2-D code was added and subroutines for the far-field electric field calculations were written. The 3-D code has been successfully run on “Aurora and Borealis”, the parallel supercomputers on the University of Alberta campus. “Aurora”, a SGI Origin 2000, is configured with 46 processors and “Borealis” is a SGI Origin 2400 with 64 processors. For a typical model, with a simulation region (Fig. 3.2) size of  $40 \times 80 \times 80$  wavelengths  $\lambda_0$  ( $40\lambda_0$  is the length in the direction of wave propagation and  $80\lambda_0$  is the length of two transverse directions), the code will usually take less than 24 hours to run on “Aurora” (utilizing 10 processors).

## 4.3 Code Validation

### 4.3.1 Linear Perturbation Theory

In this subsection, an analytic stationary solution to Eq. (3.9) is obtained via the linear perturbation method. In the stationary regime, the time derivative term in Eq. (3.9) can be neglected. Consider the scalar wave equation (3.9) in two spatial dimensions. By assuming small-angle scattering, the field amplitude  $E$  can be written as  $E = E_a(x, y) \exp(ik_m x)$ , where  $k_m \equiv 2\pi/\lambda_m = (\omega_0/c)\sqrt{\varepsilon_0}$  is the laser wavevector in the inter-cellular medium. The characteristic inhomogeneity scale length of the field amplitude  $E_a(x, y)$  in the direction of light propagation ( $x$ ) is assumed to be much larger than the laser wavelength in the inter-cellular medium  $\lambda_m \ll |\partial \ln(E_a)/\partial x|^{-1}$ . This is the condition that is required for the validity of the paraxial approximation. Expanding  $E_a = E_0 + \delta E$ , where  $E_0$  is the incident light amplitude and  $\delta E$  is the scattered light amplitude ( $|\delta E| \ll |E_0|$ ), Eq. (3.9) to first order in  $\delta E$  and  $\Delta\varepsilon$  takes form

$$2ik_m \frac{\partial \delta E}{\partial x} + \frac{\partial^2 \delta E}{\partial y^2} + \frac{\omega_0^2}{c^2} \Delta\varepsilon E_0 = 0. \quad (4.1)$$

After performing a Fourier transformation in the transverse ( $y$ ) direction, we obtain the following equation for the Fourier component of the electric field  $\delta E(x, k_y)$ :

$$2ik_m \frac{d\delta E(x, k_y)}{dx} - k_y^2 \delta E(x, k_y) + \frac{\omega_0^2}{c^2} \Delta\varepsilon(x, k_y) E_0 = 0, \quad (4.2)$$

where  $\Delta\varepsilon(x, k_y)$  is the Fourier component of the dielectric constant perturbation  $\Delta\varepsilon(x, y)$ . The solution to Eq. (4.2) takes the form

$$\delta E(x, k_y) = \frac{i\omega_0^2 E_0}{2k_m c^2} \int_0^x dx' \Delta\varepsilon(x', k_y) \Delta\varepsilon(x', k_y) \exp\left(-\frac{ik_y^2}{2k_m}(x - x')\right). \quad (4.3)$$

The constant of integration in (4.3) is chosen so that the field perturbation  $\delta E$  is zero at the boundary  $x = 0$ .

For simplicity, consider a square perturbation of the dielectric constant  $\Delta\varepsilon(x, y)$  equal to  $\Delta\varepsilon_0$  in the region  $-R_0 \leq x - x_0 \leq R_0$  and  $-R_0 \leq y \leq R_0$ , and zero elsewhere. By using the assumption that the incident light has a very small divergence angle ( $E_0(L_x, k_y) \approx 0$  for  $k_y \neq 0$ ), we may combine (4.3) and (3.35) to obtain the transmitted power per unit angle

$$Q = \frac{8E_0^2}{\pi^3 L_y^2} \left( \frac{\Delta\varepsilon_0}{\varepsilon_0} \right)^2 \frac{1 - k_*^2}{k_*^6} \sin^2 \left( \frac{2\pi R_0}{\lambda_m} k_* \right) \sin^2 \left( \frac{\pi R_0}{\lambda_m} k_*^2 \right), \quad (4.4)$$

where  $k_* = k_y/k_0$ .

Similarly, placing a square nucleus measuring  $2R_n$  by  $2R_n$  and dielectric constant perturbation  $\Delta\varepsilon_n$  in the center of a cell with dimensions  $2R_0$  by  $2R_0$  and dielectric constant  $\Delta\varepsilon_0$ , the transmitted power per unit angle is

$$Q = \frac{8E_0^2}{\pi^3 L_y^2} \left( \frac{\Delta\varepsilon_0}{\varepsilon_0} \right)^2 \frac{1 - k_*^2}{k_*^6} \left[ \sin^2 \left( \frac{2\pi R_0}{\lambda_m} k_* \right) \sin^2 \left( \frac{\pi R_0}{\lambda_0} k_*^2 \right) + 2 \left( \frac{\Delta\varepsilon_n}{\Delta\varepsilon_0} - 1 \right) \sin \left( \frac{2\pi R_0}{\lambda_m} k_* \right) \sin \left( \frac{\pi R_0}{\lambda_m} k_*^2 \right) \sin \left( \frac{2\pi R_n}{\lambda_m} k_* \right) \sin \left( \frac{\pi R_n}{\lambda_m} k_*^2 \right) + \left( \frac{\Delta\varepsilon_n}{\Delta\varepsilon_0} - 1 \right)^2 \sin^2 \left( \frac{2\pi R_n}{\lambda_m} k_* \right) \sin^2 \left( \frac{\pi R_n}{\lambda_m} k_*^2 \right) \right]. \quad (4.5)$$

As  $k_* \rightarrow 0$  formula (4.5) takes the form

$$Q = \frac{32\pi E_0^2}{L_y^2} \left( \frac{\Delta\varepsilon_0}{\varepsilon_0} \right)^2 \left( \frac{R_0}{\lambda_m} \right)^4 \left[ 1 + 2 \left( \frac{\Delta\varepsilon_n}{\Delta\varepsilon_0} - 1 \right) \left( \frac{R_n}{R_0} \right)^2 + \left( \frac{\Delta\varepsilon_n}{\Delta\varepsilon_0} - 1 \right)^2 \left( \frac{R_n}{R_0} \right)^4 \right]. \quad (4.6)$$

The scattering from these square perturbations can be used to test the numerics of our spectral method. A comparison between our numerical results and theoretical predictions from Eqs. (4.4), (4.5) is shown in Fig. 4.1. In these simulations, the dielectric constant of the medium is  $\varepsilon_0 = 1.8225$ , while the dielectric constant perturbations for the cytoplasm and the nucleus are  $\Delta\varepsilon_0 = 0.0544$  and  $\Delta\varepsilon_n = 0.1096$  respectively. The accuracy of our numerical method in this case is clearly demonstrated in Fig. 4.1, where the simulation results agree nicely with theoretical calculations.

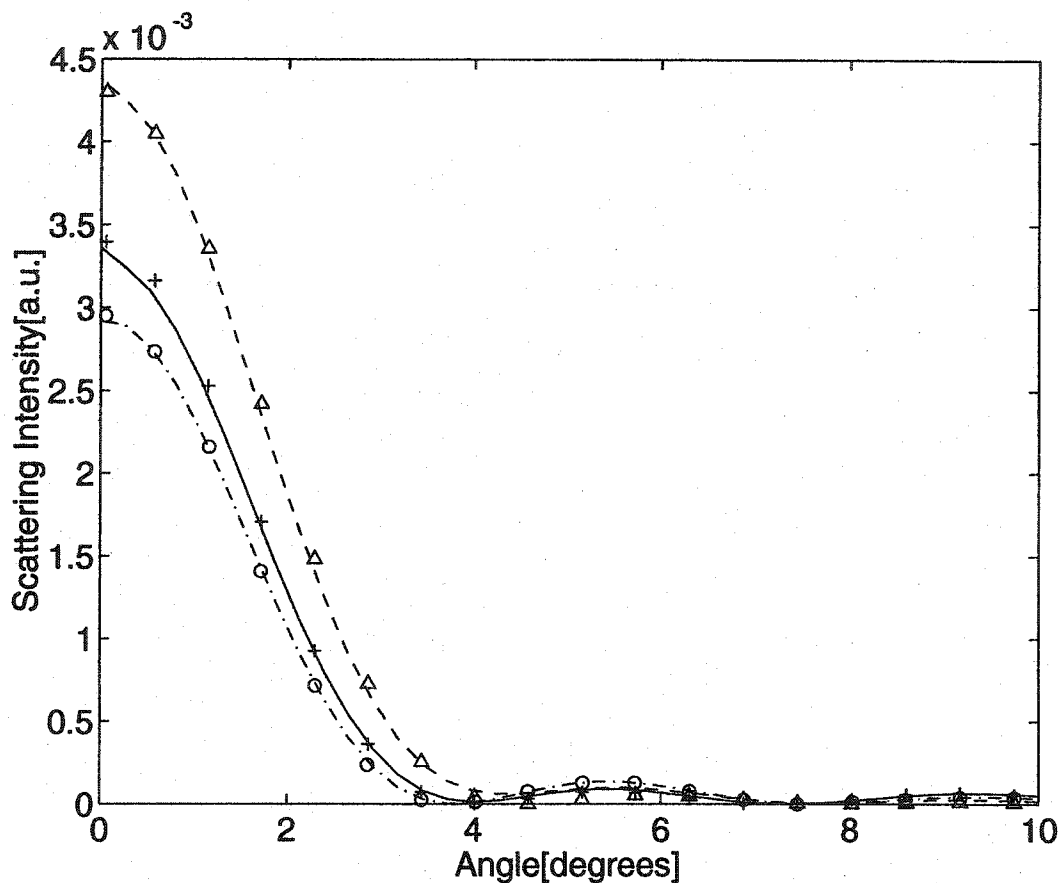


Figure 4.1: A comparison of the scattering intensity obtained from both numerical simulations and analytic solutions (4.6) for three types of square cells: for a cell without a nucleus—the dash-dotted line (simulations) and “*circ*” (analytical); for a cell with a normal nucleus—the solid line (simulations) and “+” (analytical); and for a cell with a large nucleus—the dashed line (simulations) and “ $\Delta$ ” (analytical). The width of the cell is  $D_0 = 11\mu m$ , the width of the normal nucleus is  $D_n = 3\mu m$ , and the width of the large nucleus is  $D_n = 6\mu m$ . The dielectric constant perturbation for the cell is  $\Delta\epsilon_0 = 0.0544$ , while for the nucleus  $\Delta\epsilon_n = 0.1096$ .



### 4.3.2 Scattering from a Homogeneous Sphere

The diffraction of a plane monochromatic wave by a homogeneous sphere with a zero thickness interface can be calculated within the framework of Mie theory [7, 8]. Mie theory exactly solves Maxwell's equations in 3-D for all components of the electromagnetic field both inside and outside of the sphere, along with the boundary conditions on the surface. In Mie theory, the electromagnetic fields are expressed in term of infinite series expansions. These expansions can be significantly simplified when the distance  $r$  from the scattering sphere is much larger than the laser wavelength  $\lambda_m$  in the medium surrounding the scattering sphere. When the incident light is linearly polarized, the scattered light intensity  $|S|^2$  can be determined by [8]

$$S = \sum_n \frac{2n+1}{n(n+1)} [a_n \tau_n + b_n \pi_n] \quad (4.7)$$

where  $\pi_n = -(1/\sin\theta)dP_n/d\theta$ ,  $\tau_n = -d^2P_n/d\theta^2$ , and  $P_n$  are the Legendre polynomials of order  $n$ . The coefficients  $a_n$  and  $b_n$  are given by

$$\begin{aligned} a_n &= \frac{m\psi_n(mx)\psi'_n(x) - \psi_n(x)\psi'_n(mx)}{m\psi_n(mx)\xi'_n(x) - \xi_n(x)\psi'_n(mx)} \\ b_n &= \frac{\psi_n(mx)\psi'_n(x) - m\psi_n(x)\psi'_n(mx)}{\psi_n(mx)\xi'_n(x) - m\xi_n(x)\psi'_n(mx)}, \end{aligned} \quad (4.8)$$

where  $\psi_n$  and  $\xi_n$  are the Ricatti-Bessel functions,  $x = k_m a$ ,  $m = k_s/k_m$ ,  $a$  is the radius of the scattering sphere, and  $k_m$  and  $k_s$  are the laser wavevectors outside and inside the scattering sphere, respectively.

Figure 4.2 and Figure 4.3 compare 3D simulation results and Mie theory predictions for the scattering of a plane wave by a homogeneous sphere in different cases. The agreement is very good for scattering angles up to 30 degrees. This good agreement between simulations and theory is achieved in spite of the fact that the numerical model solves the wave equation in the scalar approximation, whereas Mie theory solves the full Maxwell's equations (for all 6 components of

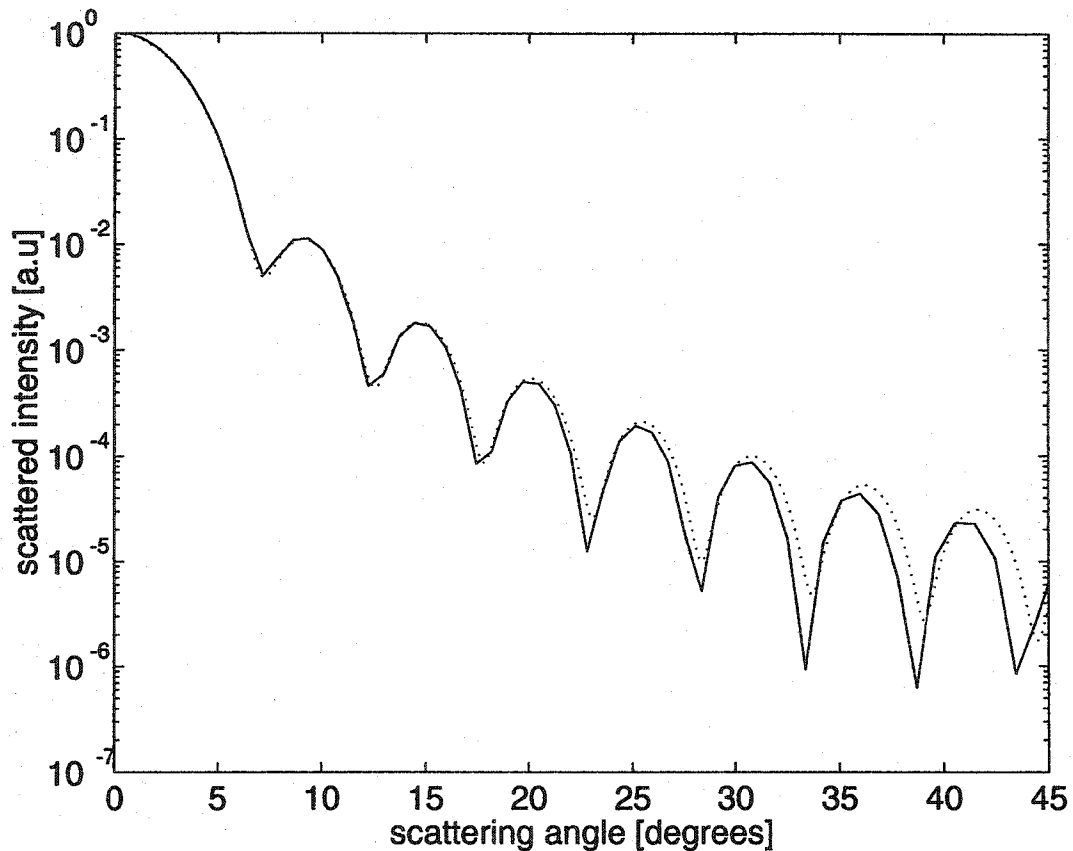


Figure 4.2: A comparison of the intensity of scattered light from a homogeneous sphere in three spatial dimensions obtained from simulations (solid line) and from Mie theory (dotted line). The diameter of the sphere is  $D_0 = 11\mu m$ . The dielectric constant outside the sphere is  $\epsilon_0 = 1$  and inside the sphere  $\epsilon = 1.0609$ . In the simulation result, the transmitted component (at  $0^\circ$ ) has been removed by setting the intensity at 0 degrees equal to its neighbour point.

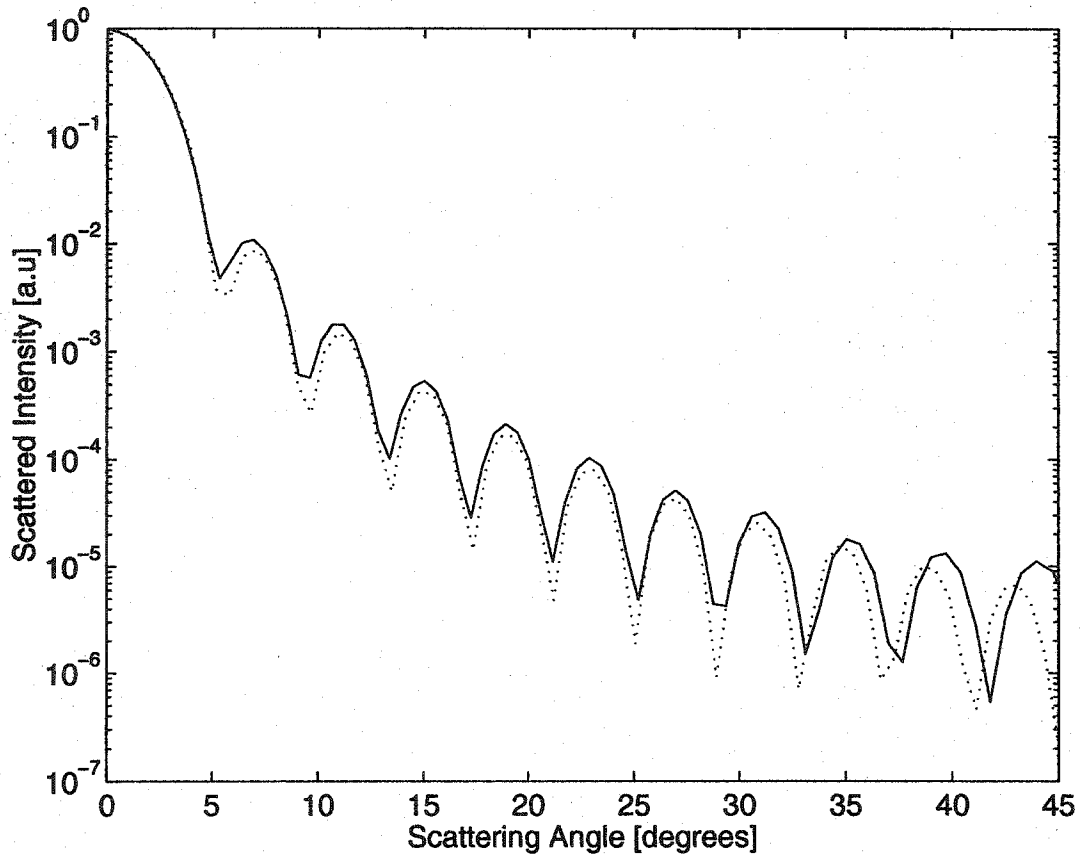


Figure 4.3: An another comparison of the intensity of scattered light from a homogeneous sphere in three spatial dimensions obtained from simulations (solid line) and from Mie theory (dotted line). The diameter of the sphere is  $D_0 = 11\mu m$ . The dielectric constant outside the sphere is  $\epsilon_0 = 1.8225$  and inside the sphere  $\epsilon = 1.8769$ . In the simulation result, the transmitted component (at  $0^\circ$ ) has been removed by setting the intensity at 0 degrees equal to its neighbour point.

the electromagnetic field). We may conclude that the scalar wave equation is an effective approximation to the full Maxwell equations for moderate scattering angles that are of practical importance for applications such as cytometry. The scalar wave approximation is valid because in the case of small-angle scattering, the longitudinal component of the electric field  $\vec{E}$  is small and  $div\vec{E}$  is small, so the last term on the left hand side of the full wave equation (3.6) can be neglected. For larger scattering angles, the scalar wave approximation breaks down, since the term with  $div\vec{E}$  becomes comparable to the second and third terms on the left hand side of Eq. (3.6).

### 4.3.3 Backward Scattering

Mie theory predicts (see figure 2.4) a 5 to 6 order of magnitude difference between the forward and backward scattering intensities. It is very difficult for a simulation code to give correct results over a range from 1 to  $10^{-6}$ . So verification of the backward scattering calculations must be addressed.

We first examined the reflection and refraction of electromagnetic waves at a plane interface between two different dielectrics. In the propagation direction, one half the simulation box was filled with a medium with a refractive index of 1.00 while the other half was filled with another medium with a refractive index of 1.03. The incident laser light was assumed normal to the plane interface. The simulation results show that the ratio of intensities of the reflected and incident light is  $2.1 \times 10^{-4}$ .

Based on the Fresnel's prediction [5], we have that if the electric field is perpendicular to the plane of incidence, the ratio of amplitudes of the reflected wave and incident wave takes form

$$\frac{E_0''}{E_0} = \frac{n \cos \theta - \frac{\mu}{\mu'} \sqrt{n'^2 - n^2 \sin^2 \theta}}{n \cos \theta + \frac{\mu}{\mu'} \sqrt{n'^2 - n^2 \sin^2 \theta}}, \quad (4.9)$$

where  $\theta$  is the incident angle,  $n$  and  $n'$  are the refractive indices of two different media, and  $\mu, \mu'$  are the permeabilities. On the other hand, if the electric field is parallel to the plane of incidence, the ratio of amplitudes of the reflected and incident fields is given by

$$\frac{E_0^r}{E_0} = \frac{\frac{\mu}{\mu'} n'^2 \cos \theta - n \sqrt{n'^2 - n^2 \sin^2 \theta}}{\frac{\mu}{\mu'} n'^2 \cos \theta + n \sqrt{n'^2 - n^2 \sin^2 \theta}}. \quad (4.10)$$

For normal incidence ( $\theta = 0$ ), Eqs. (4.9) and (4.10) reduce to

$$\frac{E_0^r}{E_0} = \frac{n' - n}{n' + n} \quad (4.11)$$

where  $\mu' = \mu$  is assumed. Using Eq. (4.11) and defining  $n' = 1.03$ ,  $n = 1.00$ , the ratio of intensities of the reflected and incident light is  $2.18 \times 10^{-4}$ . Therefore, our simulation result closely agrees with Fresnel's prediction.

Secondly, in order to avoid the aliasing effect [6] in the discrete Fourier transform, we have smoothly cut off modes with large  $k$  vectors in the transverse directions. This is done by multiplying the modes of  $E_y$  and  $E_z$  respectively by the profile function shown in Fig. (4.5). Figure 4.4 shows the backward scattering signal on the boundary. Figure 4.4 (a) corresponds to the case when a cutoff is not imposed on large  $\vec{K}$  values while figure 4.4 (b) represents the case where a cutoff on large  $\vec{K}$  values is used. Without a cutoff, the signal due to the aliased Fourier transform in the transverse directions are larger than the backward scattering signal which is very small for scattering from a cell. Therefore, an incorrect backward scattering profile is obtained in the far-field. With a cutoff, the backward scattering signal on the left boundary is correct (see Fig. 4.4 (b)), so that the backward scattering intensity in far-field is also correct. Therefore, in order to have a correct backward scattering signal distribution, modes with large  $\vec{K}$  values in transverse direction have to be smoothly cut-off. The prescription we have used is shown in Fig. 4.5. Figure 4.5 (a) and (b) show two

different smooth cutoff profiles imposed on large  $k$  modes in transverse directions. Fig. 4.6 (a) shows the scattering intensity in far-field corresponding to the smoothly cutoff profile shown in Fig. 4.5 (a) and Fig. 4.6 (b) is the scattering intensity in far-field corresponding to the smoothly cutoff profile shown in Fig. 4.5 (b). From Fig. 4.6 (a) and (b), the elimination of large  $\vec{K}$  modes gets rid of the signal produced by the aliased Fourier transform and leads to a correct backward scattering intensity in the far-field. By comparing Fig. 4.6 (a) with Fig. 4.6 (b), we can see that the difference in scattered intensity distribution is in the scattering angle beyond  $45^\circ$  in both forward and backward directions. Therefore, the profile of Fig. 4.5 (a) is chosen in our simulations. In transverse directions, we set the grid of 3 points per wavelength. This grid is not as fine as that in propagation direction (see below discussion) to resolve the interface profile between surrounding medium and cell. It may lead to some numerical inaccuracy at large scattering angle. This is the another reason why we choose the smooth cutoff profile described in Fig. 4.5 (a).

According to Mie scattering theory [8, 9], the backscattered (scattering angle  $\theta = \pi$ ) phase function can be expressed as

$$p(x, \pi) = \frac{1}{\pi x^2 Q_{sca}} |S_1(\pi)|^2, \quad (4.12)$$

where  $Q_{sca}$  is the scattering efficiency and  $x = 2\pi Na/\lambda_0$  is the size parameter defined in chapter 2; the definition of  $S_1(\pi)$  is given by Eq. (2.90). We have plotted  $p(x, \pi)$  (solid line with symbol '\*') and its corresponding backscattered intensity (solid line with symbol 'o') in Fig. 4.7 over a small range of size parameters common in spherical cell scattering. Figure 4.7 shows that the backscattered intensity is very sensitive to the size parameters (cell size). The reason of this sensitivity may be due to mismatch between the cell diameter and the incident laser wavelength. Therefore, the mechanism involved in the backscattering is rather complex.

In Mie theory, the interface between the cell and the surrounding medium is treated as a step-function. Unfortunately, when we attempt to model this setup numerically, stability requirements force us to describe the interface as an extended object—we treat the cell boundary as if it was a smooth transition from the index of refraction of the surrounding medium to that of the cell interior. We are allowed some freedom, however, in choosing how sharp/smooth this interface profile is. Our choice of interface profile will impact our measurement of effective cell radius and cell size parameter  $x$ — a broader interface region will tend to give a smaller size parameter than that which results when a very sharp interface profile is used. Therefore, we should examine the effect of our choice of interface profile on our simulation results. Figure 4.8 (a) shows a relatively smooth profile for the interface between cytoplasm and surrounding medium. Figure 4.8 (b) gives the scattering intensity distribution corresponding to this smooth profile. The magnitude of backward scattering is  $10^{-5}$  smaller than that predicted by Mie theory (dotted line in Figure 4.8 (b)). Figure 4.9 (a) shows a much sharper profile for the interface between the cytoplasm and the surrounding medium. Only 4 points are used to resolve the interface which leads to resolution limit of 3 points per wavelength (see Chapter 3). Figure 4.9 (b) gives the scattering intensity in far-field corresponding to the sharp profile of the interface. The backward scattering intensity is comparable with that predicted by Mie theory (see Fig. 4.9 (b)). Moreover, we consider the high resolution case by doubling the points in the propagation direction (12 points per wavelength in propagation direction). Figure 4.10 (a) shows the same profile as shown in Fig. 4.9 (a) and Figure 4.10 (b) shows the corresponding far-field scattered intensity distribution from which one can conclude that with the same profile but doubling the resolution, the forward scattered distribution has been improved but the backward scattered distribution has become worse. This is because the interface profile between

cytoplasm and surrounding medium is smooth (refer to Fig. 4.10 (a)). Figure 4.11 (a) shows a much sharper interface profile and Figure 4.11 (b) shows the corresponding scattered intensity distribution. This is improved in both forward and backward scattering.

In order to check if our simulation results in backward region are also sensitive to the cell size, we consider a case of surrounding medium index  $n = 1.35$ , cell index  $n_1 = 1.37$ , and cell radius  $a = 5.5\mu\text{m}$  with four different interface profiles which are equivalent to having four different effective cell sizes. In this consideration, we also choose the high resolution case of having 12 points per wavelength in propagation direction. Figure 4.10 (a), 4.12 (a) & (b), and 4.11 (a) show these four different interface profiles, from smooth to the sharper. Figure 4.13 (a) shows our simulation results in the backward region for these four different interface profiles. The solid line represents the scattered intensity distribution for the very sharp profile described by Fig. 4.11 (a). The dotted line represents the scattered intensity distribution for a less sharp profile described in Fig. 4.12 (b) while the dashed line represent the scattered intensity distribution for a reasonable smooth profile described in Fig. 4.12(a). The dash-dotted line is the backscattered intensity distribution for a smooth profile described in Fig. 4.10 (a). From Fig. 4.13 (a), we conclude that our simulation results in the backward region are very sensitive to our choice of interface profile, which, as we have seen above, corresponds to different choices of the effective cell size. On the other hand, Figure 4.13 (b) shows our simulation results in forward direction which are not sensitive to the effective cell size. We also consider a case of surrounding medium index  $n = 1.35$ , cell index  $n_1 = 1.37$ , and a very sharp interface profile described by Fig. 4.11 (a) with three different values of the cell radius  $a = 5.50, 5.49, \text{ and } 5.48\mu\text{m}$ . We also use 12 points per wavelength in propagation direction in this consideration. Our simulation results of the scattered intensity



distributions are plotted in Fig. 4.14, (a) for the backward region and (b) for the forward region. The solid line is the results of cell radius  $a = 5.50\mu m$ , the dashed line is the results of cell radius  $a = 5.49\mu m$ , and the dotted line is the results of cell radius  $a = 5.48\mu m$ . Our simulation results shows that there is a factor of 2 for backscattered intensities for these two cell sizes—cell radius  $a = 5.50\mu m$  and  $a = 5.48\mu m$ . Therefore, our simulation results in the backward region are very sensitive to the cell size which is predicted by Mie theory. However, in the forward region, our simulation results are not very sensitive to the cell size (refer to Fig. 4.14 (b)).

In summary, backward scattering is implemented in our simulation code. The simulation results and Mie theory predictions are different since Mie theory is an analytical solution of the full Maxwell's equations assuming a plane monochromatic wave incident upon a spherical surface, at which the profile between two media is a step function. However, in the case of high resolution (12 points per wavelength in propagation direction), our numerical simulation results of backward scattering are a good approximation to the exact solution and allows one to derive information on a cell's shape, size, and dielectric composition.

## 4.4 Conclusions

A new numerical technique for modelling laser light propagation in biological tissue has been developed and implemented as an optimized and parallelized three dimensional simulation code. This code can be used to efficiently model laser light scattering from both single cells and larger biological samples. For a typical simulation run on "Aurora", the supercomputer at the University of Alberta campus, utilizing 10 processors, requires less than 24 hours of real time. This code is non-paraxial, and can model both forward and backward scattering of laser light in biological tissues. The simulation results are reliable over the

range of  $0^\circ \pm 30^\circ$  for forward scattering and  $180^\circ \pm 20^\circ$  for backward scattering.

The 3-D code has some limitations—for example, the ratio of  $|\Delta\epsilon(x, y, z)/\epsilon_0| \leq 0.2$ , otherwise the code will experience convergence difficulties, since we treat  $\Delta\epsilon(x, y, z)$  as a perturbation; the code only solves the approximate scalar wave equation, so all polarization information is lost; and practically, the code cannot resolve structures on scales much smaller than the laser wavelength, as for example, the cell membrane. Polarization effects will be addressed in Chapter 7.

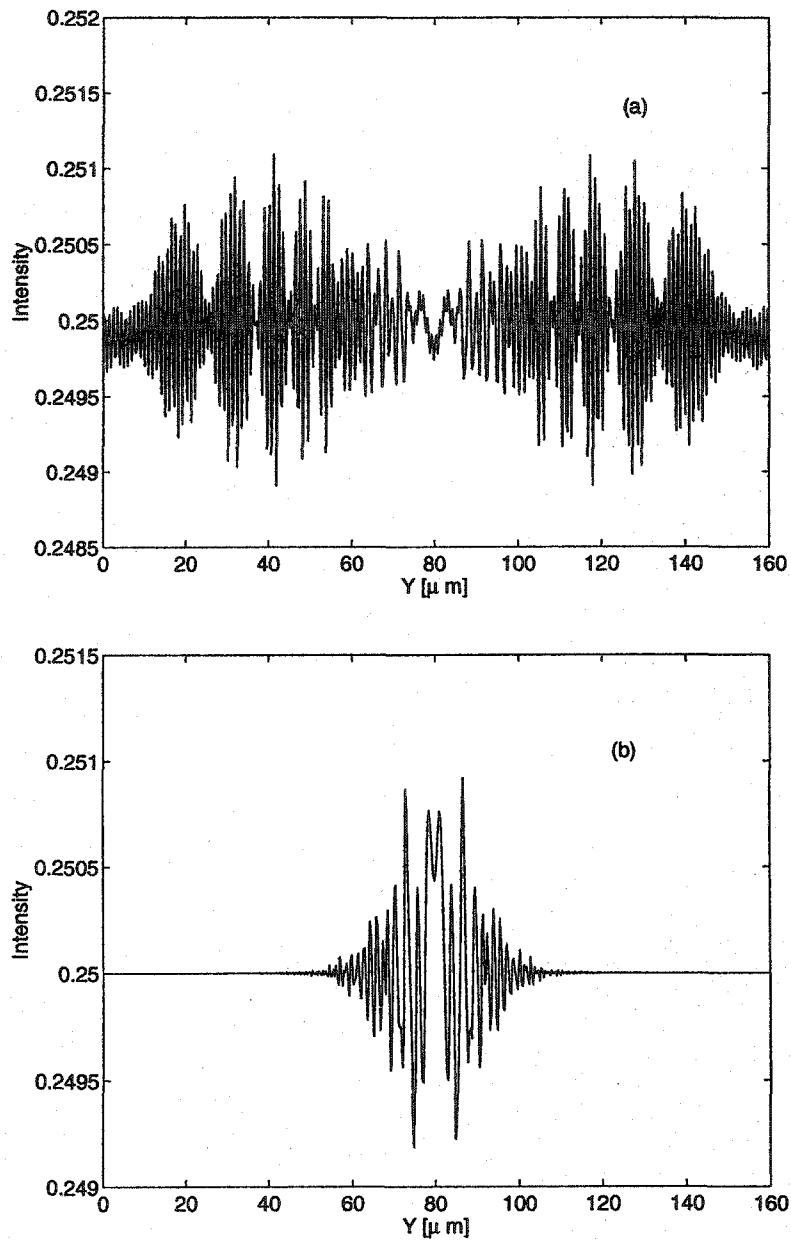


Figure 4.4: Backward scattering signals on the left boundary from a two dimensional cell with diameter of  $11\mu m$  and dielectric constant of 1.8769. The incident light is a plane wave with a wavelength of  $1\mu m$ . Figure (a) corresponds to the case where a cutoff is not imposed on large  $\vec{K}$  values while figure (b) gives results when a cutoff is used.

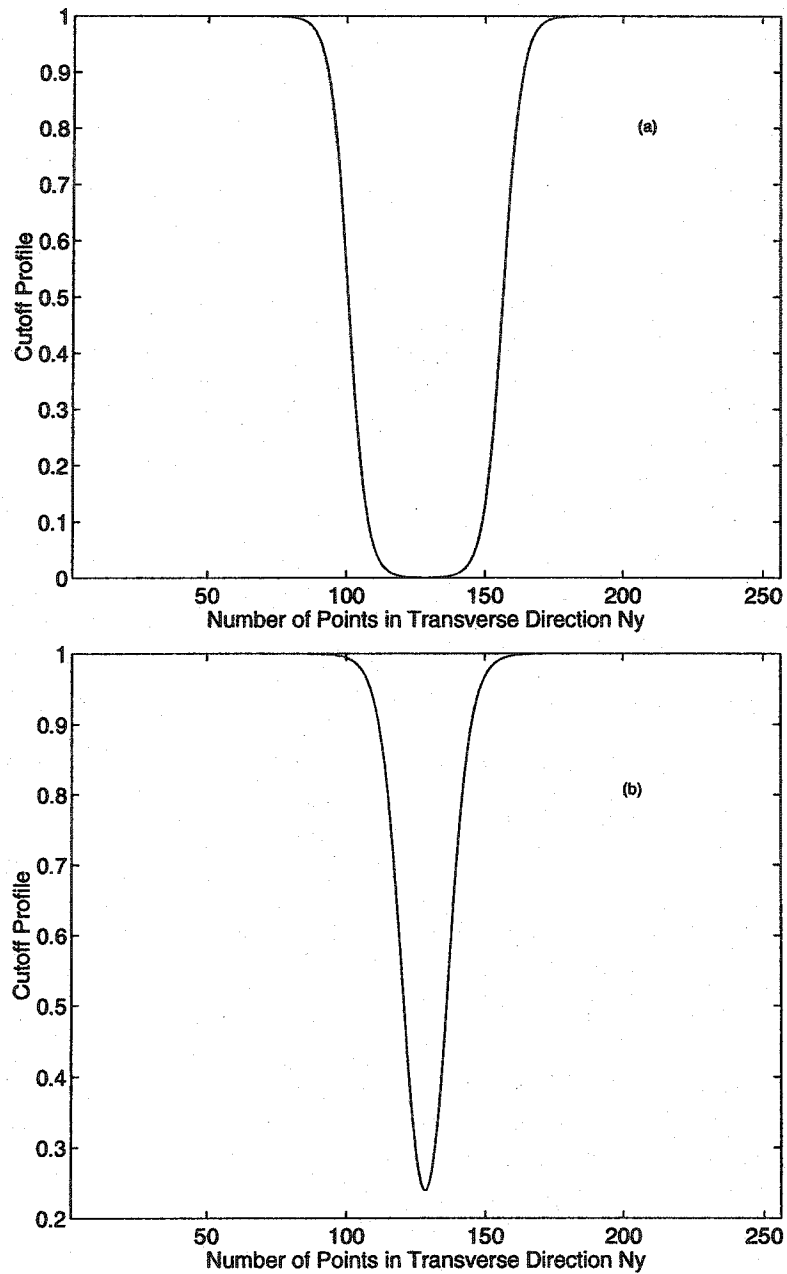


Figure 4.5: The profiles of smooth cutoff. Fig. (a) corresponds to the profile of more modes being cut off while Fig. (b) stands for the profile of less modes being cut off which means only extreme large  $\vec{K}$  being cut off. The largest mode in transverse direction can be expressed as  $K_{max} = k_y(N_y/2)$ .

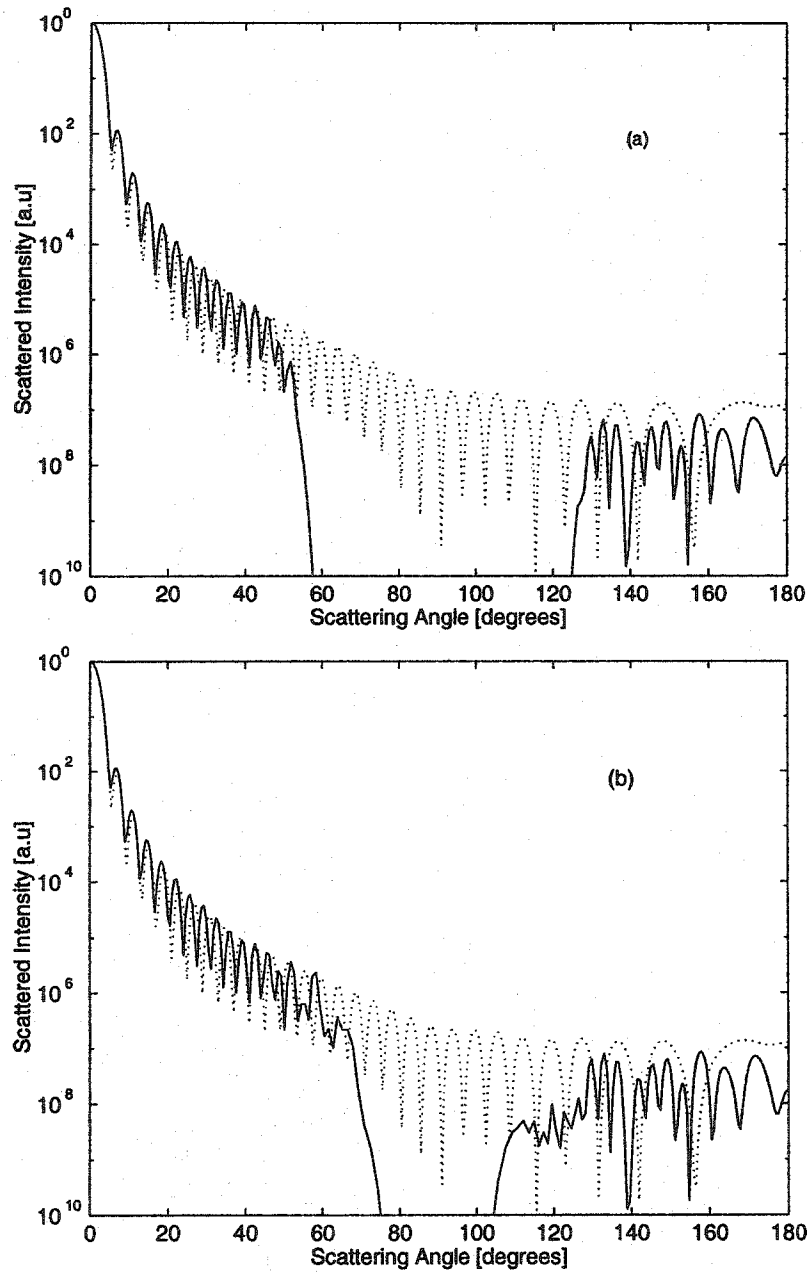


Figure 4.6: Scattering intensities in far-field. Fig. (a) shows the scattering intensity in far-field corresponding to the smoothly cutoff profile shown in Fig. 4.5 (a) and Fig. (b) is the scattering intensity in far-field corresponding to the smoothly cutoff profile shown in Fig. 4.5 (b). The dotted line in both Fig. (a) and (b) is the result of Mie theory.

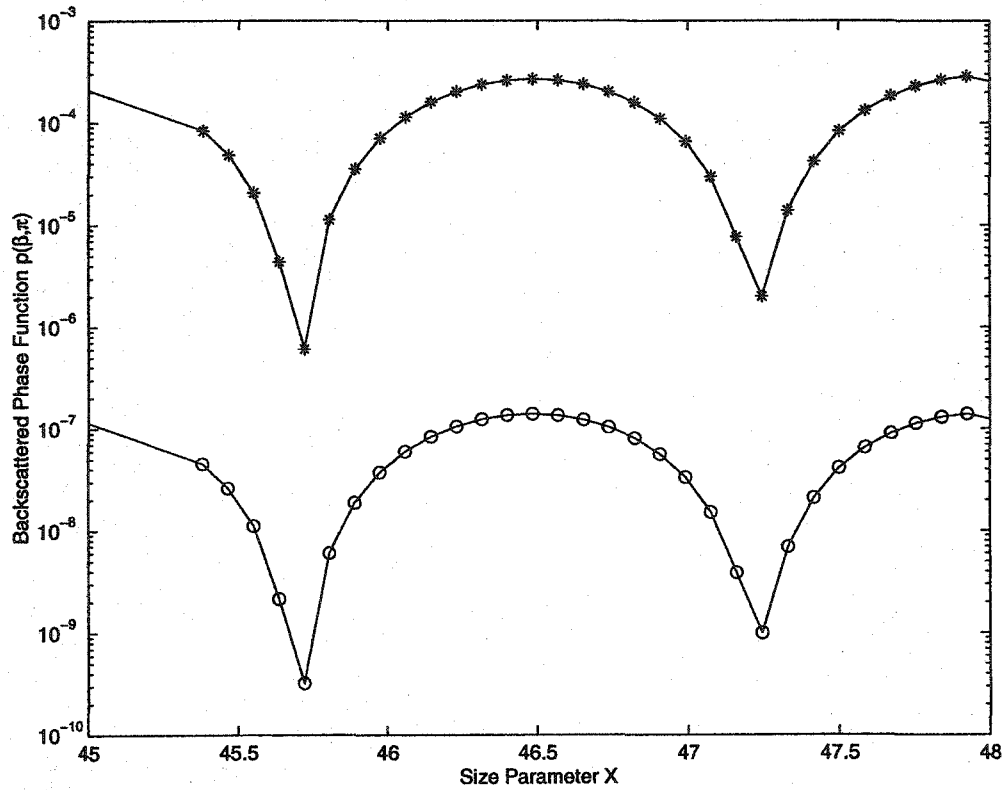


Figure 4.7: The backscattered phase function of Mie theory over a small range of size parameters for a surrounding medium with refractive index  $n = 1.35$ , the refractive index of cell  $n_1 = 1.37$ , and laser wavelength in vacuum  $\lambda_0 = 1.0 \mu m$ . The solid line with symbol 'o' represents the corresponding normalized backscattered intensity [a.u.].

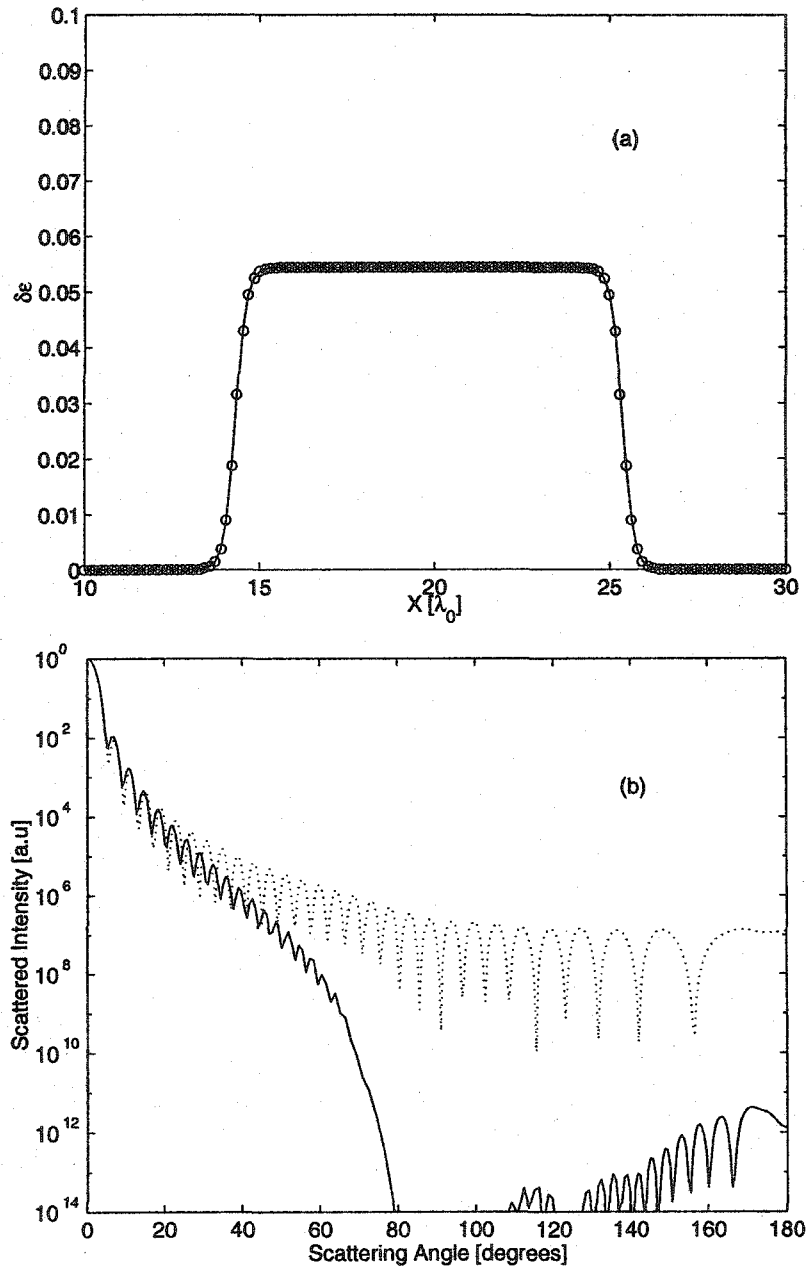


Figure 4.8: Smooth profile of the interface between cytoplasm and surrounding medium and its scattering intensity distribution. Fig. (a) shows a smooth profile of the interface between cytoplasm and surrounding medium. Fig. (b) is the scattering intensity in far-field corresponding to the gentle profile of the interface.

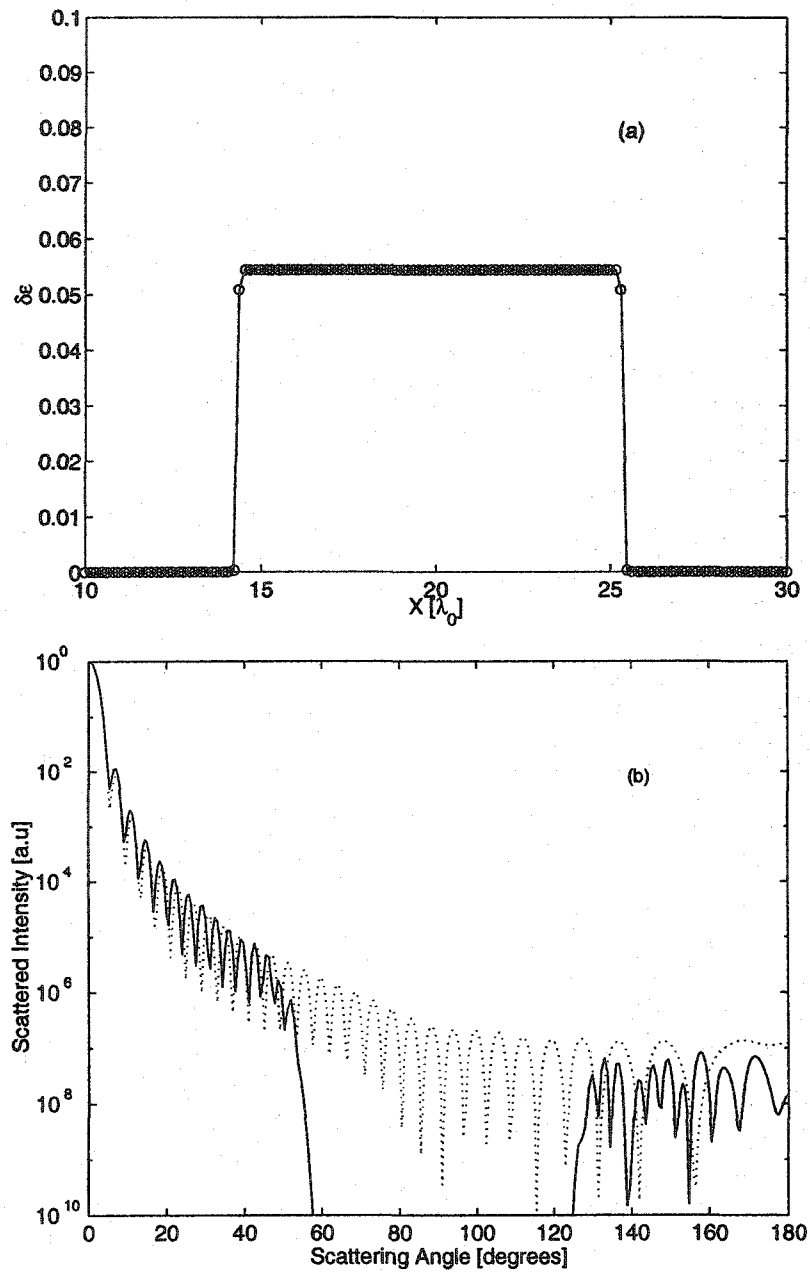


Figure 4.9: Sharp profile of the interface between cytoplasm and surrounding medium and its scattering intensity distribution. Fig. (a) shows a sharp profile of the interface between cytoplasm and surrounding medium. Fig. (b) is the scattering intensity in far-field corresponding to the sharp profile of the interface.



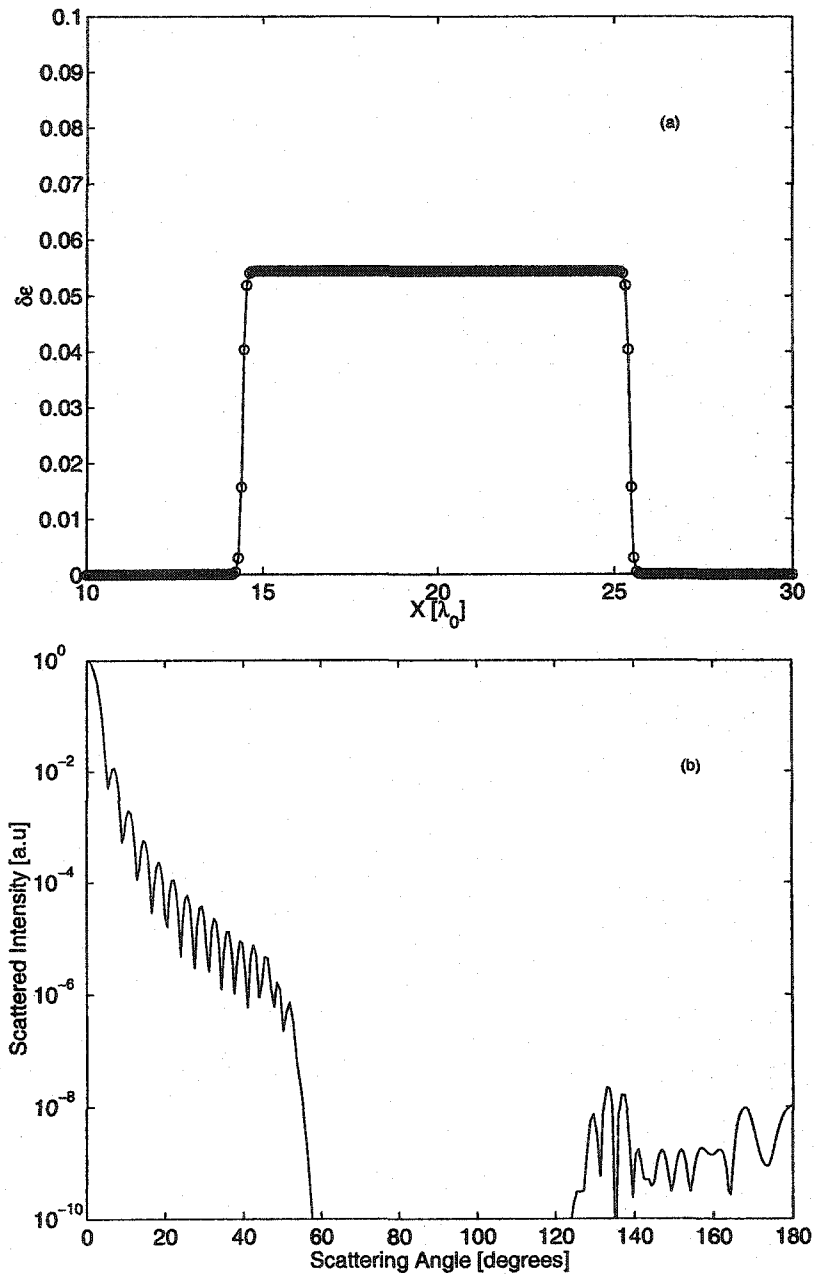


Figure 4.10: In the high resolution case, “smooth” profile of the interface between cytoplasm and surrounding medium and its scattered intensity distribution. Fig. (a) shows a smooth profile of the interface between cytoplasm and surrounding medium. Fig. (b) is the scattered intensity in far-field corresponding to the gentle profile of the interface.

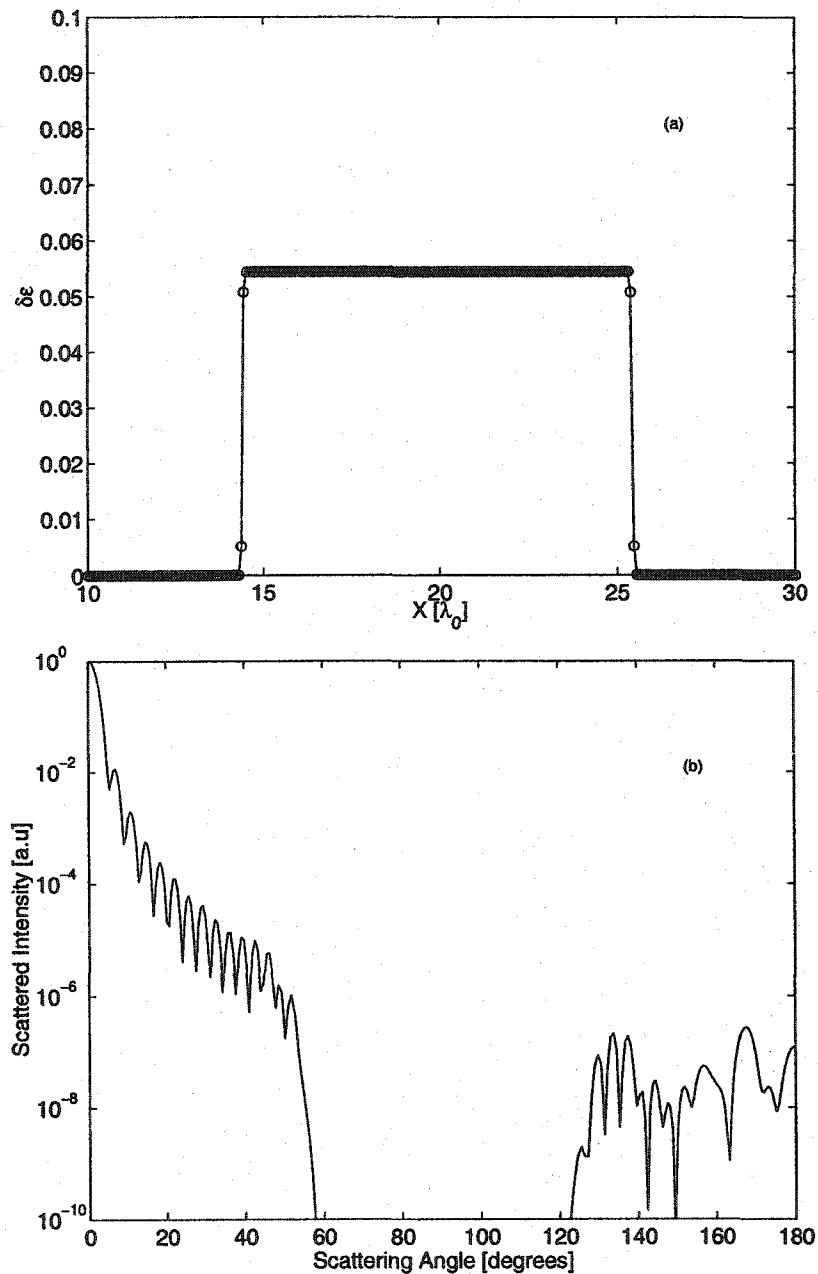


Figure 4.11: In the high resolution case, the much sharper profile of the interface between cytoplasm and surrounding medium and its scattering intensity distribution. Fig. (a) shows the much sharper profile of the interface between cytoplasm and surrounding medium. Fig. (b) is the scattered intensity in far-field corresponding to the sharpest profile of the interface.

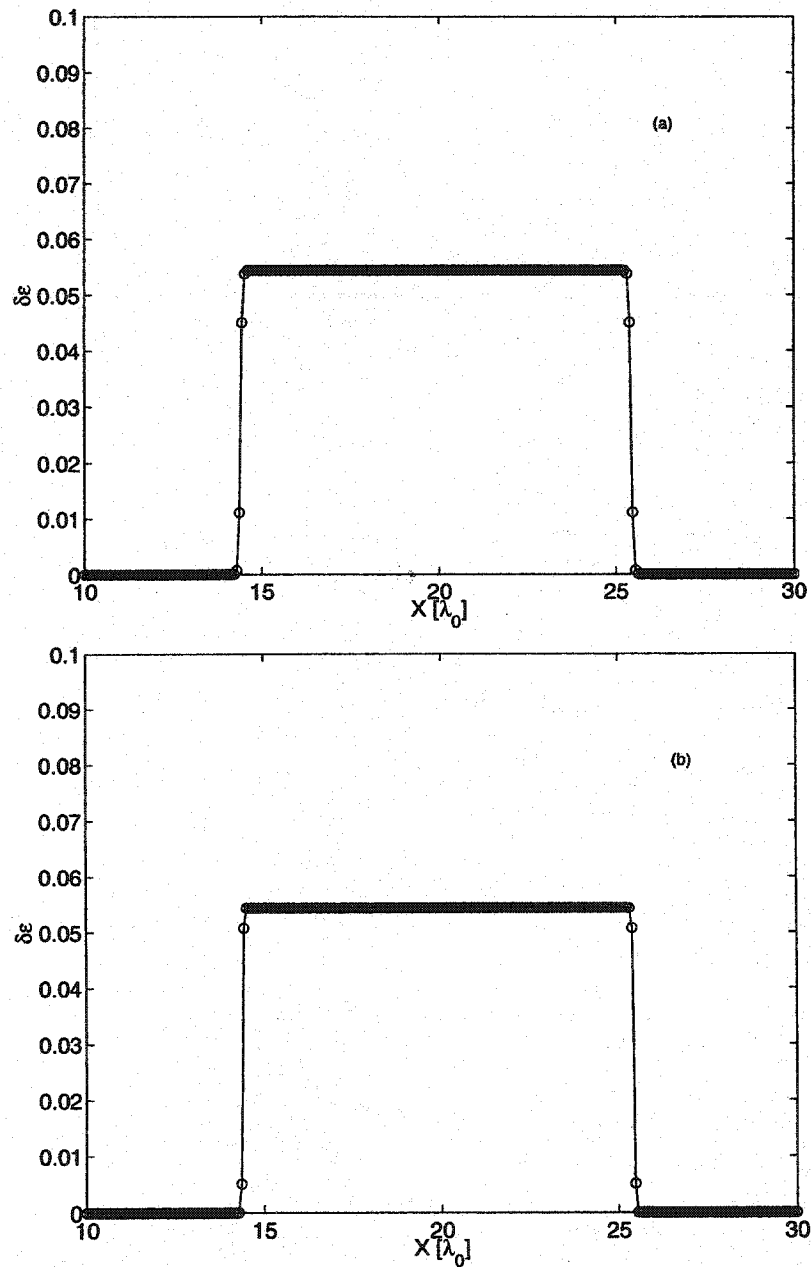


Figure 4.12: Two different profiles of the interface between cytoplasm and surrounding medium in the high resolution case of 12 points per wavelength.

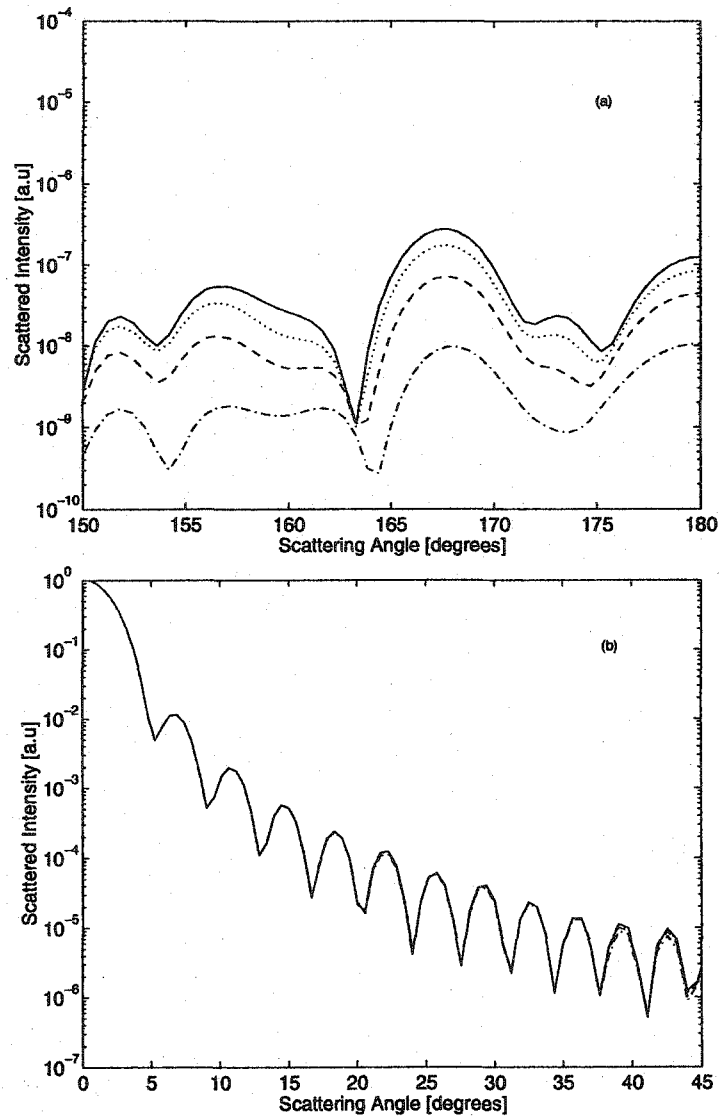


Figure 4.13: Simulation results of the scattered intensity distributions for four different profiles of the interface between cytoplasm and surrounding medium in the high resolution case of 12 points per wavelength. (a) backward direction and (b) forward direction. The solid line is the result of the very sharp interface profile described by Fig. 4.11 (a); the dotted line is the result of the sharp interface profile described by Fig. 4.12 (b); the dashed line is the result of the reasonable smooth interface profile described by Fig. 4.12 (a); the dash-dotted line is the result of the smooth interface profile described by Fig. 4.10 (a);

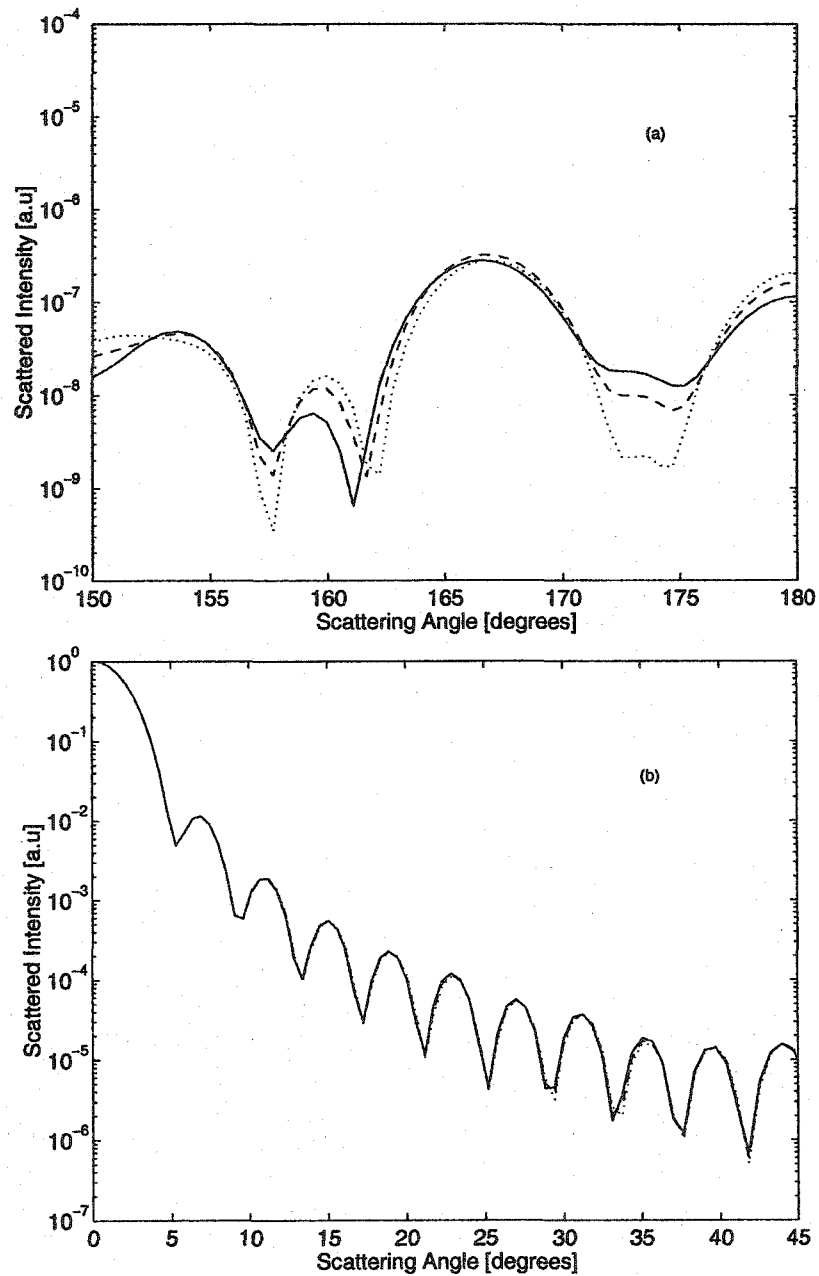


Figure 4.14: Simulation results of the scattered intensity distributions for different cell sizes with the very sharp profile (described by Fig. 4.11 (a)) of the interface between cytoplasm and surrounding medium in the high resolution case of 12 points per wavelength. (a) backward direction and (b) forward direction. The solid line is for cell radius  $a = 5.50 \mu m$ , the dashed line is for cell radius  $a = 5.49 \mu m$ , and the dotted line is for cell radius  $a = 5.48 \mu m$ .

## Bibliography

- [1] M. R. Amin, C. E. Capjack, P. Frycz, W. Rozmus, and V. T. Tikhonchuk, "Two dimensional simulations of stimulated Brillouin scattering in laser plasma," *Phys. Rev. Lett.* **71**, 81 (1993).
- [2] V. V. Eliseev, W. Rozmus, V. T. Tikhonchuk, and C. E. Capjack, "Effect of diffraction on stimulated Brillouin scattering from a single hot spot," *Phys. Plasma*, **3**, 3745 (1996).
- [3] V. V. Eliseev, I. Ourdev, W. Rozmus, V. T. Tikhonchuk, C. E. Capjack, and P. Young, "Ion wave response to intense laser beams in underdense plasmas," *Phys. Plasmas*, **4**, 4333 (1997).
- [4] D. Pesme, W. Rozmus, R. Rozmus, V. T. Tikhonchuk, A. Maximov, I. Ourdev, and C. H. Still, "Resonant instability of laser filaments in a plasma," *Phys. Rev. Lett.* **84**, 278 (2000).
- [5] J. D. Jackson, *Classical Electrodynamics* New York: Wiley, 1974.
- [6] W. H. Press, S. A. Teukolsky, W. T. Vetterling, and B. P. Flannery, *Numerical Recipes in FORTRAN* Cambridge University Press 1992, Second Edition.
- [7] M. Born and E. Wolf, *Principles of Optics* (Pergamon, Oxford, 1970).

[8] G. Mie, *Ann. d. Physik* (4), **30** 377(1908)

[9] Walter T. Grandy, Jr, *Scattering of Waves from Large Spheres*. Cambridge University Press, 2000.

## Chapter 5

# Two Dimensional Simulations of Light Scattering from Cells

### 5.1 Introduction

The previous two chapters dealt with the development of an algorithm upon which our simulations are based and the implementation and testing of the computer code. In this chapter, we present the two dimensional simulation results of light scattering from biological cells.

Although they cannot describe the “real world,” results from simulations in two dimensions are nevertheless useful in obtaining qualitative predictions for the behaviour of certain systems. In the 2-D case, we focus on plane wave scattering from both single and multiple cells.

Since we intend to model laser light propagation in biological tissue, we require values for the index of refraction of each cell component. The values listed in Table 5.1 were taken from the literature, and are used in all simulations in this thesis.



Cell component	Refractive index	Reference
Surrounding medium	1.35	[2]
Cytoplasm	1.37	[3]
Nucleus	1.39	[3]
Mitochondria	1.42	[4]

Table 5.1: The values for index of refraction of various cell components which are used in the simulations.

## 5.2 Scattering by Single Cells

In light scattering from cells, it is important to understand the role of a cell nucleus. For example, cancerous cells are characterized by a large nuclear to cytoplasmic volume ratio [1]. Three types of cells were chosen for our 2D simulations: cells without a nucleus, cells with a normal-size nucleus of diameter  $D_n = 3\mu m$ , and cells with a large nucleus of diameter  $D_n = 6\mu m$ . The cell diameter in all cases is  $D_0 = 11\mu m$ . The dielectric constant is related to the index of refraction by  $\varepsilon = n^2$ . Therefore, using the values from Table 5.1, we know that the dielectric constant of the inter-cellular medium is  $\varepsilon_0 = 1.8225$ . Similarly, we find that for the cytoplasm,  $\varepsilon = 1.8769$ , while for the nucleus  $\varepsilon = 1.9321$ . The incident laser light is assumed to be a plane wave with wavelength  $\lambda_0 = 1\mu m$ . The dependence of the scattered light intensity on the scattering angle is shown on a linear scale in Fig. 5.1(a) and on a logarithmic scale in Fig. 5.1(b). The transmitted component, which is the large peak at 0 degrees in Fig. 5.1(b), is removed by setting the intensity at 0 degree equal to its neighbour point intensity in Fig. 5.1(a).

From Fig. 5.1 it is clear that the dominant feature of the scattering pattern is forward (small-angle) scattering. Three different regions can be identified in the

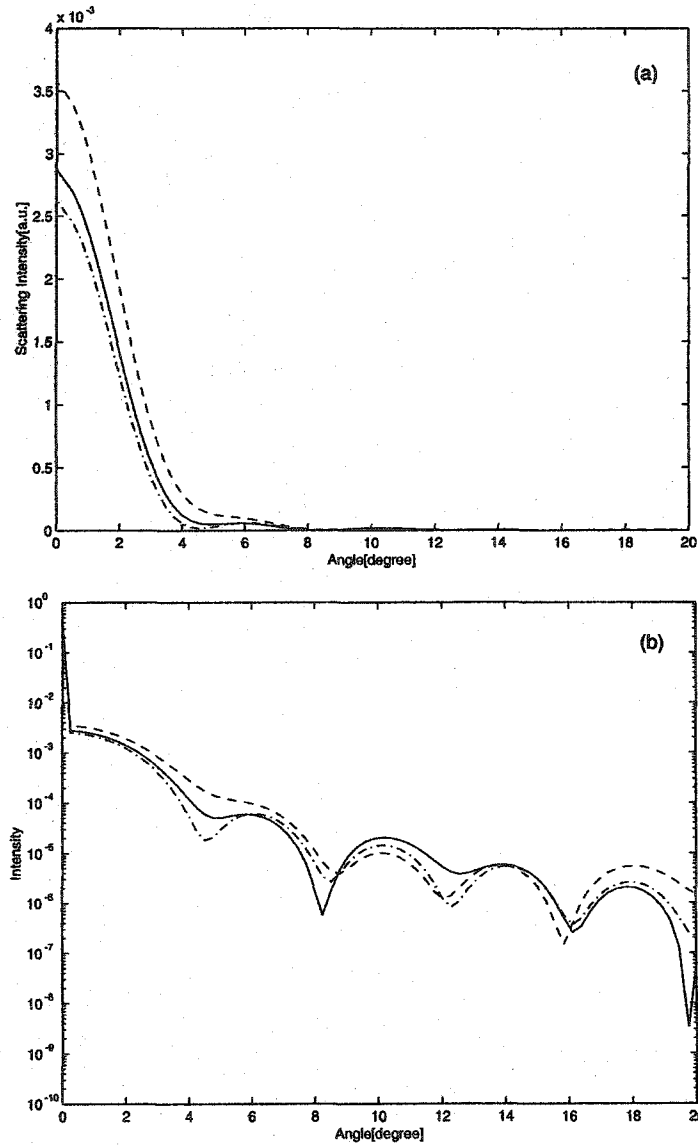


Figure 5.1: Scattering intensity from a two dimensional single cell with diameter  $D_0 = 11 \mu\text{m}$  on a linear scale (a) and on a semi-logarithmic scale (b). The dash-dotted line corresponds to a cell without nucleus, the solid line corresponds to a cell with a normal nucleus of diameter  $D_n = 3 \mu\text{m}$ , and the dashed line corresponds to a cell with a large nucleus of diameter  $D_n = 6 \mu\text{m}$ . The transmitted component, which is the large peak at 0 degrees in (b), is removed by setting the intensity at 0 degree equal to its neighbour point intensity in (a).

scattering pattern in Fig. 5.1. First, the angle interval from 0 to 0.25 degrees corresponds to the angular width of the incident light. The large scattering intensity over this range simply represents the signal from the incident light which is not scattered.

The second region, which extends from 0.25 to  $\theta_0 \approx 4$  degrees, contains the main part of the scattered light intensity. The width of this interval, characterized by value of  $\theta_0$ , is determined by the ratio of the typical cell size to the laser wavelength in the inter-cellular medium. A cell with a large nucleus scatters more light than a cell with a normal nucleus, while a cell with a normal nucleus scatters more light than a cell without nucleus. This is consistent with the predictions of linear perturbation theory (4.5), (4.6), and with the numerical results of Ref. [1].

Finally, for angles larger than  $\theta_0 \approx 4$  degrees, the scattering amplitude decreases rapidly with angle, so that large-angle scattering is small.

### 5.3 Scattering by many objects

In many realistic situations, the laser light propagates through a medium with many scattering objects (scatterers). For example, a biological tissue sample usually contains many cells. Therefore, the problem of light scattering by an ensemble of many identical scatterers is of fundamental importance. In this section, the scattering features of a medium with many scattering objects are discussed and compared to the scattering features of a single object. In our 2D simulations, the number of randomly distributed scattering objects in the simulation region was varied from 1 to 90. The scattering objects are assumed to have a diameter of  $D_0 = 7\mu m$  and a dielectric constant  $\epsilon = 1.8769$ . The dielectric constant of the surrounding medium is assumed to be  $\epsilon_0 = 1.8225$ . The incident light is assumed to be a plane wave with a wavelength  $\lambda_0 = 1\mu m$ .

Figure 5.2 shows a contour plot of the dielectric constant in a simulation region with 52 randomly distributed scatterers. Figure 5.3 illustrates the typical form of the relationship between the scattering intensity and the scattering angle. In this figure, the scattering intensities for the case of  $N = 10$  scatterers and for the case of single scatterer are compared. It is readily seen that the scattering intensity from  $N = 10$  scatterers does not have the regular pattern of minima and maxima that is observed when scattering from only a single object. At the same time, the scattering intensity, averaged over an interval of a few degrees, is a few times larger in the  $N = 10$  case than it is in the  $N = 1$  case. The increase of scattering intensity with the number of scatterers is observed at both small and large scattering angles.

In addition, up to 45 degrees scattering angle in Fig. 5.3, the distribution of scattered intensity from  $N = 10$  scatterers has a high frequency modulation and is enveloped by a scattering distribution from single scatterer. The phenomenon may be caused by interference effects between scatterers. One can conclude from Fig. 5.3 that the increase of the number of scatterers changes the scattering intensity, but not the characteristic angular features of scattering.

The dependence of scattering power and scattering angle on the number of scatterers is illustrated in Figs. 5.4(a) and (b), which combine results corresponding to two different lengths of the simulation region— $L = 160\mu m$  and  $L = 320\mu m$ . meanwhile, the width of the simulation region is  $160\mu m$  for both cases. Fig. 5.4(a) shows the fraction of scattered power, i.e., the power of light propagating outside the incident beam optics, as a function of the number of scatterers. The scattered power varies from about 4% of the incident power for a single scatterer to over 90% of the incident power for  $N = 90$  scatterers. From Fig. 5.4(a) it is evident that the scattered power does not depend on the length of the simulation region, but only on the number of scatterers. It can be expected

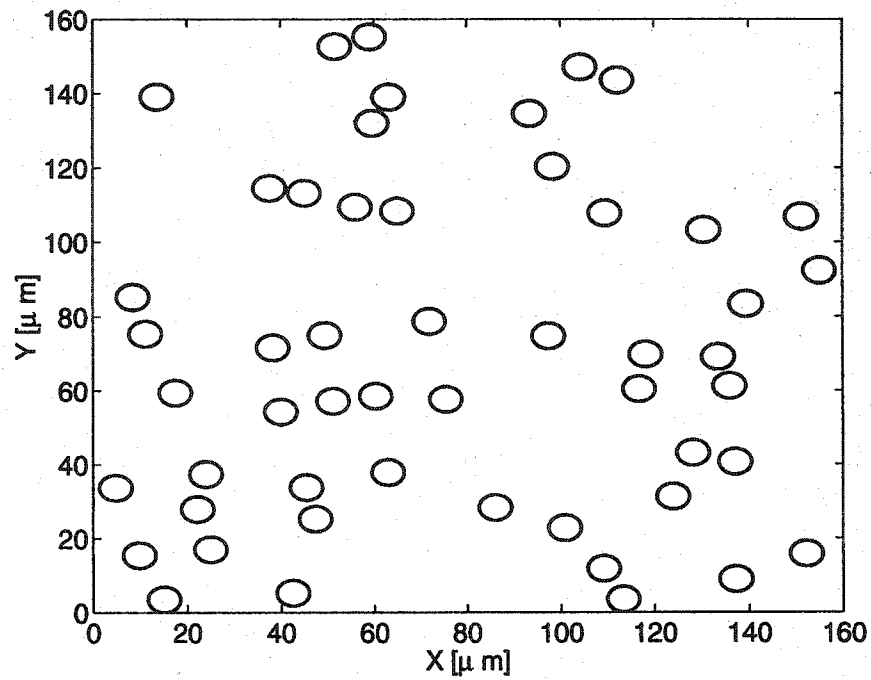


Figure 5.2: An example of the random distribution of scatterers in the simulation region. In this case, there are  $N=52$  scatterers.

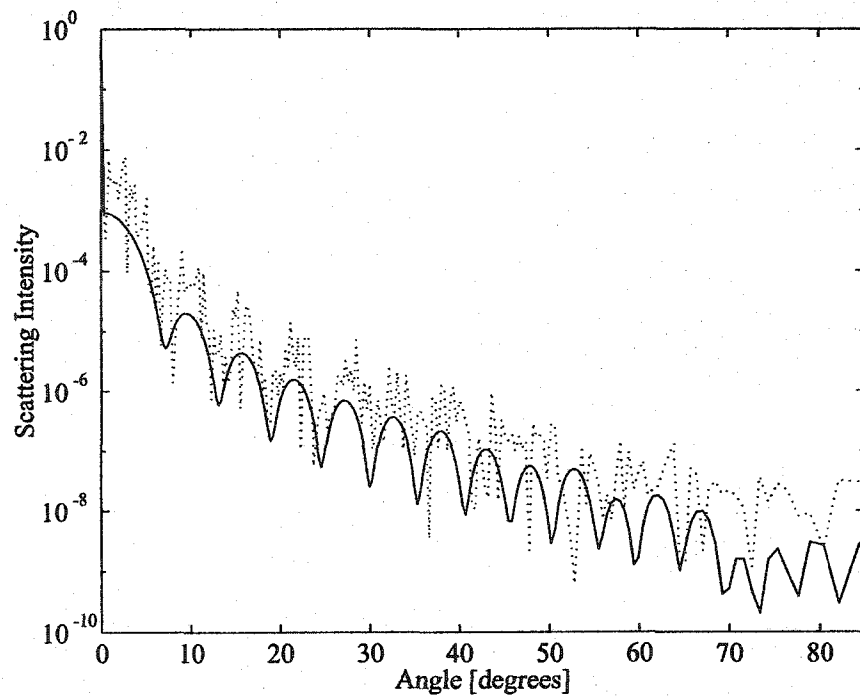


Figure 5.3: Scattering intensity as a function of scattering angle for 10 scatterers (dotted line) and for a single scatterer (solid line).

that, due to the multiple scattering, the scattered power will be close to 1 as the number of scatterers increases. The dependence of the scattered power on the number of scatterers [cf. Fig. 5.4(a)] is close to linear.

The angular width of the scattered light can be characterized by the average scattering angle  $\langle\theta\rangle$ , defined as

$$\langle\theta\rangle = \sqrt{[\int d\theta \theta^2 Q(\theta)]/[\int d\theta Q(\theta)]}. \quad (5.1)$$

Fig. 5.4(b) shows the dependence of the average scattering angle  $\langle\theta\rangle$  on the number of scatterers. It is evident from Fig. 5.4(b) that  $\langle\theta\rangle$  changes only slightly (by no more than 25%) as  $N$  changes from 1 to 90. The small dependence of the characteristic scattering angle  $\langle\theta\rangle$  on  $N$  is consistent with the angular spectrum of scattering intensity [cf. Fig. 5.3] that shown that amount of scattering increases, but without essential changes in the angular spectrum.

## 5.4 Conclusions

It has been demonstrated that the spectral method can be efficiently used in modelling laser light scattering for samples ranging in size from a single cell to large biological samples. In the case of laser light scattering from single cells, the most significant features of the angular distribution of the scattered light from various cells occur at small angles. Cells containing large nuclei have more scattering at small angles compared to cells containing normal-sized nuclei. The amplitude of scattering light decreases even further for cells without a nuclei. In the case of scattering from multiple cells, the simulation results show that the fraction of the scattered power depends on the number of scatterers and not on the size of simulation region. In fact, the fraction of the scattered power is almost linearly proportional to the number of scatterers. Finally, up to 40 degrees,

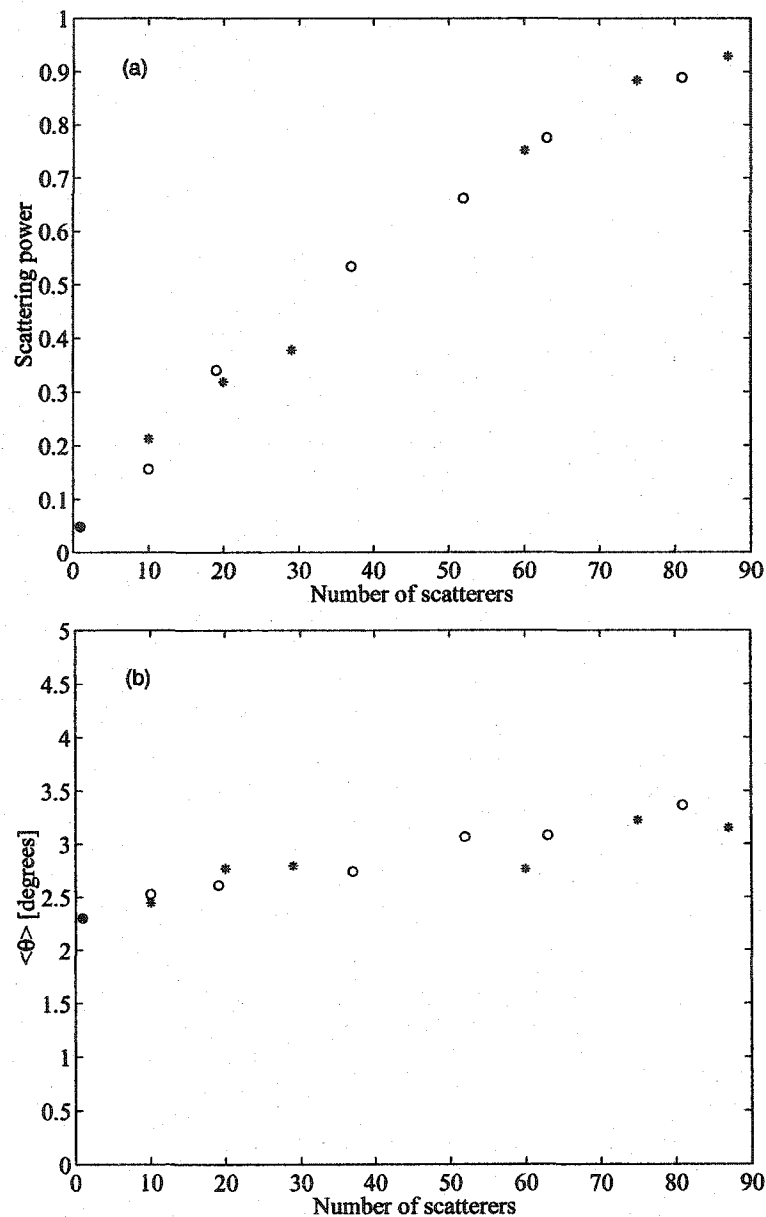


Figure 5.4: The dependence of scattered power (a) and the average scattering angle (b) on the number of scattering objects. The width of the simulation region is  $160 \mu m$ , while the length of the simulation region is either  $L = 160 \mu m$  (“o”) or  $L = 320 \mu m$  (“\*”).



the scattering pattern from many cells approximately retains the angular distribution characteristic of single cell forward scattering, but with high frequency modulation due to interference effects.

In the next chapter, we will consider the results from 3-dimensional simulations.

## Bibliography

- [1] Andrew Dunn, Colin Smithpeter, Ashley J. Welch, and Rebecca Richards-Kortum, *Journal of Biomedical Optics* **2**, 262-266 (1997).
- [2] J. Maier, S. Walker, S. Fantini, M. Franceschini, and E. Gratton, "*Possible correlation between blood glucose concentration and the reduced scattering coefficient of tissues in the near infrared,*" *Opt. Lett.* **19**, 2062-2064 (1994).
- [3] A. Brunsting and P. Mullaney, "*Differential light scattering from spherical mammalian cells,*" *Biophys. J.* **14**, 439-453 (1974).
- [4] H. Liu, B. Beauvoit, M. Kimura, and B. Chance, "*Dependence of tissue optical properties on solute-induced changes in refractive index and osmolarity,*" *J. Biomed. Opt.*, **1**, 200-211 (1996).

## Chapter 6

# Three Dimensional Simulation

## Results

### 6.1 Introduction

In the previous chapter, we discussed the results of our simulations of laser light scattering from cells in two dimensions. While these simulations enabled us to obtain a good qualitative understanding of the interaction between laser light and biological media, in addition to providing a useful testing ground for our new computational algorithm, two dimensional models, in the absence of certain symmetries, do not provide a complete general solution to the scattering problem. Therefore, in this chapter, we will turn to the treatment of a 3-dimensional model in which 3 spatial coordinates and a single component transverse E-field ( $E_y$ ) are considered. This model is exactly described by Eq. (3.9).

Since the 3-dimensional model more closely describes the true nature of the system, the results from the three dimensional simulations are very useful in obtaining quantitative predictions for the behaviour of laser-tissue interactions. These results therefore have many potential applications; for example, they would

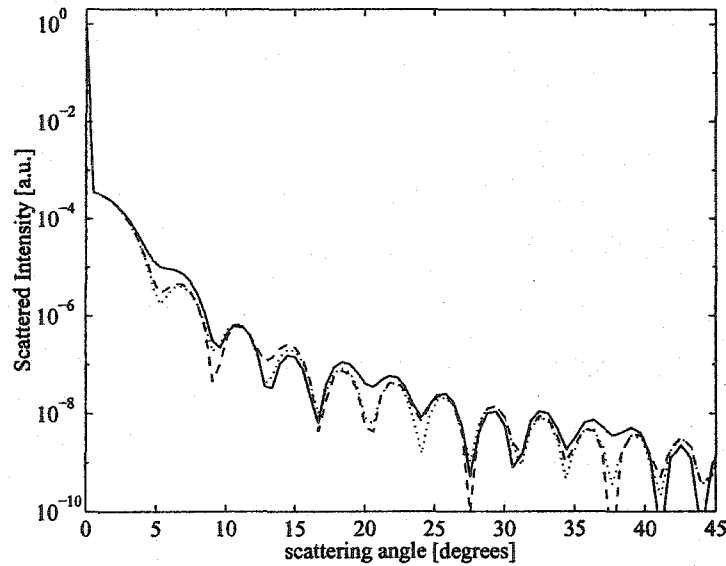


Figure 6.1: Scattered light intensity from plane wave for three types of cells : without a nucleus (dotted line), with a small nucleus  $D_n = 3\mu m$  (dashed line), and with a large nucleus  $D_n = 6\mu m$  (solid line). In all 3 cases, the cell diameter  $D_0 = 11\mu m$ . The nucleus is located in the center of the cell.

be useful in studies in micro-cytometry.

In the 3-D case, the incident laser light profile can either take the form of a plane wave or that of a Gaussian, and will experience scattering from both single and multiple cells. The values of the index of refraction for the various cell components are listed in Table 5.1.

## 6.2 Scattering by a Single Cell

In this section the influence of cell size and nucleus size on the scattering intensity are considered. Figures 6.1-6.4 show the angular spectra of light scattered by a spherical cell in 3D numerical simulations. The angular range shown in Figs. 6.1-6.4 is up to 45 degrees off the direction of incident light propagation.

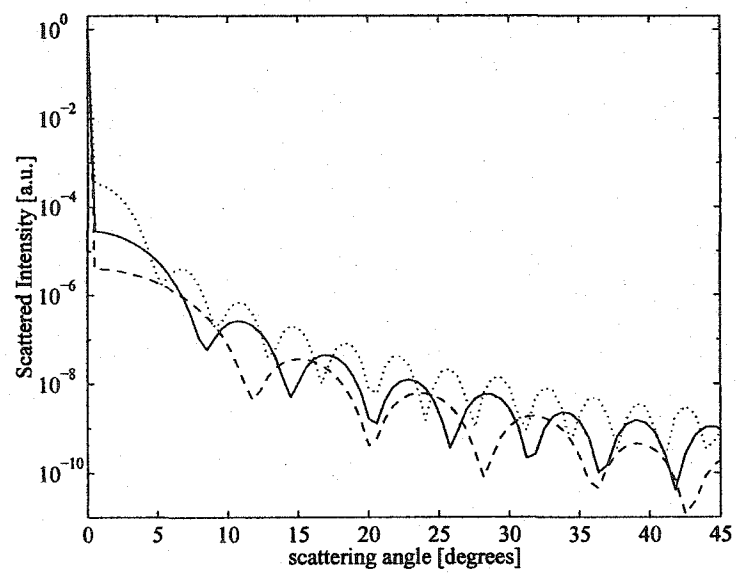


Figure 6.2: Scattered light intensity from plane wave for three sizes of cells that do not contain a nucleus : with diameter  $D_0 = 11 \mu m$  (dotted line), with diameter  $D_0 = 7 \mu m$  (solid line) and with diameter  $D_0 = 5 \mu m$  (dashed line).

Figures 6.1 and 6.2 show the angular spectra of scattered light in the case when the incident laser light is a plane wave with wavelength  $\lambda_0 = 1\mu m$ . The length of the simulation region is  $40\lambda_0$  in the direction of light propagation and  $80\lambda_0$  in each of the two transverse directions. In Fig. 6.1, three types of cells are chosen for our 3D simulations: a cell without a nucleus, a cell with a normal nucleus (the diameter of the nucleus  $D_n = 3\mu m$ ), and one with a large nucleus (the diameter of the nucleus  $D_n = 6\mu m$ ). The cell diameter in all cases is  $D_0 = 11\mu m$ . The refractive index of the inter-cellular medium is assumed to be  $n_0 = \sqrt{\epsilon_0} = 1.35$ . The cell components are cytoplasm (with refractive index  $n = 1.37$ ) and nucleus (with refractive index  $n = 1.39$ ). A spherical nucleus is located at the center of the spherical cell. Figure 6.2 shows the angular scattering spectra for cells without a nucleus, but with different diameters:  $D_0 = 11\mu m$ ,  $D_0 = 7\mu m$ , and  $D_0 = 5\mu m$ .

Spectra in Figs. 6.1, 6.2 have sharp maxima at zero angles, corresponding to the unscattered light. In our simulations with a plane wave, only a small fraction of light is scattered because the cell occupies only a small fraction of the simulation region cross-section. Figs. 6.1, 6.2 clearly show that the scattered light spectra have a characteristic width of a few degrees and that this width is consistent with the cell size : the smaller the cell size, the larger the angular width. In fact, the first minimum in the scattering pattern is approximately determined by the ratio of the incident laser wavelength and the diameter of the cells:  $\theta_m = \lambda/D$ . For example, three cases in Fig. 6.2 have the minimum near at  $5.2^\circ$ ,  $8.2^\circ$ , and  $11.4^\circ$ , respectively.

Figures 6.3, 6.4 show the angular spectra of scattered light in the case when the incident laser light is a Gaussian beam with wavelength  $\lambda_0 = 1.0\mu m$  and optical f-number of 3 (Fig. 6.3) and optical f-number of 10 (Fig. 6.4). Other parameters in the simulations with the Gaussian beam are the same as in simu-

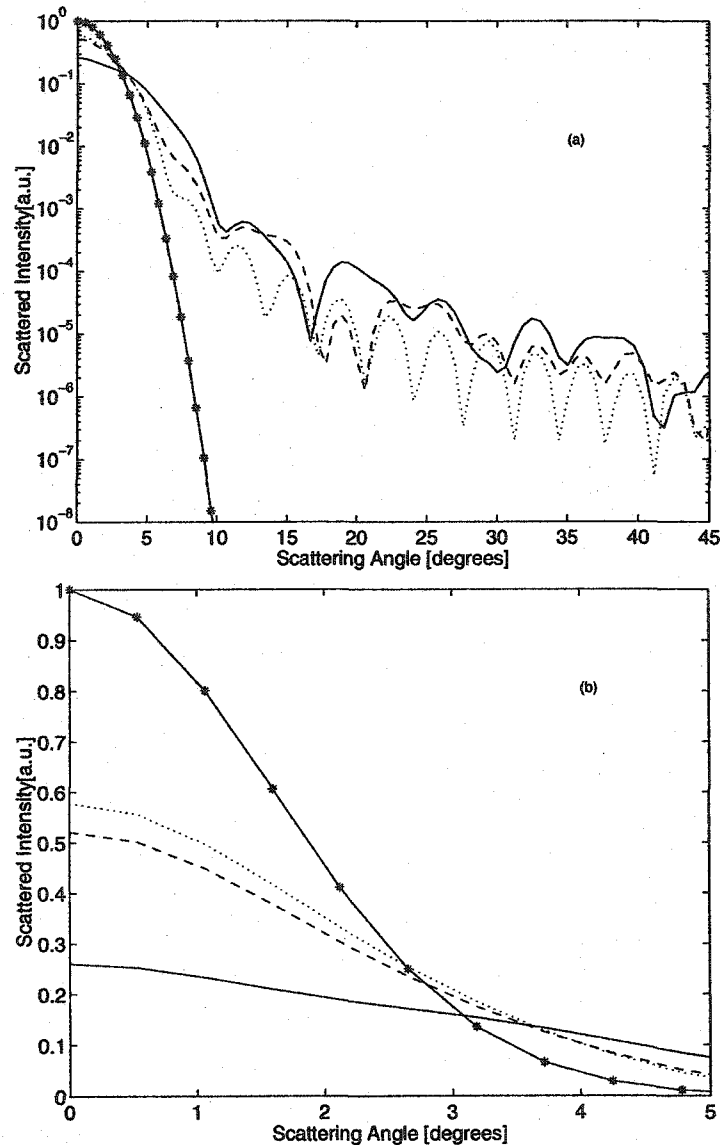


Figure 6.3: Scattered intensity from a Gaussian beam with  $f/3$  optics on a logarithmic scale (a) and linear scale (b) for three types of cells: without a nucleus (dotted line), with a small nucleus  $D_n = 3 \mu m$  (dashed line), and with a large nucleus  $D_n = 6 \mu m$  (solid line). In all cases, the cell diameter is assumed to be  $11 \mu m$  and the cell is located in center of the focal spot of the laser beam. The incident beam profile is given by the solid lines with the  $\star$  symbol.

lations with the plane wave incident light.

By comparing Figs. 6.3, 6.4 with Figs. 6.1, 6.2 one can see that in the case of Gaussian beams, the amount of scattered light is much larger than in the case of a plane wave. This is partially due to a stronger concentration of the total light beam on a cell. Fig. 6.1 also shows that the amount of scattered light can provide information about the dielectric permittivity of a cell. This information, combined with the information on the cell size from the width of angular spectrum, allows characterization of the basic cell features.

### 6.3 Backward Scattering

As described in Chapter 4, the backward scattering calculation is implemented in our simulation tool and information regarding the cell's size and dielectric can be derived from the backscattering intensity distribution. Figure 6.5 shows the scattering intensity from a three dimensional single cell with different diameters of  $D_0 = 11\mu m$ ,  $D_0 = 7\mu m$ , and  $D_0 = 5\mu m$ . The backscattering intensity distribution is plotted in Fig. 6.5 (b). The solid line corresponds to a cell with diameter  $D_0 = 11\mu m$ , the dotted line corresponds to a cell with diameter  $D_0 = 7\mu m$ , and the dashed line corresponds to a cell with diameter  $D_0 = 5\mu m$ . Figure 6.5 (b) shows that a cell with different size has a different backscattering intensity distribution. From the backward scattered spectra, one can conclude the first minimum away from the backward direction is proportional to the ratio of the incident laser wavelength and the cell diameter.

### 6.4 Multiple Scattering

The Henyey-Greenstein phase function [1] is often used to characterize the angular distribution of scattered light by tissue and it has the form of



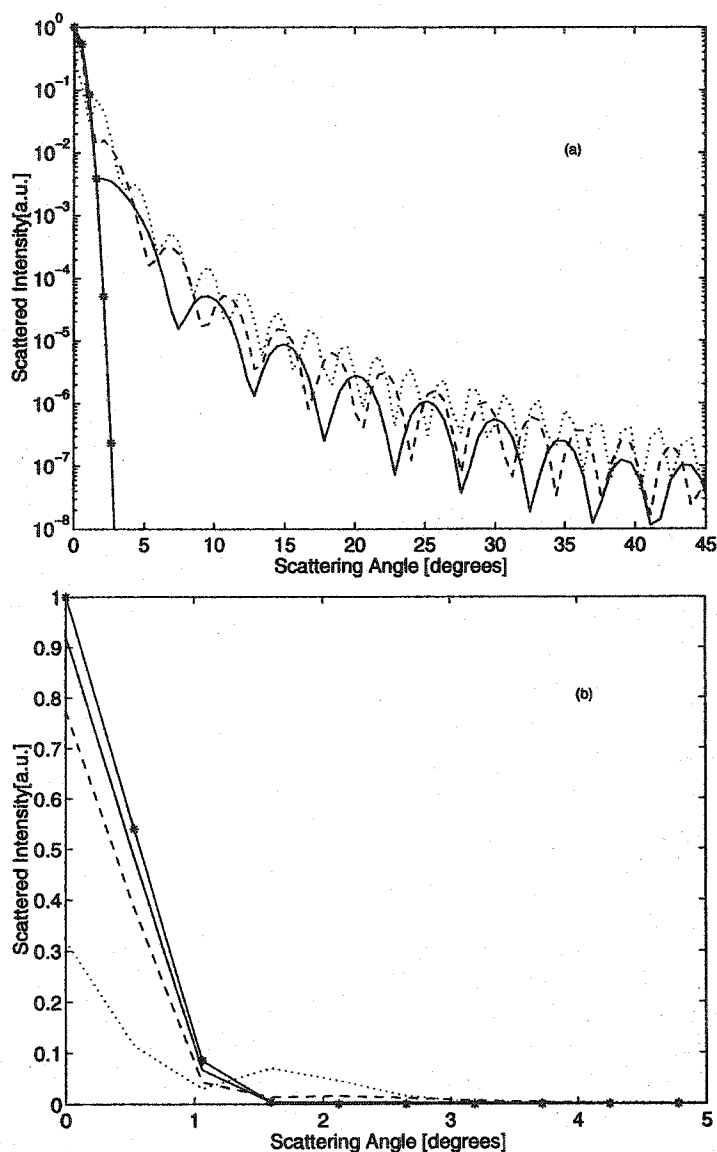


Figure 6.4: Scattered intensity from a Gaussian beam with  $f/10$  on a logarithmic scale (a) and linear scale (b) for three types of cells: with diameter  $D_0 = 17 \mu\text{m}$  (dotted line), with diameter  $D_0 = 11 \mu\text{m}$  (dashed line), and diameter  $D_0 = 8 \mu\text{m}$  (solid line). In all cases, the cell is without nucleus and is located in center of the focal spot of the laser beam. The incident beam profile is given by the solid lines with the  $\star$  symbol.

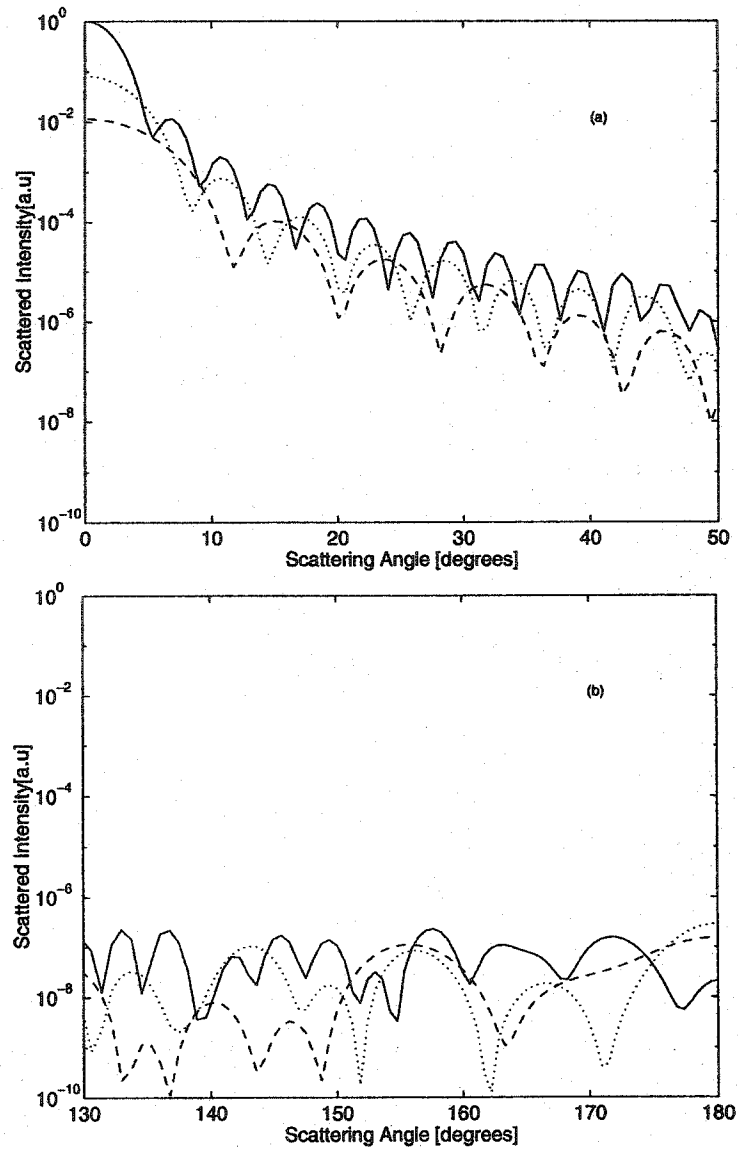


Figure 6.5: Forward scattering intensity (a) and backscattering intensity (b) from a three dimensional homogeneous cell with different diameters. The solid line corresponds to a cell with diameter  $D_0 = 11 \mu m$ , the dotted line corresponds to a cell with diameter  $D_0 = 7 \mu m$ , and the dashed line corresponds to a cell with diameter  $D_0 = 5 \mu m$ .

$$ph(\theta) = \frac{\gamma(1 - g^2)}{4\pi} \frac{1}{(1 + g^2 - 2g \cos \theta)^{3/2}} \quad (6.1)$$

where  $\theta$  is the phase angle or scattering angle,  $\gamma$  is the spherical albedo, and  $g$  is an anisotropic factor. The case where  $g = 1$  corresponds to the complete forward scatter and  $g = 0$  represents an isotropic distribution of the scattered light. This well-known Henyey-Greenstein phase function is used as another reference to check our three dimension simulation results, especially for the multiple scattering case. Using the simulation results, the anisotropic factor  $g$  is computed from the scattered distribution  $P(\theta)$ ,

$$g = \langle \cos \theta \rangle = \frac{\int_0^\pi P(\theta) \cos \theta \sin \theta d\theta}{\int_0^\pi P(\theta) \sin \theta d\theta}. \quad (6.2)$$

We consider the specific case where a plane wave incident laser with wavelength  $\lambda_0 = 1.0\mu m$  interacts with homogeneous cells with diameter of  $7\mu m$ . Figure 6.6 shows the scattering distribution of a laser interacting with a single cell. There are three curves in Fig. 6.6 : the solid line represents our numerical simulation result, the dotted line represents the Mie theory result, and the dashed line is the result of Henyey-Greenstein's phase function with  $g = 0.985$ . The calculated  $g$  factor is equal to 0.99. Thus, one can conclude that when a plane wave incident laser beam with wavelength  $\lambda_0 = 1.0\mu m$  interacts with homogeneous cells with a diameter of  $7\mu m$ , the scattering is almost completely forward. Figure 6.7 illustrates the difference between multiple (ten cells) and single scattering distributions. The amount of both forward and backward scattering from 10 cells is almost 10 times larger than that from a single cell.

The case of a plane wave incident laser with wavelength of  $1.0\mu m$  interacting with multiple homogeneous cells with diameter of  $7\mu m$  is now considered. Figure 6.8 (a) shows the scattered distribution from 18 homogeneous cells and Figure 6.8 (b) is for the scattered distribution from 34 homogeneous cells. The scattered distributions are characterized by the Henyey-Greenstein function with

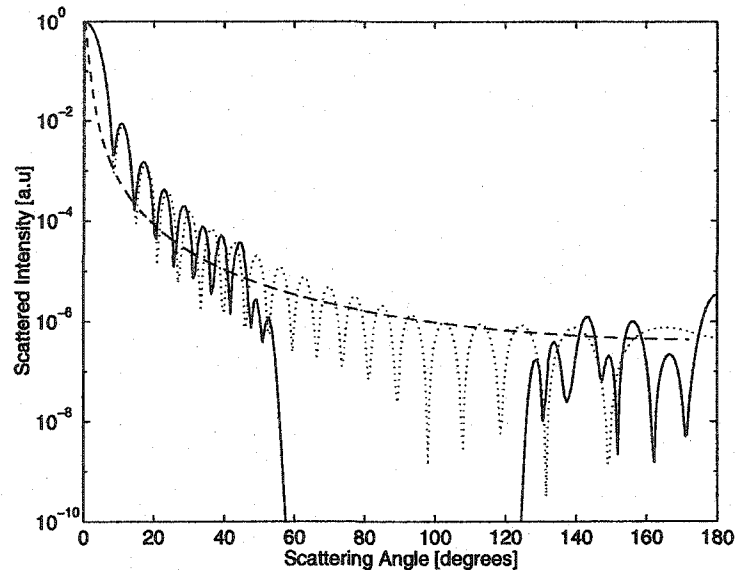


Figure 6.6: The scattering angular distribution from single cell. The solid line corresponds to the numerical simulation result, the dotted line corresponds to the Mie theory, and the dashed line corresponds to Henyey-Greenstein phase function with  $g$  factor value of 0.985.

$g = 0.985$ . The calculated  $g$  factor for both cases is equal to 0.99. Figure 6.9 shows the scattered intensity as a function of the number of cells (the simulation region has a dimension of  $40 \times 80 \times 80\lambda_0$ ). The inter-scattering amongst cells increases as the number of cells in the simulation box is increased. However, our simulation tool cannot quantify the amount of inter-scattering among cells.

## 6.5 Conclusions

In this chapter, an optimized and parallelized 3-spatial dimensions and one electric field component simulation code (3D scalar solver) has been used to efficiently model laser light scattering from both single cells and larger biological samples. In the case of laser light scattered by single cells, the cases of a plane wave and

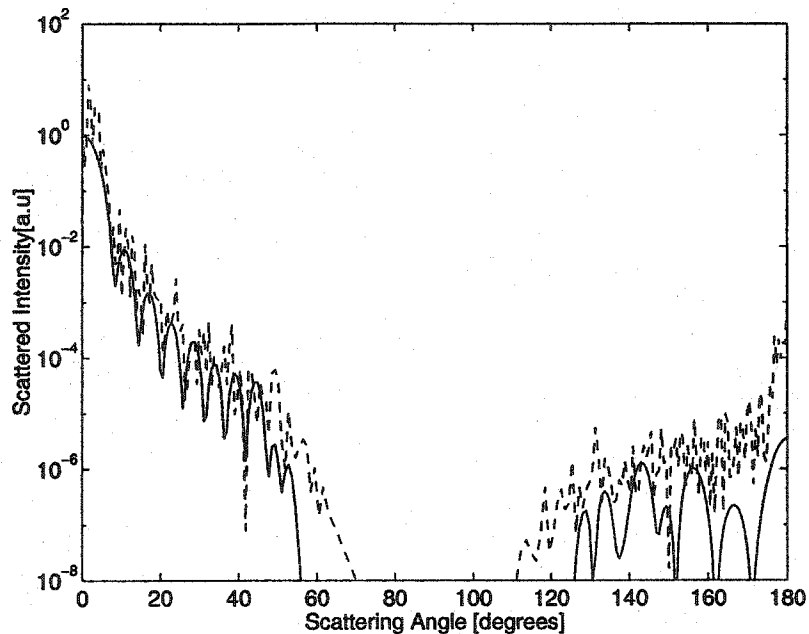


Figure 6.7: The difference of scattering angular distribution from 10 cells and from single cell. The solid line corresponds to the numerical simulation result for laser light scattering from a single cell with diameter of  $7\mu m$  and the dashed line corresponds to the numerical simulation result for laser light scattering from 10 cells with same size: diameter of  $7\mu m$ .

a Gaussian beam are used as incident laser light. The simulation results demonstrate that this 3D scalar solver is a valuable simulation tool in cell cytometry, for example, in the detection of rare event cells and cancerous cells. The healthy cell usually has a nucleus with diameter of  $3\mu m$  and the cancerous cell has a nucleus with diameter of  $6\mu m$ . The scattered spectra from a cell with a  $3\mu m$  diameter nucleus and with a  $6\mu m$  nucleus are different. The calculated  $g$  factor value indicates that scattering of a plane wave with both a single cell and multiple cells is an almost complete forward scattering.

The 3D scalar solver described in the previous chapters is unable to capture

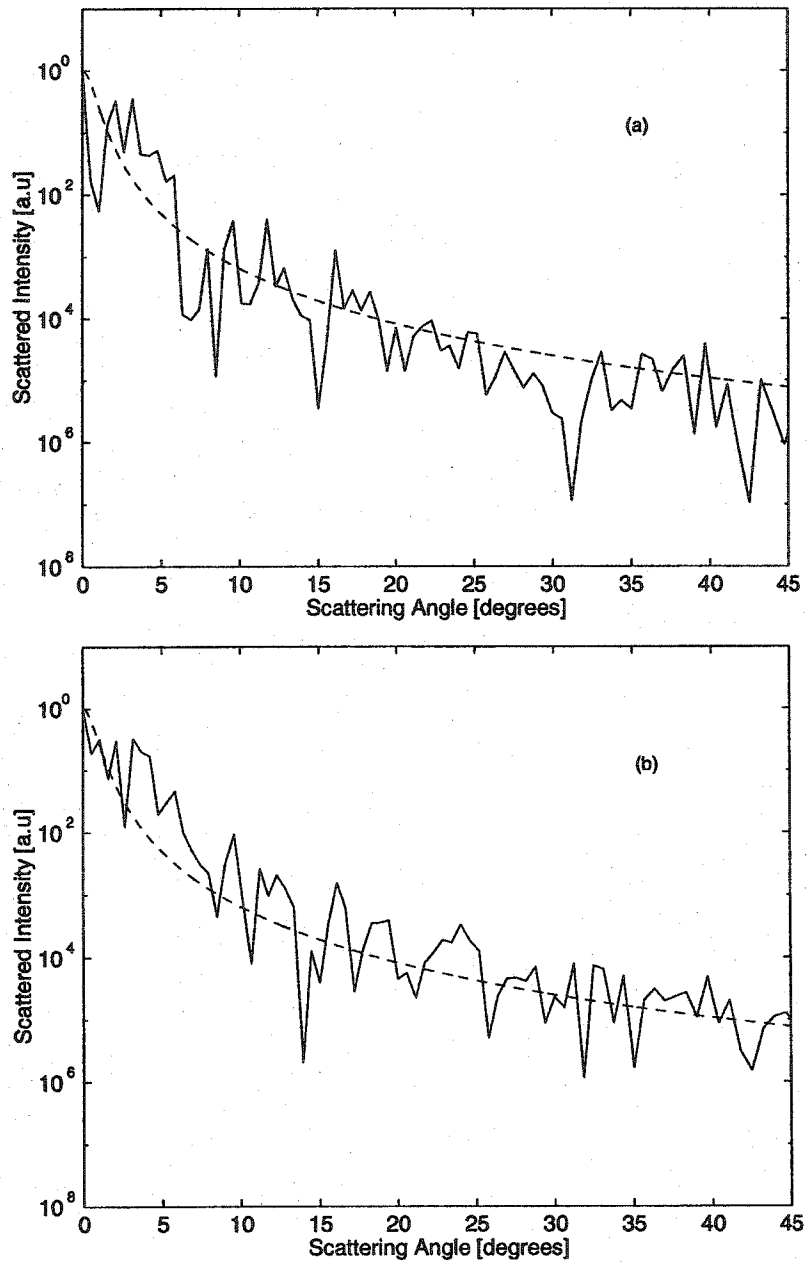


Figure 6.8: Multiple scattering distribution of laser light from 18 cells (a) and 34 cells (b). The solid stands for the calculated scattering and the dashed line represents the Henyey-Greenstein distribution.

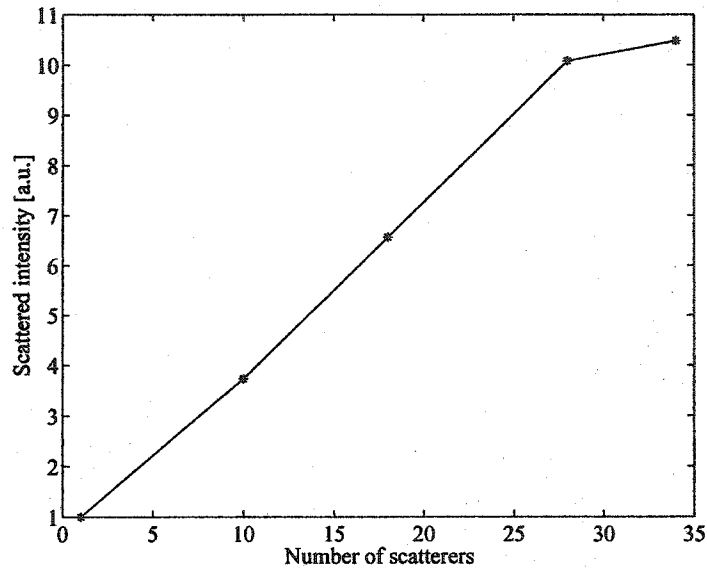


Figure 6.9: Dependence of the scattered intensity on the number of scatterers (cells).

any polarization information. In the next chapter, we will address solving the two field components wave equation and the three electric field components wave equation to explore the polarization effects in the process of laser light tissue scattering.

# Bibliography

- [1] Henyey and Greenstein, "Diffuse radiation in the galaxy," *Astrophys. J.* **93**  
pp.70-83, 1941



## Chapter 7

# Polarization Effects

### 7.1 Introduction

In the last several chapters, a new numerical technique for the solution of the scalar wave equation in both two and three spatial dimensions was developed, and the results of these simulations were presented and compared against theoretical predictions. Unfortunately, the scalar wave equation treatment is somewhat limited, as it does not take into account effects due to the polarization of light.

In this chapter, we explore the effects of polarization by solving a vector wave equations We begin with a simple review of the different polarization properties of light waves. Starting with Maxwell's equations, we derive a two component vector equation and present the numerical method that we use to solve it and some simulation results. Based on the success in solving the 2 electric field component vector wave equation, a vector wave equation with 3 electric field components will be derived and solved numerically. We conclude with a discussion of the numerical results obtained from 2 electric field component solver and 3 electric field component solver.

## 7.2 Polarization Properties of Light

### 7.2.1 Linearly Polarized Light

Light is simply an oscillating electromagnetic field. Since, in this work, we are interested in the interaction of laser light with biological tissue, we can restrict our consideration to the electric field components, as they will interact much more strongly with our media than the magnetic field components do. In the case of linearly polarized light, the electric field is oriented along the polarization axis. Therefore, we can describe light which is propagating along the  $x$  axis and linearly polarized along the  $y$  axis as follows:

$$\vec{E}_y = E_y^0 \sin(\omega t - kx + \phi_0) \vec{j}, \quad (7.1)$$

where the amplitude  $E_y^0$  is the magnitude of the electric field and  $\vec{j}$  is the unit vector in the  $y$ -direction. In an analogous manner, we may write light which is linearly polarized along the  $z$ -direction as:

$$\vec{E}_z = E_z^0 \sin(\omega t - kx + \phi_0) \vec{k}, \quad (7.2)$$

where  $\vec{k}$  is the unit vector oriented along the  $z$  axis. Since the electric field of linearly polarized light can be oriented in any direction perpendicular to the propagation direction, in the most general case, it can be described as a vector sum of  $\vec{E}_y$  and  $\vec{E}_z$ :

$$\vec{E} = (E_y^0 \vec{j} + E_z^0 \vec{k}) \sin(\omega t - kx + \phi_0). \quad (7.3)$$

Hence, linearly polarized light with arbitrary orientation of the polarization axis in the  $y$ - $z$  plane can be thought of as consisting of two components oriented along the  $y$  and  $z$  axis, respectively. The orientation of the polarization axis is determined by the relative magnitudes of the two components. Note that in the above discussion, we have taken the two components to have the same frequency  $\omega$  and the same absolute phase  $\phi_0$ .

### 7.2.2 Circularly Polarized Light

Let us now consider another special case, in which the electric field components have identical magnitudes  $E_0$ , but now a  $90^\circ$  phase difference exists between the two components:

$$\begin{aligned}\vec{E}_{rcp} &= E^0 \{ \sin[\omega t - kx + \phi_0] \vec{j} + \sin[\omega t - kx + \phi_0 + \pi/2] \vec{k} \} \\ &= E^0 \{ \sin[\omega t - kx + \phi_0] \vec{j} + \cos[\omega t - kx + \phi_0] \vec{k} \},\end{aligned}\quad (7.4)$$

or

$$\begin{aligned}\vec{E}_{lcp} &= E^0 \{ \sin[\omega t - kx + \phi_0] \vec{j} + \sin[\omega t - kx + \phi_0 - \pi/2] \vec{k} \} \\ &= E^0 \{ \sin[\omega t - kx + \phi_0] \vec{j} - \cos[\omega t - kx + \phi_0] \vec{k} \}.\end{aligned}\quad (7.5)$$

In equation (7.4), the subscript *rcp* stands for right circularly polarized light for which the polarization vector has constant amplitude, but rotates in the clockwise direction. Similarly, equation (7.5) describes left circularly polarized light, for which the polarization vector traces out a counterclockwise circular path.

Circularly polarized light can be viewed as being made up of linearly polarized components which are  $\pi/2$  radians out of phase with each other. Similarly linearly polarized light can be treated as being composed of equal quantities of right and left circularly polarized components. Therefore, in order to obtain a reasonable description of polarization effects in the case of the non-paraxial approximation or moderate angle forward and backward scattering, we must solve for these two perpendicular components of the electric field in the vector wave equation. However, in the case of larger angle forward and backward scattering, a wave equation with 3 field components should be considered. We will develop a wave equation with 2 field components further in the next section.

### 7.3 The Two Component Vector Wave Equations and Algorithm

As described in Chapter 3, we may use Maxwell's equations (3.1–3.4) to obtain:

$$\nabla(\nabla \cdot \vec{E}) - \nabla^2 \vec{E} + \frac{\epsilon}{c^2} \frac{\partial^2 \vec{E}}{\partial t^2} = 0. \quad (7.6)$$

Assuming propagation in the  $x$ -direction, we look for solutions for the specific case of 2 components vector field of the form

$$\vec{E} = [0, E_y(x, y, z, t)e^{-i\omega_0 t}, E_z(x, y, z, t)e^{-i\omega_0 t}]$$

so that the simulation results can be improved in small angle scattering and backward scattering. In addition, the 2 components vector field results can also provide the effects due to the polarization in the region of small angle forward and backward scattering. From Eq.(7.6) (neglecting the second derivative in time), we have

$$\begin{aligned} \hat{L}E_y &= -\frac{\omega_0^2 \Delta\epsilon}{c^2} E_y + \frac{\partial}{\partial y} \left( \frac{\partial E_y}{\partial y} + \frac{\partial E_z}{\partial z} \right) \\ \hat{L}E_z &= -\frac{\omega_0^2 \Delta\epsilon}{c^2} E_z + \frac{\partial}{\partial z} \left( \frac{\partial E_y}{\partial y} + \frac{\partial E_z}{\partial z} \right), \end{aligned} \quad (7.7)$$

where  $\hat{L} = \nabla^2 + \frac{2i\omega_0\epsilon_0}{c^2} \frac{\partial}{\partial t} + \frac{\epsilon_0\omega_0^2}{c^2}$ .

In a manner analogous with that discussed in Chapter 3, Eq. (7.7) is solved in a 3D region:  $0 \leq x \leq L_x$ ,  $-L_y/2 \leq y \leq L_y/2$  and  $-L_z/2 \leq z \leq L_z/2$  (see Fig. 3.2) by using the spectral method [1]. In the spectral method, we expand the electric field amplitude  $A$  as a Fourier series in the transverse ( $y$  and  $z$ ) directions, obtaining

$$A(x, y, z) = \sum_m \sum_{m'} A^{mm'}(x) \exp(imk_y y + im'k_z z), \quad (7.8)$$

where  $A$  stands for  $E_y$  and  $E_z$ ,  $k_y = 2\pi/L_y$ , and  $k_z = 2\pi/L_z$ . We then introduce dimensionless variables:

$$\begin{aligned} T &= \beta\omega_0 t/\varepsilon_0 \\ X &= kx \\ Y &= ky \\ Z &= kz, \end{aligned} \quad (7.9)$$

where  $k = 2\pi N/\lambda_0$ , with  $\lambda_0 = c/\omega_0$  being the laser wavelength in vacuum and  $N = \sqrt{\varepsilon_0}$  being the medium refractive index in the simulation region, and  $\beta$  is a dimensionless parameter which is used to renormalize the time  $T$  to some convenient unit (picoseconds, for example). This allows us to recast Eq. (7.7) in the following form:

$$\begin{aligned} \hat{P}E_y^{mm'} &= -\Delta\varepsilon E_y^{mm'} - \left(\frac{mk_y}{k}\right)^2 E_y^{mm'} - \frac{mk_y m' k_z}{k^2} E_z^{mm'} \\ \hat{P}E_z^{mm'} &= -\Delta\varepsilon E_z^{mm'} - \left(\frac{m' k_z}{k}\right)^2 E_z^{mm'} - \frac{mk_y m' k_z}{k^2} E_y^{mm'}, \end{aligned} \quad (7.10)$$

where

$$\begin{aligned} \hat{P} &= 2i\beta \frac{\partial}{\partial T} + \frac{\partial^2}{\partial X^2} + K_{Xmm'}^2 \\ K_{Xmm'}^2 &= \varepsilon_0 - (mk_y/k)^2 - (m' k_z/k)^2. \end{aligned} \quad (7.11)$$

We use the same numerical technique described in Chapter 3 to solve these coupled wave equations (7.10). In particular, the time iteration is implemented as described in section 3.3, namely, by the implicit midpoint rule [2] [3]. We must generalize this somewhat, however, since we are now dealing with two components. We should develop a symmetrical approach to solve the symmetrical equations (7.10) so that  $E_z^n$  and  $E_y^n$  are advanced in the same way. In this scenario, we compute the midpoint values of  $\tilde{E}_z$  and  $\tilde{E}_y$  from initial values of  $E_z^n$  and  $E_y^n$ . It is then possible to compute the iterated values for  $E_z^{n+1}$  (using  $\tilde{E}_z$  and  $\tilde{E}_y$ ) and  $E_y^{n+1}$  (using  $\tilde{E}_z$  and  $\tilde{E}_y$ ).

## 7.4 Simulation Results

Following the algorithm described in above section and based on our three-dimensional parallelized code (3D scalar solver), another version of three-dimensional parallelized code (3D-2 components vector solver) was implemented to solve equations (7.10). The expression for the total intensity used in the code is the same as that defined in Mie theory. It takes form:

$$I = (|E_y|^2 + |E_z|^2) \quad (7.12)$$

In order to test the 3D-2 components vector solver, we consider the special case where there are no cells in the simulation region (see Fig. 3.2). In this case, equations (7.10) become two independent free propagating equations. When the incident light is represented by two identical plane waves for  $E_y$  and  $E_z$ , the simulation results in far-field are found to be comprised of two identical delta functions — which is physically correct.

We now consider the case where the incident laser light is comprised of two identical plane wave components with wavelength  $\lambda_0 = 1\mu m$  for both  $E_y$  and  $E_z$ , and a homogeneous cell (without nucleus) is placed in the simulation region. The diameter of the cell is assumed to be equal to  $11\mu m$  and the refractive index of the inter-cellular medium and cytoplasm are taken the values from Table 5.1 (1.35 for the inter-cellular medium and 1.37 for the cytoplasm). The length of the simulation region is  $40\lambda_0$  in the light propagating direction and  $80\lambda_0$  in each of the two transverse directions. The simulation results are plotted in Fig. 7.1. Figure 7.1 (a) shows the angular spectra of forward scattered light while Fig. 7.1 (b) gives the backscattering results. In both Fig. 7.1 (a) and (b), the solid line is for  $|E_y|^2$ , the symbol + is for  $|E_z|^2$ , and the dotted line is for the results of the 3D scalar solver using the same simulation conditions. Since equation (7.10) is a symmetrical equation and the initial conditions for  $E_y$  and  $E_z$  are the same, the

simulation results should be the same for  $E_y$  and  $E_z$ . Indeed, from Fig. 7.1 (a) and (b), one can see that the angular distribution of scattered light for the two orthogonal electric field components are identical.

Initially, the direction of polarization is  $45^\circ$  from the  $Y$  axis in the  $Y - Z$  plane ( $\vec{E}^0 = \vec{E}_y^0 + \vec{E}_z^0$ ) and the degree of the linear polarization is equal to 1 since the two orthogonal components are initially identical. After scattering, we have  $|E_y|^2 = |E_z|^2$  for forward and backward scattering (see Fig. 7.1). Therefore, for the scattered light, the direction of polarization is  $45^\circ$  from the  $Y$  axis in  $Y - Z$  plane and the degree of polarization is 1.

Figure 7.2 shows our simulation results of the scattered intensity parallel to the scattering plane  $i_{\parallel}$  (solid line) and the scattered intensity perpendicular to the scattering plane  $i_{\perp}$  (dash-dotted line) in forward direction (a) and backward direction (b). From Figure 7.2 (a), we can find that there is a discrepancy between  $i_{\parallel}$  and  $i_{\perp}$  for scattering angle  $\theta \geq 30^\circ$  which agrees with Mie theory's prediction (refer to Fig. 2.4). This may be a reason for the breakdown of the scalar approximation. Figure 7.3 shows the comparison of our simulation results using a 3D -2 component vector solver with the Mie theory results (a) for  $i_{\parallel}$  and (b) for  $i_{\perp}$ . For both  $i_{\parallel}$  and  $i_{\perp}$ , there is a good agreement up to scattering angle  $\theta = 30^\circ$ .

## 7.5 The Three Components Vector Wave Equation

In this section, we will explore the effects of polarization by solving the 3 spatial dimension, 3 electric field components vector wave equation. Recalling Eq. (3.6) and using assumptions of  $\mu = 1$  and  $\varepsilon = \varepsilon_0 + \Delta\varepsilon(x, y, z)$ , one has

$$2i \frac{\omega_0}{c^2} \varepsilon_0 \frac{\partial \vec{E}}{\partial t} + \nabla^2 \vec{E} + \frac{\omega_0^2}{c^2} \varepsilon_0 \vec{E} - \nabla(\nabla \cdot \vec{E}) = -\frac{\omega_0^2}{c^2} \Delta\varepsilon \vec{E}. \quad (7.13)$$

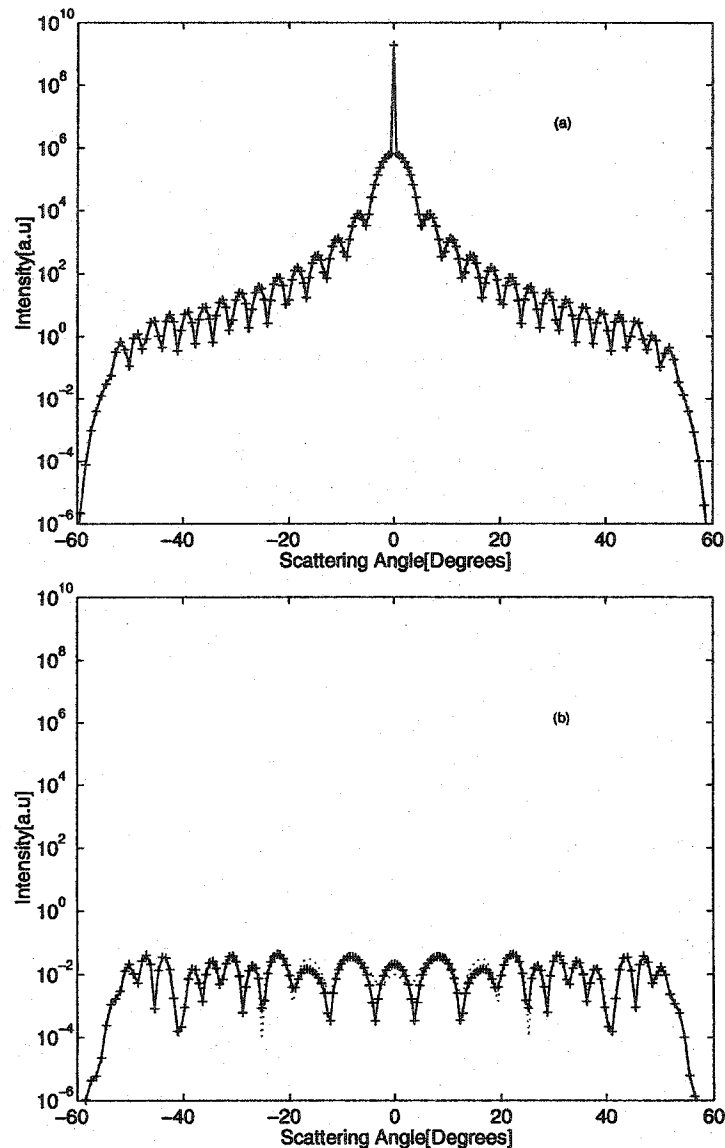


Figure 7.1: The angular spectra of forward and backward scattered lights for two orthogonal vector components. Figure (a) is for the forward scattered component and (b) is the backward scattered component off a three dimensional single cell with diameter  $D_0 = 11\mu m$ . The solid line is for  $|E_y|^2$ , the symbol + is for  $|E_z|^2$ , and the dotted line represents results obtained with the 3D scalar solver for the same simulation conditions.



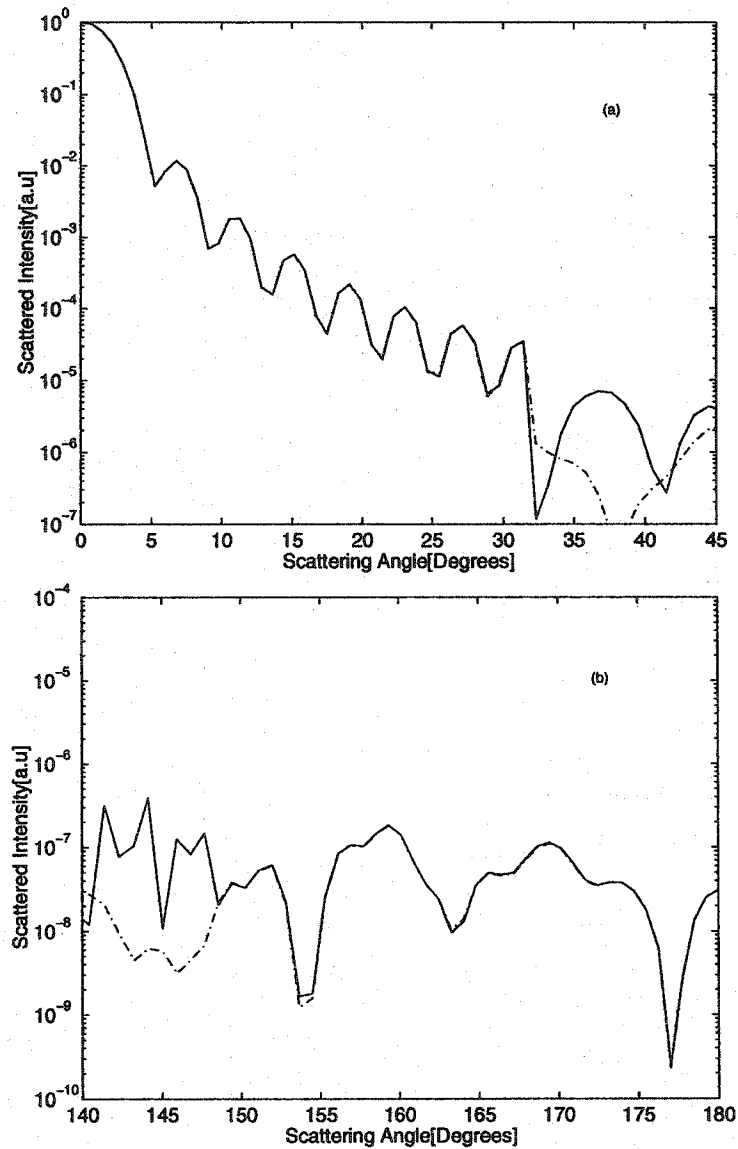


Figure 7.2: Scattering by a cell with diameter  $D_0 = 11\mu m$ —the simulation results of two components vector wave equation solver. The forward scattering and backward scattering are shown in Fig. (a) and (b) in which solid line represents  $i_{\parallel}$  and dash-dotted line represents  $i_{\perp}$ .

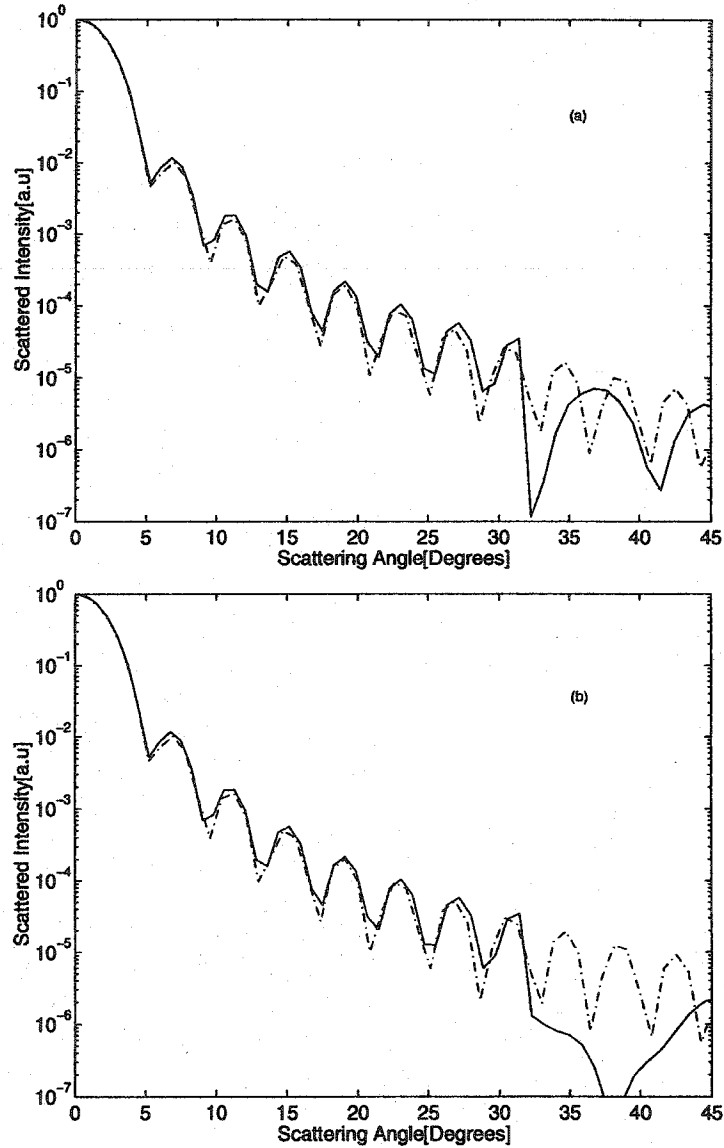


Figure 7.3: Comparison of our simulation results  $i_{\parallel}$  (a),  $i_{\perp}$  (b) with Mie theory results. The solid line represents our simulation results and dash-dotted line represents Mie theory results.

After Fourier transform with respect to transverse coordinates  $(y, z)$ , one obtains the following equations for three Fourier components  $E_y^{mm'}(x)$ ,  $E_z^{mm'}(x)$ , and  $E_x^{mm'}(x)$ :

$$2i\frac{\omega_0}{c^2}\varepsilon_0\frac{\partial E_y^{mm'}}{\partial t} + \left(\frac{\partial^2}{\partial x^2} - (mk_y)^2 - (m'k_z)^2 + \frac{\omega_0^2}{c^2}\varepsilon_0\right)E_y^{mm'} = -m^2k_y^2E_y^{mm'} - mk_y m'k_z E_z^{mm'} + imk_y \frac{\partial E_x^{mm'}}{\partial x} - \frac{\omega_0^2}{c^2}\Delta\varepsilon E_y^{mm'} \quad (7.14)$$

$$2i\frac{\omega_0}{c^2}\varepsilon_0\frac{\partial E_z^{mm'}}{\partial t} + \left(\frac{\partial^2}{\partial x^2} - (mk_y)^2 - (m'k_z)^2 + \frac{\omega_0^2}{c^2}\varepsilon_0\right)E_z^{mm'} = -(m'k_z)^2 E_z^{mm'} - mk_y m'k_z E_y^{mm'} + im'k_z \frac{\partial E_x^{mm'}}{\partial x} - \frac{\omega_0^2}{c^2}\Delta\varepsilon E_z^{mm'} \quad (7.15)$$

$$2i\frac{\omega_0}{c^2}\varepsilon_0\frac{\partial E_x^{mm'}}{\partial t} + \left(\frac{\partial^2}{\partial x^2} - (mk_y)^2 - (m'k_z)^2 + \frac{\omega_0^2}{c^2}\varepsilon_0\right)E_x^{mm'} = imk_y \frac{\partial E_y^{mm'}}{\partial x} + im'k_z \frac{\partial E_z^{mm'}}{\partial x} + \frac{\partial^2 E_x^{mm'}}{\partial x^2} - \frac{\omega_0^2}{c^2}\Delta\varepsilon E_x^{mm'} \quad (7.16)$$

Instead of solving Eq. (7.16) for longitudinal component  $E_x^{mm'}$ , it is possible to use Eq. (3.1) which is one of Maxwell's equations in charge free region,  $\nabla \cdot \varepsilon \vec{E} = 0$ . This gives the following equation:

$$\nabla \cdot \left(\vec{E} + \frac{\Delta\varepsilon}{\varepsilon_0}\vec{E}\right) = 0. \quad (7.17)$$

After taking Fourier transfer in  $y$  and  $z$  directions, Eq. (7.17) becomes

$$\frac{\partial}{\partial x} \left(E_x^{mm'} + \frac{(\Delta\varepsilon E_x)^{mm'}}{\varepsilon_0}\right) + imk_y \left(E_y^{mm'} + \frac{(\Delta\varepsilon E_y)^{mm'}}{\varepsilon_0}\right) + im'k_z \left(E_z^{mm'} + \frac{(\Delta\varepsilon E_z)^{mm'}}{\varepsilon_0}\right) = 0. \quad (7.18)$$

The term of  $\frac{\partial}{\partial x} \left(\frac{(\Delta\varepsilon E_x)^{mm'}}{\varepsilon_0}\right)$  on the left hand side of Eq. (7.18) can be neglected compared to other terms. Then from Eq. (7.18), one easily finds:

$$i\frac{\partial E_x^{mm'}}{\partial x} = mk_y \left(E_y^{mm'} + \frac{(\Delta\varepsilon E_y)^{mm'}}{\varepsilon_0}\right) + m'k_z \left(E_z^{mm'} + \frac{(\Delta\varepsilon E_z)^{mm'}}{\varepsilon_0}\right). \quad (7.19)$$

Therefore, Eqs. (7.19), (7.14), and (7.15) construct a complete system.

Using dimensionless variables of Eq. (7.9), the complete system becomes

$$\hat{P}E_y^{mm'} = -\Delta\varepsilon E_y^{mm'} - \left(\frac{mk_y}{k}\right)^2 E_y^{mm'} - \frac{mk_y m' k_z}{k^2} E_z^{mm'} + i \frac{mk_y}{k} \frac{\partial E_x^{mm'}}{\partial X} \quad (7.20)$$

$$\hat{P}E_z^{mm'} = -\Delta\varepsilon E_z^{mm'} - \left(\frac{m'k_z}{k}\right)^2 E_z^{mm'} - \frac{mk_y m' k_z}{k^2} E_y^{mm'} + i \frac{m'k_z}{k} \frac{\partial E_x^{mm'}}{\partial X} \quad (7.21)$$

$$i \frac{\partial E_x^{mm'}}{\partial X} = \frac{mk_y}{k} \left( E_y^{mm'} + \frac{(\Delta\varepsilon E_y)^{mm'}}{\varepsilon_0} \right) + \frac{m'k_z}{k} \left( E_z^{mm'} + \frac{(\Delta\varepsilon E_z)^{mm'}}{\varepsilon_0} \right), \quad (7.22)$$

where

$$\begin{aligned} \hat{P} &= 2i\beta \frac{\partial}{\partial T} + \frac{\partial^2}{\partial X^2} + K_{Xmm'}^2 \\ K_{Xmm'}^2 &= \varepsilon_0 - (mk_y/k)^2 - (m'k_z/k)^2, \end{aligned} \quad (7.23)$$

and  $\beta$  is a dimensionless parameter which is used to renormalize the time  $T$  to a unit of picosecond.

In order to solve Eqs. (7.21—7.22) numerically, the numerical technique described in Chapter 3 and an algorithm presented in section 7.3 are used. We calculate the value of  $i \frac{\partial E_x^{mm'}}{\partial X}$  using initial values of  $E_y^n$  and  $E_z^n$ . The results are substituted into Eq. (7.21) and (7.22) for the midpoint values of  $\tilde{E}_y$  and  $\tilde{E}_z$  calculations. In the next step, the value of  $i \frac{\partial E_x^{mm'}}{\partial X}$  is updated by using the midpoint values of  $\tilde{E}_y$  and  $\tilde{E}_z$  for  $E_y^{n+1}$  and  $E_z^{n+1}$  calculations. A new version of the three spatial dimension parallelized code (3D-3 components vector solver) was implemented.

We again consider the case described in section 7.4. The incident laser light is assumed to be comprised of two identical plane wave components with wavelength  $\lambda_0 = 1\mu m$  for both  $E_y$  and  $E_z$ , and a homogeneous cell (without nucleus) is placed in the simulation region. The diameter of the cell is taken to be  $11\mu m$

and the refractive index of the inter-cellular medium and cytoplasm are taken the values from Table 5.1. The length of the simulation region is  $40\lambda_0$  in the light propagating direction and  $80\lambda_0$  in each of the two transverse directions. The simulation results are plotted in Fig. 7.4. Figure 7.4 (a) shows the angular spectra of forward scattered light while Fig. 7.4 (b) gives the backscattering results. In both Fig. 7.4 (a) and (b), the solid line is for  $|E_y|^2$ , the symbol + is for  $|E_z|^2$ , and the dotted line is for the results of the 3D scalar solver using the same simulation conditions. Since equations (7.21—7.22) are symmetrical equations for  $E_y$  and  $E_z$  and the initial conditions for  $E_y$  and  $E_z$  are the same, the simulation results of the scattered intensities for  $E_y$  and  $E_z$  should be identical. In fact, from Fig. 7.4 (a) and (b), one can see that the angular distribution of scattered light for two orthogonal electric field components  $|E_y|^2$  and  $|E_z|^2$  are exactly the same.

Figure 7.5 shows the angular distribution of the scattered intensity by a cell in the backward region. The simulation conditions are the same as described in the previous paragraph. The solid line is the result of 3D-3 component vector solver, the dotted line is the result of 3D-2 component vector solver, the dash-dotted line is the output of 3D scalar solver, and dashed line represents the results of Mie theory. In these simulations, the interface profile described in Fig. 4.10 (a) with 6 points per wavelength in propagation direction is used. For the scattered intensity in the backward scattering direction ( $180^\circ$ ), we find in Fig. 7.5 that the result of 3D-3 components solver is the closest to the Mie theory results, and the result of 3D-2 components solver is the second one. The reason is that the  $\nabla(\nabla \cdot \vec{E})$  term in Eq. (7.6) is fully considered in the 3D-3 component solver, partially considered in the 3D-2 components solver, and neglected in the 3D scalar solver. The  $\nabla(\nabla \cdot \vec{E})$  term accounts for the effect of the cell wall, since it is only at this interface when the  $\nabla(\nabla \cdot \vec{E})$  term is non-zero.

Concerning the degree of polarization, the simulation results from our 3D–3 components solver agrees with those from our 3D–2 components solver. Initially, the direction of polarization points  $45^\circ$  against the  $Y$  axis in the  $Y - Z$  plane ( $\vec{E}^0 = \vec{E}_y^0 + \vec{E}_z^0$ ) and the degree of the linear polarization is equal to 1 since the two orthogonal components are initially identical. After scattering, we have  $|E_y|^2 = |E_z|^2$  for forward and backward scattering (see Fig. 7.4). Therefore, for the scattered light, the direction of polarization is  $45^\circ$  against  $Y$  axis in  $Y - Z$  plane and the degree of polarization is also equal to 1.

## 7.6 Conclusion

In order to explore the effects of the polarization of light, a vector equation for 2 transverse field components is derived from Maxwell's equations. An algorithm to solve this coupled equation is presented and a 3D–2 component vector solver (code) is implemented and tested. The simulation results of the 3D–2 component vector solver also shows that if the incident light is 100% polarized parallel to a scattering plane ( $\phi = 45^\circ$ ) then the scattered light is also 100% polarized parallel to that scattering plane, which is in agreement with Mie theory. There is a discrepancy between  $i_{\parallel}$  and  $i_{\perp}$  when the scattering angle is equal to or larger than  $30^\circ$ . Both  $i_{\parallel}$  and  $i_{\perp}$  are in good agreement with the Mie theory results in range of scattering angle up to  $30^\circ$ .

Furthermore, a 3 electric field component wave equation is also derived from Maxwell's equations. An algorithm to solve this coupled vector wave equation is developed and a 3D–3 components solver is implemented. Regarding the observed polarization effects, our 3D–3 component solver gives similar results to our 3D–2 components solver. Comparing to 3D scalar solver and 3D–2 component vector solver results, the simulation results of 3D–3 component vector solver shows an improvement in the backward scattering results.

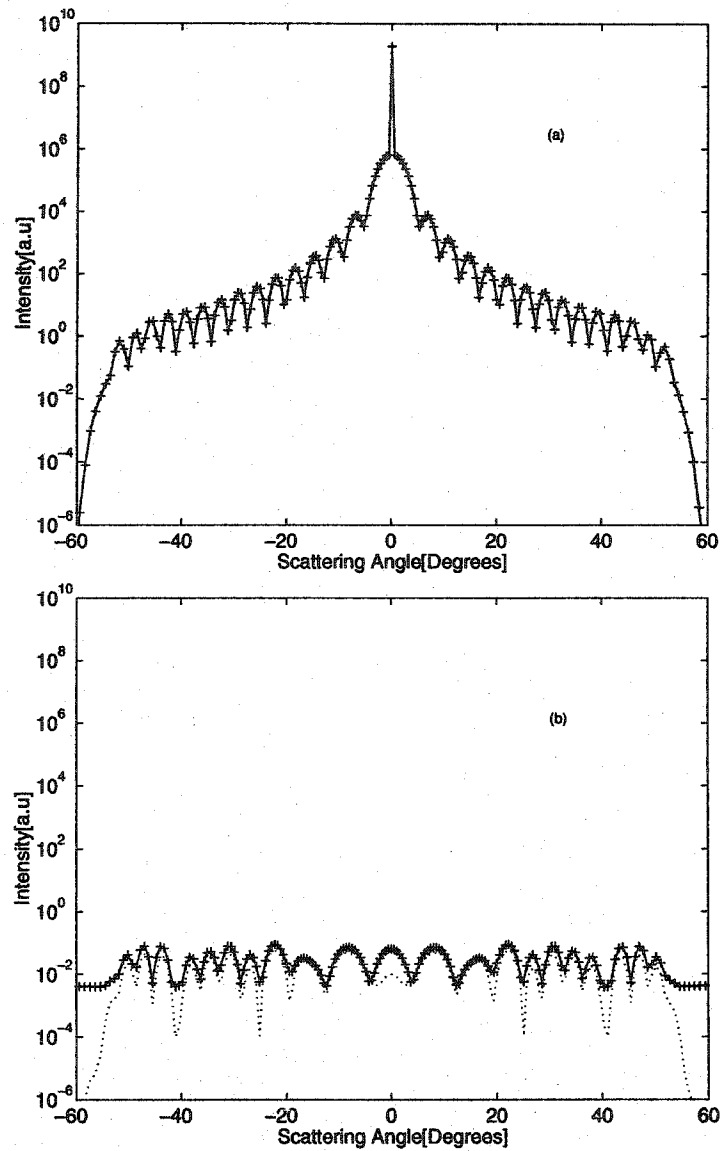


Figure 7.4: The angular spectra of forward and backward scattered light for the  $E_y$  and  $E_z$  components of the electric field as predicted by our three component vector wave equation solver. Figure (a) is for the forward scattered component and (b) is the backward scattered component off a three dimensional single cell with diameter  $D_0 = 11\mu m$ . The solid line is for  $|E_y|^2$ , the symbol + is for  $|E_z|^2$ , and the dotted line represents results obtained with the 3D scalar solver for the same simulation conditions.

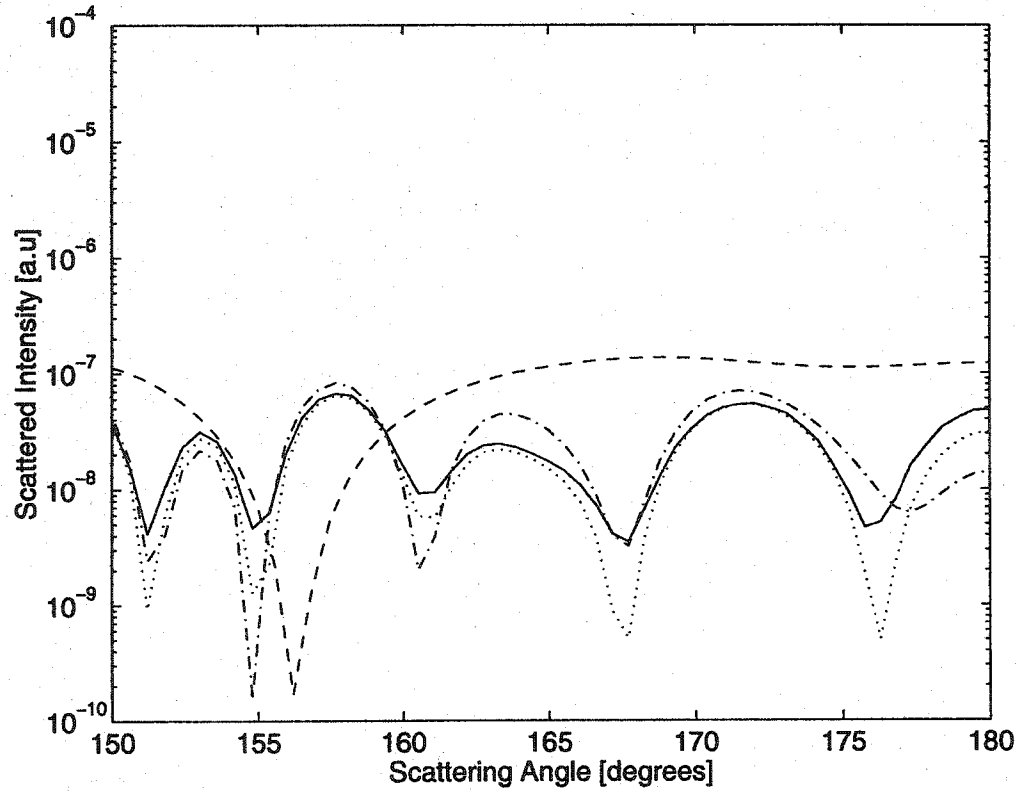


Figure 7.5: The backward scattered intensity by a cell with diameter  $D_0 = 11\mu m$  as simulated by our 3D-3 component vector solver (solid line), 3D-2 component vector solver (dotted line), and 3D scalar solver (dash-dotted line). The dashed line is the result of Mie theory.



## Bibliography

- [1] C. Canuto, M. Y. Hussaini, A. Quarteroni, T. A. Zang, *Spectral Methods in Fluid Dynamics* (Springer-Verlag, Berlin Heidelberg 1988).
- [2] J. M. Sanz-Serna and J. G. Verwer, *IMA Journal of Numerical Analysis* (1986) **6**, 25-42.
- [3] J. M. Sanz-Serna and V. S. Manoranjan, *J. Comp. Phys.* **52**, 273-289.

## Chapter 8

# Experimental Considerations

### 8.1 Introduction

All our efforts towards developing a numerical model of laser-tissue interactions as described in previous chapters are motivated by cytometry applications, particularly micro-cytometry. Micro-cytometry is simply conventional flow cytometry carried out in an apparatus based on a microchip. Recently, Schrum et al. [1] demonstrated a microchip-based cytometer with which they sorted latex beads, correlating the scattered peak intensity with the bead size. They used two different sizes of particles: fluorescent smaller particles with a diameter of  $0.972\mu m$  and non-fluorescent large particles with a diameter of  $1.94\mu m$ . It was found that peak intensity, which corresponds to the total scattered intensity by a particle, was 0.235 times smaller for the  $0.972\mu m$  fluorescent particles as than for the  $1.94\mu m$  non-fluorescent particles [1]. A U.S. company called Micronics has developed a microcytometer in which biological cells from a sample, such as blood, pass in single file through a micro-channel upon which a laser beam is focused. Light scatter measurements are taken at multiple angles over two ranges: forward angle scattering (from 0 to 3 degrees) and small angle scattering

(from 3 to 11 degrees). These multi-parameter scatter measurements provide information about the size and the internal cellular structure for the various type of cells. A study of this device's ability to separate several types of white blood cells has been presented in Ref. [2]. This would be very useful in blood counting and differentiation.

A research project called "Analysis of Cells with Scattered Laser Light" is now being carried out by a collaboration including members from both the Electrical & Computing Engineering and Physics departments at the University of Alberta. This project is realized through marrying existing cutting edge microchip development with a detailed numerical model of scattered light. The objective of this project is the development of an inexpensive instrument using microfluidic technology. Our research approach is to integrate cell sorting and the measurement of the scattered light by a cell with microchips developed at the University of Alberta and Micralyne, a local company.

Figure 8.1 shows a top view of a microchip which consists of micromachined channels. Cell sorting procedures are performed on the microchip where an individual cell moves through microchannels. By applying an electric field, a charged cell will move in a medium toward the cathode or anode, depending on the sign of the applied electric field.

Figure 8.2 shows a schematic of the experimental set-up. When a selected cell passes in front of a laser beam, the incident light is scattered in the forward direction and captured by a very sensitive CCD camera. The experimental program is currently in an early stage. A latex bead with refractive index of 1.35 is used instead of a real cell. The refractive index of the surrounding medium in the microchannels is 1.30. A HeNe laser with wavelength of  $0.6328\mu\text{m}$  is used in our experiment. As described in Fig. 8.2, we also need a very sensitive CCD camera; however, what criteria should we use in selecting a suitable CCD camera?

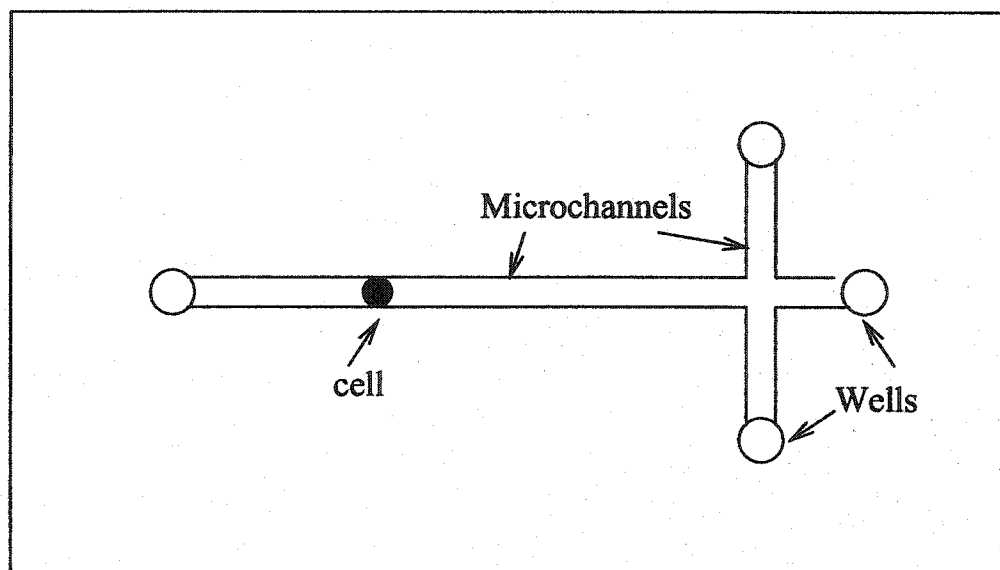


Figure 8.1: Microchip for manipulation of cells

In previous chapters, our results for the scattered intensity were presented in arbitrary units. In order to determine the requisite CCD camera sensitivity, we derive the normalization constant for both Gaussian beam and plane wave incident light sources, allowing us to present the scattered light intensity in an appropriate absolute unit, i.e. *photons/(s.sr)*.

## 8.2 A Gaussian Beam Incident Light Source

An actual incident laser beam can be well described by a Gaussian beam whose profile is given by Eq. (3.23). In this section, we will start from Eq. (3.23) to derive the normalization constant.

The optical energy density  $|E(x, y, z)|^2$  is a function of the radial and axial variables  $\rho = \sqrt{y^2 + z^2}$  and  $x$  [3], i.e.,

$$|E(x, y, z)|^2 = |E_0|^2 \left[ \frac{\sigma}{W(x)} \right]^2 \exp\left[ -\frac{\rho^2}{W^2(x)} \right], \quad (8.1)$$

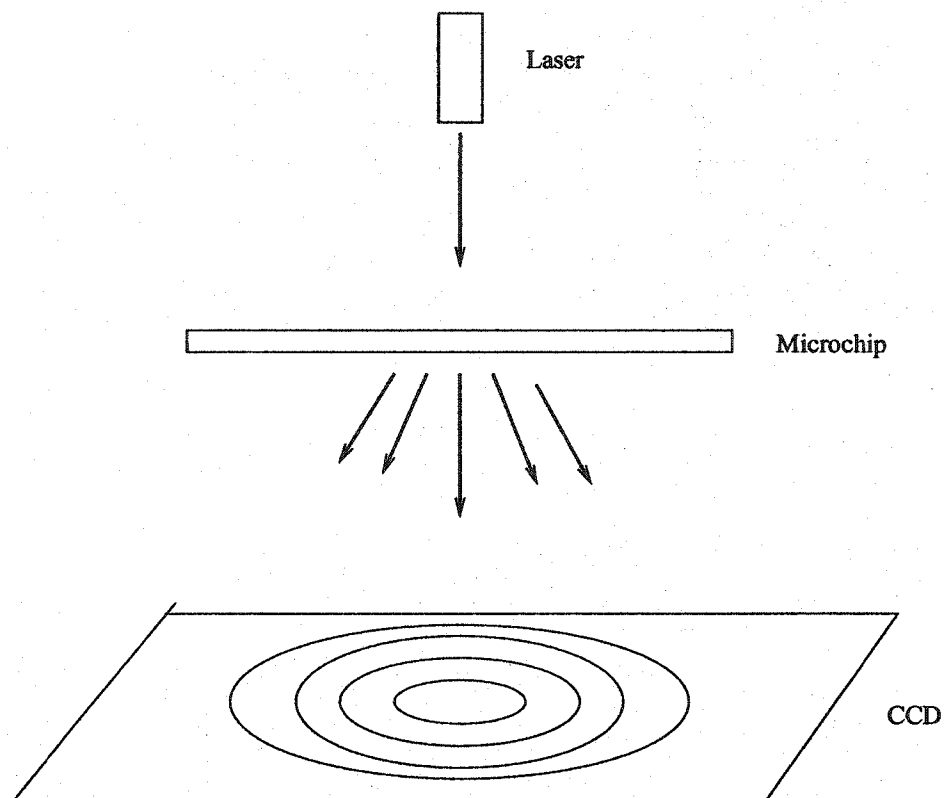


Figure 8.2: Schematic of the experimental setup for measuring forward scattered light by cells

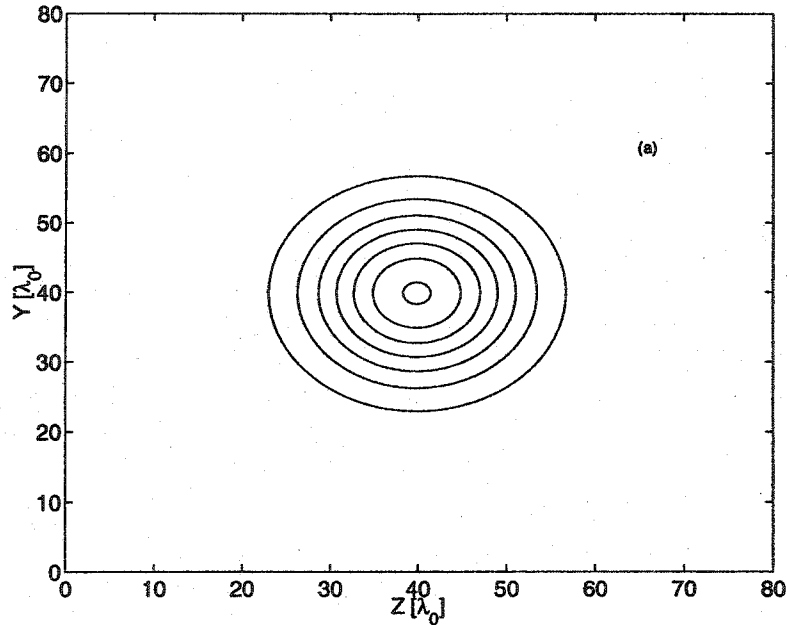


Figure 8.3: A Gaussian Beam with  $f/12$  at best focus, represented as a contour plot.

and the optical flux (intensity) is given by

$$I = \frac{c |E(x, y, z)|^2}{8\pi} = I_0 \left[ \frac{\sigma}{W(x)} \right]^2 \exp\left[-\frac{\rho^2}{W^2(x)}\right], \quad (8.2)$$

where  $I_0 = c |E_0(x, y, z)|^2 / 8\pi$ ;  $W(x)$  is the beam radius defined by Eq. (2.34) and  $\sigma$  is the minimum radius of the beam at the best focus position. Figure 8.3 illustrates the Gaussian function at the best focus position ( $x = 0$ ) with number  $f/12$  where the number  $f$  is defined to characterize the minimum radius  $\sigma$  of the beam at the best focus position by

$$\sigma = f\lambda. \quad (8.3)$$

The total optical power of the beam is the integral of the optical flux over its transverse plane ( $y$ - $z$  plane) at any point on the  $x$ -axis.

$$P = \int_0^{2\pi} d\phi \int_0^\infty I \rho d\rho, \quad (8.4)$$

which leads to

$$P = I_0 \times \pi \sigma^2. \quad (8.5)$$

As expected, the total power is independent of  $x$ . Since Gaussian beams are very often described in terms of their total power  $P$ , it is useful to express  $I_0$  in terms of  $P$  by using Eq. (8.5). Therefore, Eq. (8.2) is rewritten in the form

$$I = \frac{P}{\pi W^2(x)} \exp\left[-\frac{\rho^2}{W^2(x)}\right]. \quad (8.6)$$

Hence, at the best focus position ( $x = 0$ ), we have

$$I = \frac{P}{\pi \sigma^2} \exp\left[-\frac{\rho^2}{\sigma^2}\right]. \quad (8.7)$$

Another parameter which is used to describe Gaussian beams is the full width at half maximum (FWHM). From Eq. (8.2), we have

$$\exp\left(-\frac{\rho_{1/2}^2}{\sigma^2}\right) = \frac{1}{2}, \quad (8.8)$$

where  $\rho_{1/2}$  is the beam radius at which the beam power is one-half of its peak power. Therefore, using Eq. (8.8), the FWHM takes the following form

$$\text{FWHM} = 2\rho_{1/2} = 2\sqrt{\ln 2} \times \sigma. \quad (8.9)$$

In the far-field, we have  $x \gg L_R$ , where  $L_R$  is the Rayleigh Range defined by

$$L_R = 2\pi f^2 \lambda. \quad (8.10)$$

In this limit we may rewrite Eq. (8.1) as

$$|E(x, y, z)|^2 = |E_0|^2 \frac{L_R^2}{x^2} \exp\left[-\frac{L_R^2 \rho^2}{\sigma^2 x^2}\right], \quad (8.11)$$

where we have used the relation  $W(x) = \sigma \sqrt{1 + (x/L_R)^2}$ . The flux  $I$  in the far-field then takes the form

$$I = \frac{c |E(x, y, z)|^2}{8\pi} = \frac{c |E_0|^2 L_R^2}{8\pi x^2} \exp\left[-\frac{L_R^2 \rho^2}{\sigma^2 x^2}\right]. \quad (8.12)$$

The total power in the far-field (for arbitrary fixed  $x$ ) is given by integral of Eq. (8.12)

$$\begin{aligned} P &= 2\pi I_0 \frac{L_R^2}{x^2} \int_0^\infty \exp\left(-\frac{L_R^2}{x^2 \sigma^2} \rho^2\right) \rho d\rho \\ &= I_0 \times \pi \sigma^2, \end{aligned} \quad (8.13)$$

which is the same as Eq. (8.5). Therefore, it can be seen that our analytical expression (8.12) of a Gaussian beam in the far-field conserves energy.

The power per solid angle in the far-field  $Q$  takes the following expression:

$$Q = \frac{c|E(x, y, z)|^2}{8\pi} r^2 = \frac{c|E_0|^2}{8\pi} \frac{L_R^2}{\cos^2 \theta} \exp\left[-\frac{L_R^2}{\sigma^2} \tan^2 \theta\right], \quad (8.14)$$

where we used the following relations:

$$x = r \cos \theta \quad (8.15)$$

$$y = r \sin \theta \sin \phi$$

$$z = r \sin \theta \cos \phi.$$

When the incident laser light is a Gaussian beam and propagates in free space (without scattering), Eq. (8.14) is the distribution function in the far-field. The normalization factor can be obtained from Eq. (8.14) when  $\theta = 0$ . In this case, the normalization constant  $Q_0$  for a Gaussian beam can be expressed as the following

$$Q_0 = \frac{c|E_0|^2}{8\pi} L_R^2 = \frac{P}{\pi \sigma^2} L_R^2, \quad (8.16)$$

where  $L_R = 2\pi f^2 \lambda$ ,  $\sigma = f \lambda$  and  $Q_0$  has unit of  $J/(s \cdot sr)$  when  $P$  has unit of  $J/s$ . The angle dependent term  $\Phi(\theta)$  takes the form

$$\Phi(\theta) = \frac{1}{\cos^2 \theta} \exp\left(-\frac{L_R^2}{\sigma^2} \tan^2 \theta\right). \quad (8.17)$$

Figure 8.4 shows the comparison of analytical results and non-scattering simulation results. For a fixed length of the simulation box in transverse directions,



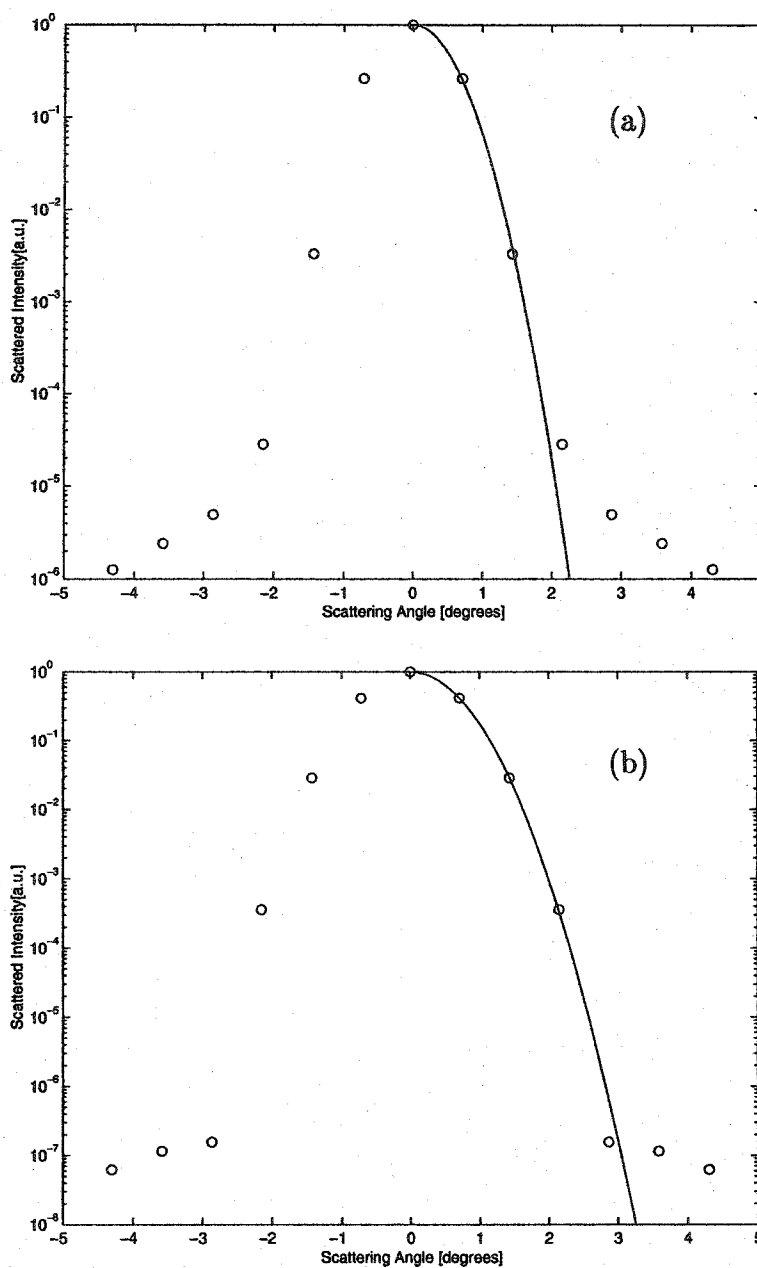


Figure 8.4: The far-field distributions of a Gaussian beam with (a)  $f/15$  and (b)  $f/12$ . The solid lines represent the analytical results (8.17) and circles are our non-scattering simulation results with  $L_y = L_z = 80\lambda$  and  $\lambda = 0.6328\mu m$ .

i.e.  $L_y = L_z = 80\lambda$ , deviations of analytical and simulation results decrease with the  $f$  number of Gaussian beam. The wider beam, the greater the proportion of the beam profile which extends beyond the transverse boundary. As described in Chapter 3, we only collect signals on the plane of  $x = X_l$  for forward far-field calculation. Given  $L_y = L_z = 80\lambda$  and  $f = 12$ , the analytical result (8.17) and the simulation result fully agree with each other over 6 orders of magnitude (refer to Fig. 8.4 (b)). Therefore, one can conclude that with  $L_y = L_z = 80\lambda$ , the widest Gaussian beam which can be accurately modelled with our simulation code (3D scalar solver) is a beam with  $f/12$  optics.

If an incident Gaussian beam is focused on a cell of radius  $R$ , the average incident flux on the cell takes the following form

$$\begin{aligned} I_{av} &= \frac{I_0}{\pi R^2} \int_0^{2\pi} d\phi \int_0^R \exp\left(-\frac{r^2}{\sigma^2}\right) r dr \\ &= I_0 \left(\frac{\sigma}{R}\right)^2 \left[1 - \exp\left(-\frac{R^2}{\sigma^2}\right)\right], \end{aligned} \quad (8.18)$$

where  $I_0$  is the maximum flux of a Gaussian beam (8.5).

A plane wave can be used to model a wider beam than  $f/12$  if necessary. The derivation of the normalization constant for a plane wave will be given in next section.

### 8.3 Plane Wave

An ideal plane wave extends out to  $\pm\infty$  in the two transverse directions (assumed to be  $y$  and  $z$ ). Without scattering, the Fourier Transform of the distribution in the far-field should be a  $\delta$ -function in both the  $k_y$  and  $k_z$  components. However, in our simulations, we are only able to include a finite range of the two transverse dimensions  $L_y$  and  $L_z$ . As a result, in the absence of scattering, the far-field distribution exhibits a finite  $\delta$ -function-like spike at a scattering angle of

zero degrees. Figure 8.5 illustrates a such distribution. Assuming that the normalization is  $Q_0$  with unit of  $J/(s.sr)$  and the normalized distribution is  $\Phi(\theta)$ , the total power in the field takes the form

$$P = Q_0 \int_0^{2\pi} d\phi \int_0^{\pi/2} \Phi(\theta) \sin \theta d\theta. \quad (8.19)$$

Based on the distribution function shown in Fig. 8.5, integral (8.19) becomes

$$P = \frac{1}{2} Q_0 2\pi \int_0^{\delta\theta} \sin \theta d\theta, \quad (8.20)$$

which can be evaluated to give

$$P = 2\pi Q_0 \sin^2\left(\frac{1}{2}\delta\theta\right), \quad (8.21)$$

where  $\delta\theta$  is the resolution determined by the length of our simulation box in the transverse directions ( $L_y = L_z = L = 80\lambda$ ). In particular,

$$\delta\theta = \frac{\delta k}{k} = \frac{2\pi}{L} \frac{1}{k} = \frac{\lambda}{nL} \leq \frac{1}{80}, \quad (8.22)$$

where  $n$  is the refractive index of surrounding medium. Therefore, we use the small angle approximation to express  $\sin^2(\frac{1}{2}\delta\theta) = (\frac{\delta\theta}{2})^2$  and Eq. (8.21) then becomes

$$P = \frac{\pi}{2} Q_0 \left(\frac{\lambda}{nL}\right)^2. \quad (8.23)$$

The incident optical power takes the form

$$P_{in} = \frac{c|E|^2}{8\pi} L^2. \quad (8.24)$$

By energy conservation, we have  $P_{in} = P$ . Therefore, the normalization constant for a plane wave takes the form

$$Q_0 = \frac{2P_{in}}{\pi} \left(\frac{nL}{\lambda}\right)^2 \quad (J/s.sr), \quad (8.25)$$

where we have used the fact that the incident flux is given by  $I = \frac{c|E|^2}{8\pi} = \frac{P_{in}}{L^2}$  and that  $P_{in}$  is expressed in units of  $J/s$ .

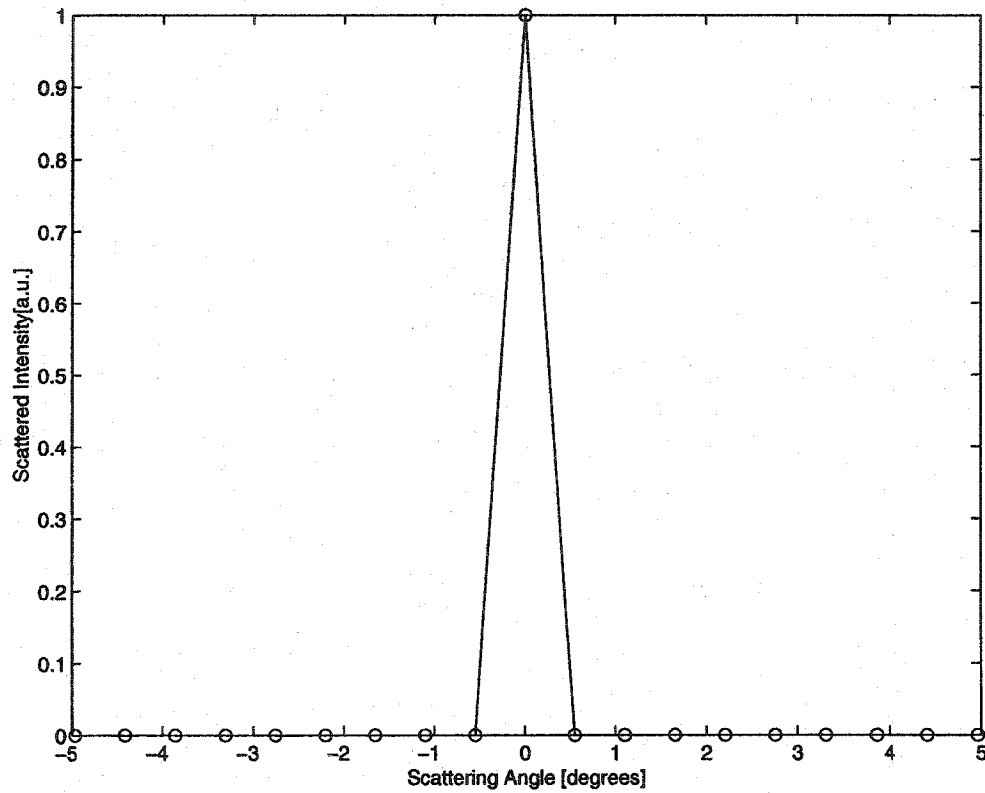


Figure 8.5: The far-field distribution for an incident plane wave in the absence of scattering. The resolution is determined by the length of the transverse directions in our simulation box.

So far, we have derived the normalization constant  $Q_0$  for both Gaussian beam and plane wave incident light sources. In the next section, we present our simulation results for the scattered intensity—in absolute units of *photons/(s.sr)*—as obtained from our 3D scalar solver code.

## 8.4 Simulation Results

We shall start by comparing the results of our simulation with analytical Mie theory calculation results published in Ref. [4]. In this study, Kashima et.al. computed the scattering cross-section for beads of various radii. Their calculations used refractive indices of 1.40 and 1.349 for the beads and the surrounding media, respectively, and used a laser wavelength of  $0.805\mu m$ .

For our simulation, we will assume that the total power is  $1mW$ . We begin by computing the appropriate normalization constants for both the Gaussian beam and the plane wave cases. Through the use of Eq. (8.16), we determine  $Q_0 = 0.734 \times 10^{18} \text{photons}/(s.sr)$  for a Gaussian beam with  $f/12$  optics. Similarly by using Eq. (8.25), we find  $Q_0 = 3.01 \times 10^{19} \text{photons}/(s.sr)$  for a plane wave.

Figure 8.6 shows our 3D scalar simulation results for the case when the radius of cell is  $2.78\mu m$ . Fig. 8.6 (a) gives the scattered intensity distribution for a  $f/12$  Gaussian beam. The total scattered power is given by

$$P_{ts} = 2\pi \int_{0^\circ}^{180^\circ} I(\theta) \sin \theta d\theta = 4.96 \times 10^{14} (\text{photons}/s). \quad (8.26)$$

By using Eq. (8.18), the average incident intensity  $I_{av}$  on a cell can be shown to be  $1.32 \times 10^{13} (\text{photons}/(s.\mu m^2))$ . The scattering cross section is therefore given by

$$\sigma_{sca} [\mu m^2] = \frac{P_{ts} [\text{photons}/s]}{I_{av} [\text{photons}/s/\mu m^2]}. \quad (8.27)$$

Conversely, when the incident laser light is a plane wave, we obtain the scattered intensity distribution function  $I(\theta)$  as shown in Fig. 8.6 (b). The total scattered

power is  $4.80 \times 10^{13}(\text{photons}/s)$ . In this case, the average incident intensity  $I_{av}$  is given by

$$I_{av} = P/L^2, \quad (8.28)$$

where  $L$  is the length of two transverse directions, taking  $L_y = L_z = L = 80\lambda$ .

The scattering cross sections obtained from our simulations were compared with published results in Ref. [4], and these are tabulated in Table 8.1. It is readily seen that our simulation results for the Gaussian beam and the plane wave bracket the published results. In particular, there is reasonably good agreement between the published results and our simulation results for the plane wave.

Published Result		Gaussian Beam			Plane Wave	
$R(\mu m)$	$\sigma_{sca}(\mu m^2)$	$I_{av}(\frac{\text{photons}}{s \cdot \mu m^2})$	$P_{ts}(\frac{\text{photons}}{s})$	$\sigma_{sca}(\mu m^2)$	$P_{ts}(\frac{\text{photons}}{s})$	$\sigma_{sca}(\mu m^2)$
5.5	N/A	$1.18 \times 10^{13}$	$8.09 \times 10^{14}$	68.6	$1.067 \times 10^{14}$	109.2
2.78	46.7	$1.32 \times 10^{13}$	$4.96 \times 10^{14}$	37.6	$4.80 \times 10^{13}$	49.1
2.56	35.0	$1.33 \times 10^{13}$	$4.12 \times 10^{14}$	31.0	$3.85 \times 10^{13}$	39.4
2.29	23.3	$1.33 \times 10^{13}$	$2.95 \times 10^{14}$	22.2	$2.77 \times 10^{13}$	28.3

Table 8.1: Our calculation results of scattering cross section against the published results in Ref. [4]. In the plane wave case, the average incident intensity is equal to  $9.77 \times 10^{11}(\text{photons}/s/\mu m^2)$ .

For the case of our proposed experiments, the refractive index of the beads is 1.35 and the refractive index of the surrounding medium is 1.30; the wavelength of the laser light is  $0.6328\mu m$  and total laser power is  $1.0mW$ ; and the incident beam can be described as a Gaussian beam but with large f number. Therefore, we provide our simulation results in two cases: incident light source as a Gaussian beam with  $f/12$  optics and as a plane wave.

Figure 8.7 gives the scattered intensity distribution using the absolute units of  $\text{photons}/(s \cdot sr)$  when the radius of the beads is  $5.5\mu m$ . Fig. 8.7 (a) shows

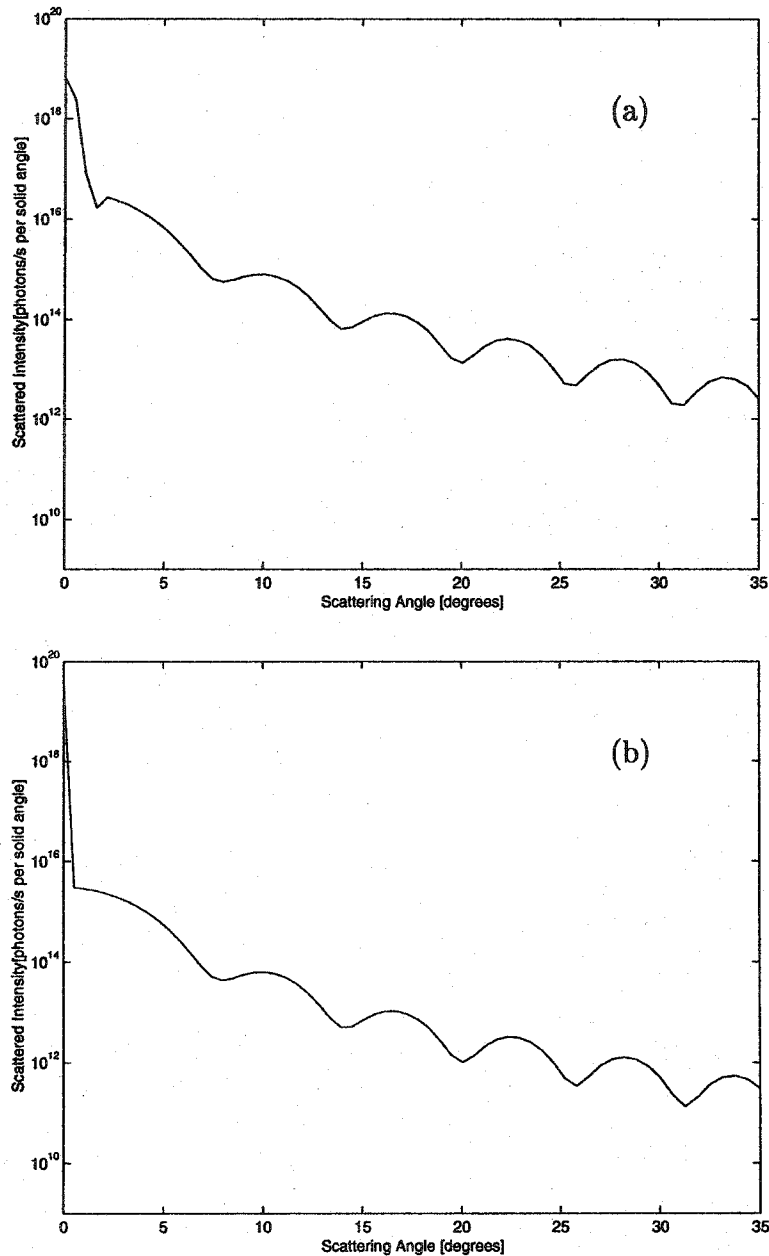


Figure 8.6: The far-field distributions (a) for a Gaussian Beam with  $f/12$  and (b) for a plane wave. The wavelength  $\lambda = 0.805\mu m$ ; the radius of cell is  $2.78\mu m$ ; the incident power  $P = 10^{-3} J/s$ ; and the refractive indices of cell and surrounding media are 1.4 and 1.349, respectively.

the intensity distribution when the incident beam is a Gaussian beam with  $f/12$  optics, while Fig. 8.7 (b) illustrates the corresponding distribution in the plane wave case. Figure 8.8 shows the scattered intensity distribution using absolute units of  $photons/(s.sr)$  when the radius of the beads is  $3.5\mu m$ .

The scattering cross sections of the beads obtained from our calculations for both the Gaussian beam and plane wave cases are given in Table 8.2.

Radius	Gaussian Beam			Plane Wave		
$R(\mu m)$	$I_{av}(\frac{photons}{s.\mu m^2})$	$P_{ts}(\frac{photons}{s})$	$\sigma_{sca}(\mu m^2)$	$I_{av}(\frac{photons}{s.\mu m^2})$	$P_{ts}(\frac{photons}{s})$	$\sigma_{sca}(\mu m^2)$
5.5	$1.36 \times 10^{13}$	$8.30 \times 10^{14}$	61.0	$1.24 \times 10^{12}$	$1.106 \times 10^{14}$	89.2
3.5	$1.58 \times 10^{13}$	$7.31 \times 10^{14}$	46.3	$1.24 \times 10^{12}$	$8.398 \times 10^{13}$	67.7

Table 8.2: The cross section of the beads obtained from our calculation for the proposed experiments: the wavelength  $\lambda = 0.6328\mu m$ ; the refractive indices of the cell and the surrounding medium are 1.35 and 1.30, respectively.

A term of figure merit (FOM) is introduced to express the intensity level of the brightest peak (excepting the one at  $0^\circ$ ) with respect to the weakest peak at  $35^\circ$ . For example, the FOM in Fig. 8.7 (a) is approximately equal to 3 and this will restrict the acquisition of cytometry data to reduced angular ranges. Recording scattering intensities over small angle intervals and combining results will increase the time and cost of medical diagnostics. Therefore, we propose a method of using a angular radial gradient filter to selectively attenuating scattering intensities over a wide angular range.

Ideally, we would like to obtain the same intensity levels for all scattering peaks. However, it is not trivial to develop such a angular radial gradient filter. We have developed a method of obtaining such an equalization although we are in the process of improving performance. At present we can obtain the attenuated scattering intensities shown in Fig. 8.9 with an improved FOM of 1.5 [5]. This



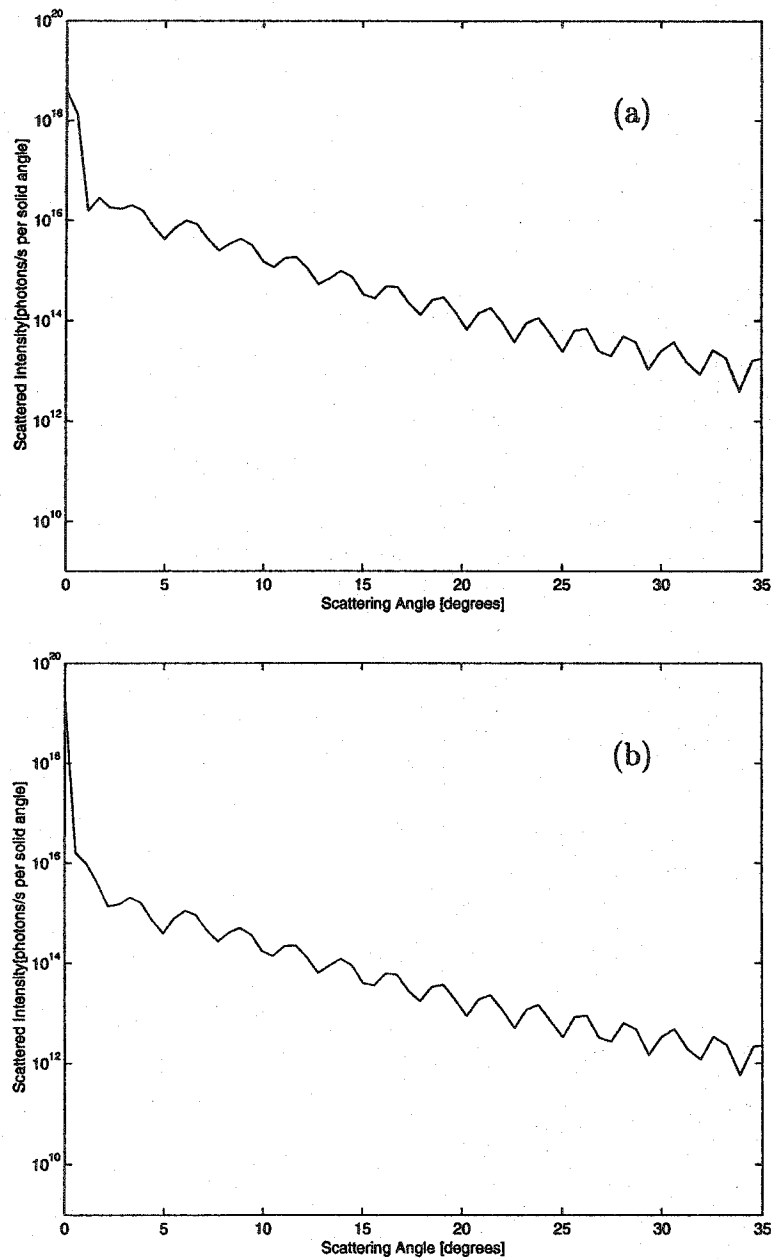


Figure 8.7: The far-field distributions (a) for a Gaussian Beam with  $f/12$  and (b) for a plane wave. The wavelength  $\lambda = 0.6328\mu m$ ; the radius of cell is  $5.5\mu m$ ; the incident power  $P = 10^{-3} J/s$ ; and the refractive indices of the cell and the surrounding medium are 1.35 and 1.30, respectively

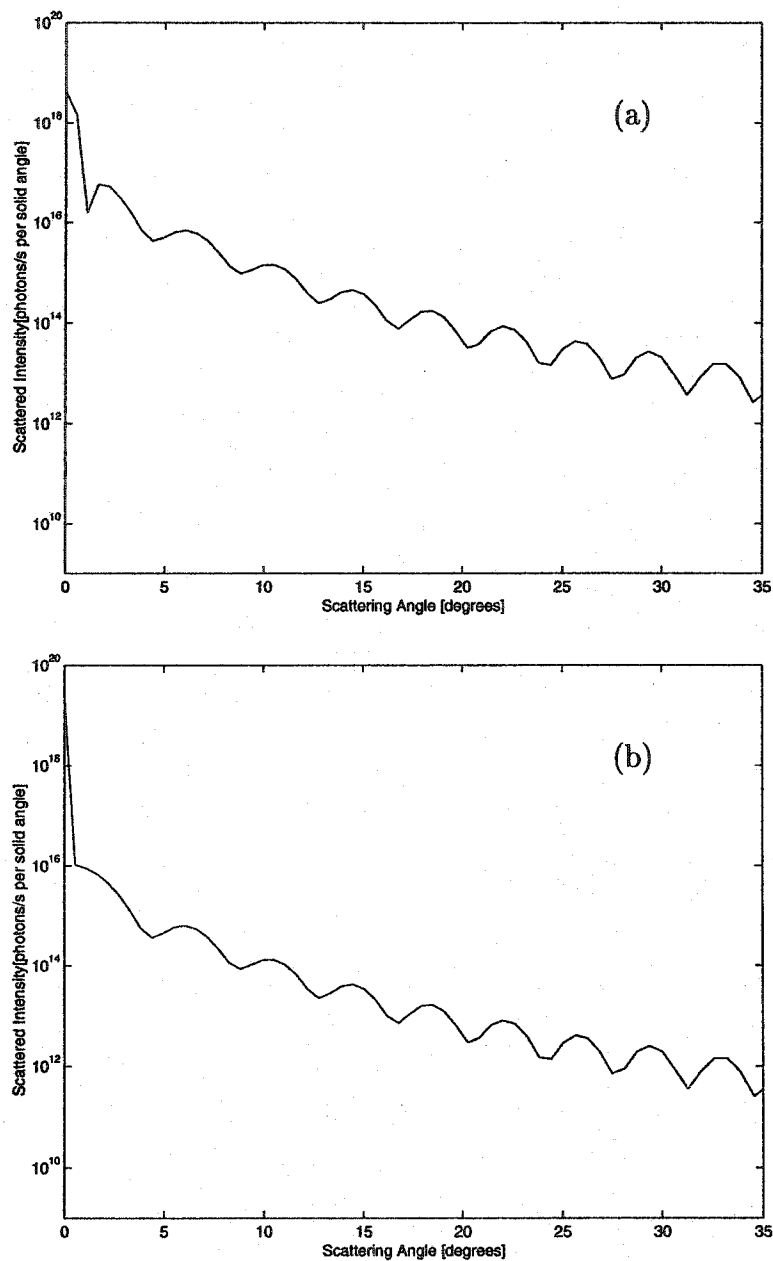


Figure 8.8: The far-field distributions (a) for a Gaussian Beam with  $f/12$  and (b) for a plane wave. The wavelength  $\lambda = 0.6328\mu m$ ; the radius of cell is  $3.5\mu m$ ; the incident power  $P = 10^{-3} J/s$ ; and the refractive indices of the cell and the surrounding medium are 1.35 and 1.30, respectively.

figure displays the number of photons/s incident on  $1\mu m^2$  of a charge-coupled device (CCD) vs scattering angle at  $2.5cm$  distance which is for CCD cameras. This leads us to believe that our method allows scattering data collection in one single test, eliminating the need for preferential sampling at particular angle.

It is also important to choose an adequately sensitive CCD camera capable of dealing with the low illumination levels at larger angles and to have a reliable recording of scattering data. The simulations described above allow us to make prediction photon counts. Based on this information, we estimated a signal-to-noise ratio (SNR) of  $\sim 36$  dB, taking into account the brightest and weakest scattering peaks. The SNR for a CCD camera is calculated as: [6]

$$SNR = \frac{I \cdot QE \cdot t}{\sqrt{I \cdot QE \cdot t + N_d \cdot t + N_r^2}} \quad (8.29)$$

where  $I$  stands for the intensity in the unit of *photons/sperpixel*,  $QE$  is the quantum efficiency,  $t$  stands for the integration time in the unit of seconds,  $N_d$  is the dark current noise in unit of *electrons/pixel/second*, and  $N_r$  is the read noise in the unit of *electronsrms/pixel*. We conclude that a camera designed for astronomical observations, such as Starlight- Xpress HX 516 [7] is an appropriate choice.

## 8.5 Conclusions

In this chapter we presented a detailed derivation of the normalization constant for both Gaussian beam and plane wave incident sources. We observed good agreement between our simulation results and those published in Ref. [4]. We were also able to use our 3D scalar solver simulation results, normalized to appropriate units, to provide an estimate of our proposed experimental measurement of the scattering cross-section and to help to refine our CCD camera criteria. The simulations allow us to make prediction photon counts. Based on this informa-

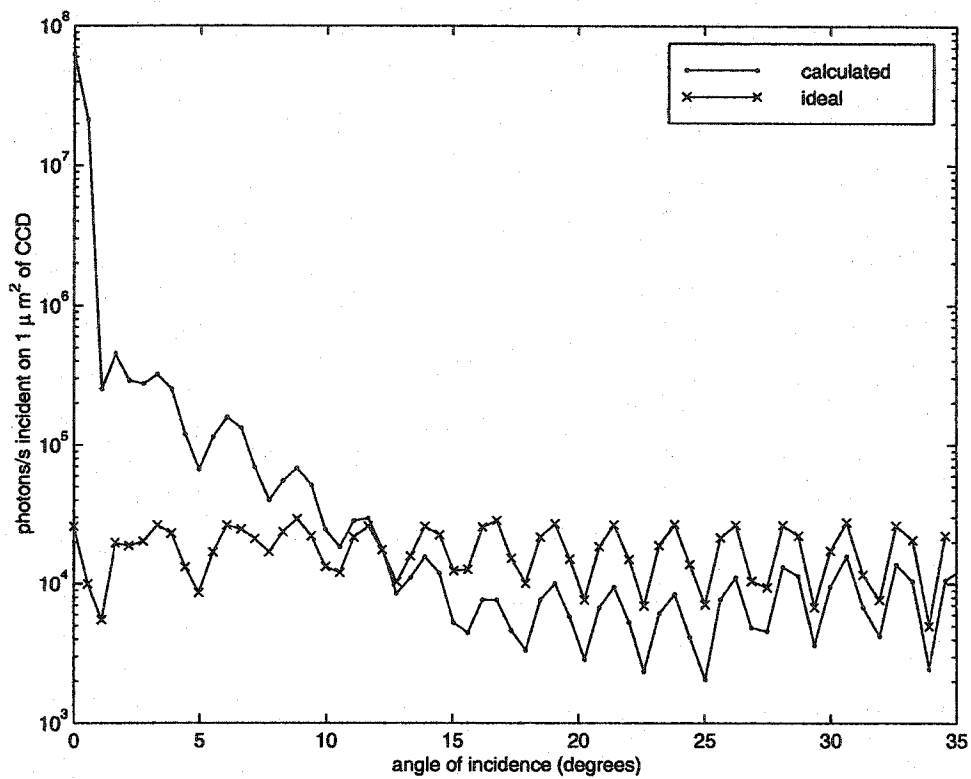


Figure 8.9: Photons/s incident on  $1\mu\text{m}^2$  of CCD vs scattering angle for an ideal equalization of scattering peaks and a calculated scenario using our method. Cell radius  $5.5\mu\text{m}$  and laser wavelength  $0.6328\mu\text{m}$ .

tion, we estimated a signal-to-noise ratio (SNR) of  $\sim 36$  dB, taking into account the brightest and weakest scattering peaks. Then we conclude that a camera designed for astronomical observations, such as Starlight- Xpress HX 516 is an appropriate choice.

## Bibliography

- [1] D. P. Schrum, C. T. Culbertson, S. C. Jacobson, and J. M. Ramsey, *Microchip flow cytometry using electrokinetic focusing*, *Anal. Chem.* **71**, 4173-4177(1999)
- [2] E. Altendorf, D. Zebert, M. Holl, A. Vannelli, C. Wu and T. Schulte, *Results obtained using a prototype microfluidics-based hematology analyzer*, Micro TAS98, Banff, Canada(1998)
- [3] B. E. A. Saleh and M. C. Teich, *Fundamentals of Photonics* (New York: Wiley , 1991).
- [4] S. Kashima, A. Sohda, Y. Yagyu and T. Ohsawa, *Determination of Deformability of erythrocytes by change in scattering cross section*. *Jpn. J. Appl. Phys.* Vol.34 pp.680-682, 1995
- [5] C.-G. Stefanita, Y. Shao, W. Rozmus, C. E. Capjack, and C. J. Backhouse, *Microchip-Based Optical Device for Medical Diagnostics Performed on a Single Cell*, IEEE Proceedings of the 2002 2<sup>nd</sup> Conference on Nanotechnology, Washington, D. C., August 26-28, pp. 133-136.
- [6] *Roper Scientific (2002)*, available online: <http://www.roperscientific.com>
- [7] *Starlight Xpress (2002)*, available online: <http://www.starlight.com>

## Chapter 9

### Summary

This dissertation presents numerical and theoretical studies of the scattering properties of inhomogeneous cells. The spectral method is applied to solve two- and three-dimensional scalar wave equations. Simulation tools which include a 2D scalar solver and a 3D scalar solver have been implemented for modelling the scattering of laser light in biological tissue. These simulation tools are capable of predicting with high resolution the intensity of scattered light from cells with internal structures, and provide numerical support for microcytometry experiments which are being carried out in the ECE Department at the University of Alberta. Furthermore, in order to explore polarization effects in the processes of laser light-tissue scattering, the spectral technique has also been applied to solve the 3-D, 2- electric field component coupled wave equations and the 3-D, 3- electric field component coupled wave equations.

The Mie theory was reviewed in detail in chapter 2. For the case of laser light scattered by a homogeneous sphere, the relationship between Stokes parameters of the incident and scattered waves can be expressed as  $S_s = MS_i$ , where the scattering matrix  $M$  is a  $4 \times 4$  matrix called the Mueller matrix. If the incident light is 100% polarized parallel to an arbitrary scattering plane, the scattered

light is also 100% polarized parallel to the scattering plane. If the incident light is 100% polarized parallel to an arbitrary scattering plane, the scattered light is also 100% polarized parallel to the scattering plane. If the incident light is unpolarized, the scattered light may be polarized perpendicular to or parallel to the scattering plane. However, the degree of polarization of the scattered light is always equal to zero in the forward ( $0^\circ$ ) and backward ( $180^\circ$ ) directions. A Mie theory code has been developed and its computational results are applied as a benchmark for our other more detailed numerical simulations.

A detailed computational model, which allows us to describe the interaction of a laser with biological objects on spatial scales ranging from single cells to larger samples, has been presented in Chapter 3. In this model, a 3D scalar wave equation has been derived from Maxwell's equations and the nonparaxial spectral method is employed to solve the equation. The issue of far-field calculations has also been addressed.

In Chapter 4, based on the computational model, a 2D scalar solver and a 3D scalar solver were developed and implemented as optimized and parallelized simulation tools. The accuracy of the 2D scalar solver has been verified by comparison with linear perturbation theory. Comparison with Mie theory also indicated that the 3D scalar wave equation is a good approximation to the full set of Maxwell equations for light scattering at moderate angles.

The simulation results of our 2D scalar solver were presented in Chapter 5. It was demonstrated that the spectral method can be efficiently used in modelling laser light scattering for samples ranging in size from a single cell to large biological samples. In the case of laser light scattering from single cells, the most significant features of the angular distribution of the scattered light from various cells occurs at small angles. Cells containing large nuclei have more scattering at small angles compared to cells containing normal-sized nuclei. The



amplitude of scattered light decreases even further for cells without a nuclei. In the case of scattering from multiple cells, the simulation results show that the fraction of the scattered power depends on the number of scatterers and not on the size of simulation region. In fact, the fraction of the scattered power is almost linearly proportional to the number of scatterers. Finally, the scattering pattern from many cells still retains the angular distribution characteristic of single cell forward scattering.

In Chapter 6, an optimized and parallelized 3D scalar solver has been used to efficiently model laser light scattering from both single cells and larger biological samples. In the case of laser light scattered by single cells, the cases of a plane wave and a Gaussian beam are used as the incident laser light source. The simulation results demonstrate that this 3D scalar solver is a valuable simulation tool in cell cytometry, for example, in the detection of rare event cells and cancerous cells. The healthy cell usually has a nucleus with diameter of  $3\mu m$  and the cancerous cell has a nucleus with diameter of  $6\mu m$ . The scattered spectra from a cell with a  $3\mu m$  diameter nucleus and with a  $6\mu m$  nucleus are different. This is the first reported implementation of the spectral technique for modeling the scattering of laser light in biological tissue. The accuracy of the spectral numerical method has been verified by comparison with linear perturbation theory and Mie theory.

The polarization information in the processes of light scattering with cells has been addressed in Chapter 7. In order to explore the effects of the polarization of light, a vector equation for 2 transverse field components is derived from Maxwell's equations. An algorithm to solve this coupled equation is presented and a 3D-2 components vector solver (code) is implemented and tested. Comparing to 3D scalar solver' results, the simulation results from the 3D-2 components vector solver improve the backward scattering distribution which is

closer the Mie theory result. The simulation results of 3D-2 component vector solver also shows that if the incident light is 100% polarized parallel to a scattering plane ( $\phi = 45^\circ$ ), then the scattered light is also 100% polarized parallel to that scattering plane, which, again, is in agreement with Mie theory. Furthermore, a 3 electric field component wave equation is also derived from Maxwell's equations. An algorithm to solve this coupled vector wave equation is developed and a 3D-3 component solver is implemented. The simulation results of 3D-3 components give our best agreement with Mie theory in the backward scattering region. Both our 3D-2 and 3D-3 component solvers agree with each other regarding the polarization of the scattered light.

In Chapter 8, we give an outline of our proposal to consider the scattering of laser light from latex beads. The issue of appropriate normalization of our simulation results in both plane wave and Gaussian beam cases is addressed. We are therefore able to present the angular spectra of the scattered light intensity in units of *photons/(s.sr)*. Moreover, we may use our results for the angular spectra to calculate the scattering cross section. The simulations allow us to make prediction photon counts. Based on this information, we estimated a signal-to-noise-ratio (SNR)  $\sim 36$  dB, taking into account the brightest and weakest scattering peaks. Then we conclude that a camera designed for astronomical observations, such as Starlight-Xpress HX 516 is an appropriate choice.

The computational requirements for the spectral method in modeling laser interaction with biological samples are much lower than the requirements for other established numerical methods: FDTD and MC. For example, three-dimensional simulations of a sample with each spatial dimension approximately equal to  $100\mu m$ , only require about 1 Gb of operational memory and 3 hours of computational time on a 16 processors SGI Origin 2400 computer. The spectral method can be successfully applied to address scattering from individual cells

and from biological samples containing many cells.

Our spectral technique has a very high spatial resolution which is limited by the dimension of transverse directions; for example, if the laser wavelength  $\lambda$  is equal to  $1.0\mu m$  and the  $L_y = L_z = 80\lambda$ , then the resolution is 0.53 degrees, which is comparable to the resolution obtained in experiments. It accurately models inhomogeneities on spatial scales larger than the laser wavelength, and treats inhomogeneities with a spatial scale much smaller than the laser wavelength as sharp boundaries.

Our simulation codes have been successfully used in prediction of our proposed experimental measurement of scattered laser light from latex beads. In the future, our simulation codes will be extensively used in micro-cytometry experiments. By comparison of our simulation results with experimental measurements, we can determine cell parameters, such as size, refractive index, and composition.